K E D R

Status Report

May 1990

KEDR COLLABORATION

V. V. Anashin, E .V. Anashkin, V. M. Aulchenko, B. O. Baibusinov,
L. M. Barkov, S. E. Baru, V. G. Biryukov, A. E. Blinov, V. E. Blinov,
A. E. Bondar, A. D. Bukin, A. G. Chilingarov, Yu. I. Eidelman,
S. I. Eidelman, F. E. Falkenstern, P. B. Gaidarev, V. R. Groshev,
G. Ya. Kezerashvili, S. G. Klimenko, G. M. Kolachev, V. N. Kozlov,
A. S. Kuzmin, O. B. Lazarenko, P. K. Lebedev, M. Yu. Lelchuk,
L. A. Leontiev, G. D. Minakov, M. D. Minakov, S. I. Mishnev,
V. P. Nagaslaev, A. B. Nomerotsky, A. P. Onuchin, V. S. Panin,
V. V. Petrov, G. S. Philimonov, S. G. Pivovarov, Yu. V. Pril,
I. Yu. Protopopov, T. A. Purlatz, N. I. Root, V. A. Rodjakin,
A. I. Romanchuk, L. V. Romanov, A. V. Rylin, G.A.Savinov,
V. P. Savinov, V. V. Serbo, A. G. Shamov, M. A. Shubin,
A. I. Shusharo, B. N. Shuvalov, B. A. Shwartz, V. A. Sidorov,
Yu. I. Skovpen, A. N. Skrinsky, V. P. Smakhtin, S. D. Soroka,
V. A. Tayursky, V. I. Telnov, A. B. Temnykh, Yu. A. Tikhonov,
V. M. Titov, G. M. Tumaikin, A. E. Undrus, A. E. Volkov,
A. I. Vorobiov, V. I. Yurchenko, V. N. Zhilich and A.A.Zholentz
Institute of Nuclear Physics, Novosibirsk,USSR

P. Cantoni , P. L. Frabetti , L. Stagni
Dipartimento di Fisica Università di Bologna and INFN-Bologna, Italy

M. Bazzotti, F. Lanni, P. Kulinich*, G. Lo Bianco , B. Maggi,
F. Palombo , A. Sala
Dipartimento di fisica Università di Milano and INFN-Milano, Italy

F. Nava , R. Tonini
Dipartimento di Fisica Università di Modena and INFN-Bologna, Italy

G. Cesura, M Citterio, D. Marioli, P. F. Manfredi, V. Re, L. Rovati, V. Speziali
Dipartimento di Electronica Università di Pavia and INFN-Milano, Italy

H. Calen, S. Kullander
Unit of High Energy Physics of the Uppsala University, Sweden

* On leave of absence from the JINR (Dubna - USSR)

TABLE OF CONTENTS

1.Introduction

The KEDR detector will be used in experiments at the electron- -positron collider VEPP-4M in the energy region of Υ-mesons. The first workshop of the KEDR detector was organized in December 1986.

In 1987 Italian physicists from INFN (Universities of Bologna, Milan and Pavia) joined the Novosibirsk groups of the Institute of Nuclear Physics (INP) in the KEDR project and the Collaboration presented the proposal for the experiment (V. V. Anashin et al., KEDR detector for VEPP-4M. June 1987).

At the time parallel variants Bof some parts of the detector (the electromagnetic calorimeter, the hadron identification system and the magneic coil) were developed.

As a result of the success of the tests with prototypes of an e.m. calorimeter based on liquid krypton (LKr) and of the experience obtained in the work with cesium iodide, it was decided to realize a conbined calorimeter with the barrel part based on LKr (35 t) and the endcapsbased on CsI crystals (3.5 t).

For hadron identification the most impressive result was the development of the aerogel Cherenkov counters and by the beginning of 1990 the prototype was successfully tested.

As far as warm or superconducting variant of the coil is concerned, the superconducting one was preferred. The main arguments were the experience obtained with superconducting coils in INP, the possibilities of the USSR industry and the future perspectives of this technology.

The final decision on the structure and the construction of the detector was adopted by the beginning of 1990. In the period 1987-1990 an intense activity has been done for all parts of the detector. The barrel part of the joke has been produced and put at the VEPP-4M collider. The weight of the joke is equal to 700 t. The manufacturing of the superconducting coil soon will be finished. It has a diameter and length of about 3 m . The magnetic field is 1.8 T. The cryostat, the electrodes and the electronics is in production for the LKr calorimeter. 20 t of krypton have already been obtained. The necessary quantuty of CsI crystals was obtained for the endcap calorimeter. The design of the calorimeter will be finished soon. 50% of muon chambers is ready. In autumn 1990 will start the stretch of 16 thousand wires of the drift chamber. The system for the detection of the scattered electrons will be made soon. The work for the production of the vertex and microvertex detectors has been done.

The work at VEPP-4M collider is successful. The vacuum has been obtained in a half of the ring and it will be finished by the end of 1990. The construction of the elements of the straight sections is at the end. The work for getting the luminosity will start in 1991.

In spite of the strong effort done, the real status of the detector and of the collider is lagging behind the project adopted in 1987. This delay, equal to about one year, is due mainly to the scarcity of workshop power at INP for the production, to the scarcity oif financial support at INP and may be to some optimism in the planning of the work too.

In 1989 Swedish physicists from the Uppsala university joined the collaboration.

We hope that the high parameters of the KEDR detector, mainly the high resolution of the vertex detector usig microstrip semiconductor counters, the possibility of the identification of pions and kaons at momenta greater than 1 GeV/c,the high angular resolution of the liquid krypton calorimeter and the double tagging system with high energy resolution for the study of two-photon processes, will allow us to obtain new important informations.

The interest to the Υ-meson energy region grows with time. Recently in several laboratories projects of B-factories have been developed. The construction of a B-factory in Novosibirsk has already been approved. So when the experiment at VEPP-4M will be finished, the KEDR detector will be moved to the new collider.

This status report of the KEDR detector for VEPP-4M is based on the materials of the IV workshop on the KEDR detector, organized in Novosibirsk in December 1989.

2. Physics motivation.

2.1 Spectroscopy of b-quark bound states.

2.1.1 Measurement of the total and leptonic widths of Υ-mesons.

Fig. 2.1 shows the spectrum of $b\bar{b}$-mesons. More then 20 states are predicted below the threshold of $B\overline{B}$ production, three of them being $^3S_1$–states (Υ-mesons). Υ-mesons posses the same quantum numbers as the photon and can be directly observed in e^+e^- annihilation. Since their decay into hadrons proceeds via three gluons, Υ-mesons are narrow states with widths of dozens of keV. Up to now only the masses of Υ-mesons have been determined with high accuracy [1, 2], whereas the precision of the total and leptonic width measurements is rather low [1, 3].
In Table 2.1 we present the peak cross sections of Υ-meson production with radiative corrections σ_Υ (for a total energy spread of VEPP–4M at the Υ-meson of 4.5 MeV) and the continuum cross section σ_c

Table 2.1

Resonance	$\Upsilon(1S)$	$\Upsilon(2S)$	$\Upsilon(3S)$
σ_Υ (nb)	14.6	4.9	3.3
σ_c (nb)	3.2	2.9	2.7

2.1.2 Hadronic decays of Υ-mesons.

CLEO and ARGUS have measured the inclusive production of most of the vector and pseudoscalar mesons as well as of the octet and decouplet baryons [4]. ARGUS observed antideuterons in Υ(1S) and Υ(2S) decays [5]. The main characteristics are described by the LUND fragmentation model [6]. However, the production of particles decaying into photons (η, η') or into three particles (ω) has been less well studied. All of these experiments must be repeated at the Υ(2S) and Υ(3S).
Of great importance for QCD is the investigation of two-particle exclusive decays of Υ-mesons ($\pi^+\pi^-$, $K\overline{K}$, $p\bar{p}$, $\cdots$) and the comparison of their widths for different Υ-mesons and with similar charmonium decays [7].

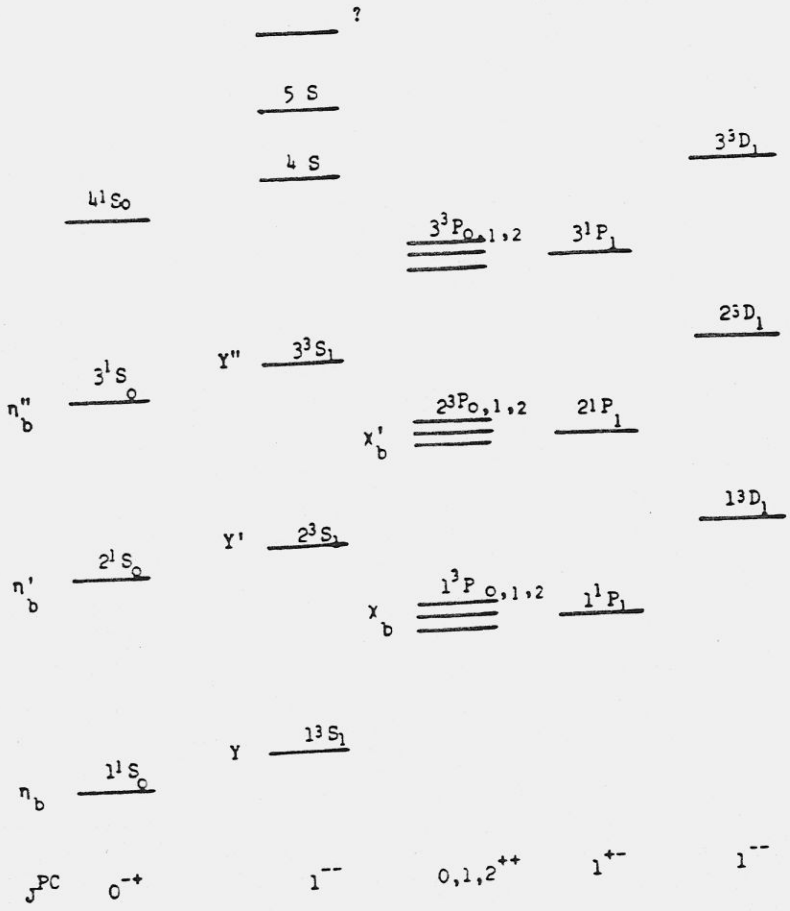

Fig. 2.1 Spectrum of $b\bar{b}$ mesons

The observations of these rather rare decays modes (branching ratios $\leq 10^{-5}$) will clarify the problem whether Υ-mesons are pure quarkonium states or contain some admixtures (molecular, gluonic etc.). CLEO set an upper limit for the branching ratio [8]:

$$Br(\Upsilon \to \rho\pi^0) < 6.6 \cdot 10^{-5} \qquad at \quad 90 \quad \% \quad C.L.$$

2.1.3 Hadronic transitions between Υ-mesons.
Hadronic transitions between Υ-states ($\Upsilon' \to \Upsilon\pi\pi$, $\Upsilon'' \to \Upsilon\pi\pi$, $\Upsilon'' \to \Upsilon'\pi\pi$) were observed both in $\pi^+\pi^-$ and $\pi^0\pi^0$ modes. The measured values of the branching ratios agree with theoretical predictions [9]. The two-pion mass distribution in the decays $\Upsilon' \to \Upsilon\pi^+\pi^-$, $\Upsilon' \to \Upsilon\pi^0\pi^0$ is also consistent with theoretical expectations [10]. However in the decay $\Upsilon'' \to \Upsilon\pi^+\pi^-$ this distribution is quite different and cannot be accounted for by currently existing theories [11]. The available statistics for the decays $\Upsilon'' \to \Upsilon\pi^0\pi^0$, $\Upsilon'\pi^+\pi^-$, $\Upsilon'\pi^0\pi^0$ are not sufficient to study their dynamics [11,12]. New measurements with good momentum resolution for charged particles and high detection efficiency for γ-quanta are needed.
Theory also predicts transitions with η-meson emission ($\Upsilon' \to \Upsilon\eta$, $\Upsilon'' \to \Upsilon\eta$) with branching ratio $\sim 3 \cdot 10^{-4}$ [9]. The best experimental upper limit obtained by the CLEO group is :

$$Br(\Upsilon' \to \Upsilon\eta) < 2 \cdot 10^{-3} \qquad at \quad 90\% \quad C.L.$$

2.1.4 ^3P_J states in the $b\bar{b}$ system.

Besides $^3S_1$ mesons, 6 ^3P_J states (χ_b and χ_b' mesons) have been observed. Their masses and widths of radiative decays of Υ-mesons into these states as well as branchings of χ_b mesons into lighter Υ-mesons were measured. For the χ_b series spins have been determined. Total widths are not well measured [13]. The study of the χ_b' series is much worse and no information exists about the hadronic decay modes of χ_b and χ_b' mesons.
The increase in the detection efficiency of photons and the improvement of energy resolution will allow the investigation of the hadronic decay modes when both a photon cascade and hadrons are detected. χ_b-states, with spin 0 and 2, decay into hadrons via two gluons and give a unique possibility to study gluonic jets with 5 GeV energy. Comparison of such hadronic decays with continuum events gives a direct comparison of the fragmentation of quark and gluon jets at the same energy.

2.1.5 Other $b\bar{b}$ states.

Up to now $^1S_0$ states have not been observed since the transition $\Upsilon \to \eta_b\gamma$ is a magnet-dipole one and the photon energies are small, so that the predicted branching ratios are $< 10^{-4}$.
One of the ways to observe the 1^1S_0 state is a cascade decay :

$$\Upsilon'' \to 2^3P_J + \gamma$$
$$\searrow^1 S_0 + \pi\pi$$

or

$$\Upsilon'' \to 1^1P_1 + \pi\pi$$
$$\searrow^1 S_0 + \gamma$$

In Ref. 9 a branching ratio of 0.4 % was predicted for the second decay. Recently M. B. Voloshin argued that its value is much lower, $\sim 10^{-4}$ [14] and that the decay $\Upsilon'' \to 1^1P_1\pi^0$ has a higher probability $\sim 2 \cdot 10^{-3}$.
Finally, η_b can be produced in $\Upsilon'' \to \eta_b\omega$ decays.
Unobserved are the D-states too. 1D states as well as η_b can be observed in the cascade decays of the $\Upsilon(3S)$. $^3D_1$-mesons having quantum numbers 1^{--} can be directly produced in e^+e^- collisions, but the expected leptonic widths are rather small ($\sim$ 1-3 eV) [15].
Theory also predicts hybrid states or meiktons consisting of bbg [16]. One of them with $J^{PC} = 1^{-+}$ and a mass of 10.49 GeV can be observed in M1 radiative decays of Υ''-meson. Meiktons with the quantum numbers of the photon which can be directly produced in e^+e^- annihilation can also exist. One cannot exclude that they are narrow. Some models predict the existence of additional vibrational states [17]. Experiment excludes new narrow resonances with a leptonic width greater than 40 eV in the energy region 10.34 - 10.52 GeV [18], with a width greater than 50 eV in the energy region 9.50 - 10.00 GeV and greater than 120 eV in the energy region 10.00 - 10.34 GeV [19].

2.2 Radiative decays of Υ-mesons.

The radiative decay of the Υ-meson into light hadrons is described by the diagram of Fig. 2.2.

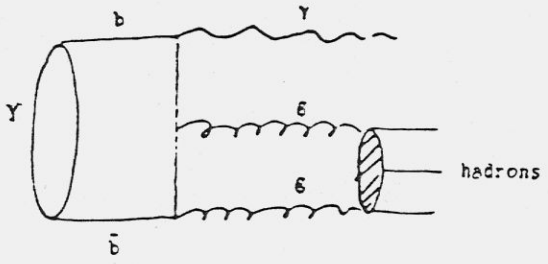

Fig. 2.2

The final hadronic system is in the C-even state and can contain different combinations of mesons formed of u, d, s and c-quarks. One can expect that in a manner similar to the decays of the J/ψ-meson at high photon energies and respectively small masses of hadronic system, both well-known mesons (π^0, η, η', f, f') and new states will

be observed in Υ-meson decays. In contrast to the two-body hadronic decays, the decrease in the radiative decay width compared to the case of the J/ψ is proportional to $(Q_b/Q_c)^2 \cdot (M_{J/\psi}/M_\Upsilon)$ only [7].
In the recent experiments of CLEO [8], Crystal Ball [20] and ARGUS the upper limits for the branching ratios of such decays were obtained. For the decay mode $\Upsilon \to \gamma f_2$ the upper limit $< 4.8 \cdot 10^{-5}$ is comparable to the theoretical predictions [21].
It is clear that the hadronic system produced via two gluons is an ideal place to look for glueballs and other exotic phenomena. A limit close to the predictions of the Standard Model [22] has been obtained, searching for the Higgs boson in the decay $\Upsilon \to \gamma + H$ [20].
We have to note finally that the analysis of the spectrum of direct photons from Υ-mesons decays allows the most accurate determination of α_s and Λ [23]. Experimental spectra [24] are consistent with the leading order of perturbation theory [25], whereas for comparison with more detailed theoretical models [26] a significant increase in statistics and photon energy resolution is needed.

2.3 Investigation of mesons with naked beauty.

In contrast with the first three Υ-mesons, the $\Upsilon(4S)$ with a mass of 10580 MeV is higher than the threshold of naked beauty production and is not narrow ($\Gamma_{tot} \simeq$ 24 MeV). The $\Upsilon(4S)$ with almost a 100 % probability decays in $B\overline{B}$, and can be considered as a factory of B-mesons or more precisely light B-mesons: $B_u(\bar{b}u)$ and $B_d(\bar{b}d)$. All characteristics are known for B_u and B_d together, the only exception is their exclusive hadronic modes and, from these, their masses.
Because of the larger mass of the b-quark and higher precision of the QCD corrections, B-mesons are considered as a good laboratory to study the Standard Model, according to which the spectator diagrams of Fig. 2.3 are dominant in B-meson decays:

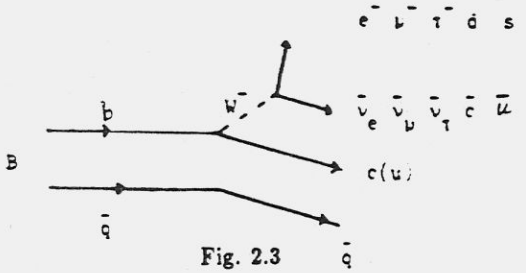

Fig. 2.3

Information about exclusive hadronic modes has been obtained by CLEO and ARGUS [27]. Their results are consistent with each other. The sum of the measured branchings is 11 %, while the total hadronic branching ratio is expected to be about 75 %. Further progress can be made with higher detection efficiency allowing the detection of high multiplicity decay modes and simultaneous reconstruction of both B-mesons.
Semileptonic decays of B-mesons are very important in order to understand the mag-

nitude of b → c and b → u couplings. The detailed analysis of the leptonic momentum spectra performed in ref. 37 shows that the b → c transition dominates, and

$$\frac{(b \to u)}{(b \to c)} \simeq 0.02$$

or, for the elements of the Cabibbo-Kobayashi-Maskawa matrix

$$\left|\frac{V_{ub}}{V_{cb}}\right| \simeq 0.1$$

This analysis is strongly model dependent. Another approach involves a search for exclusive B-meson decays into charmless (or strangeless) states, for example $B^0 \to \pi^+\pi^-$, $B^- \to \rho^0\pi^-$. This approach gives [37] :

$$\left|\frac{V_{ub}}{V_{cb}}\right| < 0.2$$

To clarify the picture one must increase substantially the statistics of the B-meson decays, to measure the lifetimes of B_u and B_d-mesons separately and to observe the semileptonic decays into τ-leptons. Observation of a purely leptonic decay $B \to \tau\nu_\tau$ can provide the most model independent measurement of f_B.

Of great interest is the search for $b \to s$ processes proceeding in the Standard Model through loop diagrams sensitive to new physics. The sensitivity of current experiments is not sufficient to observe $b \to s$ transitions at expected SM branchings, but they indicate that there is no enhancement of the corresponding amplitudes.

The investigation of B^0 - $\overline{B^0}$-mixing, described by the box diagrams of Fig. 2.4, is of great interest too.

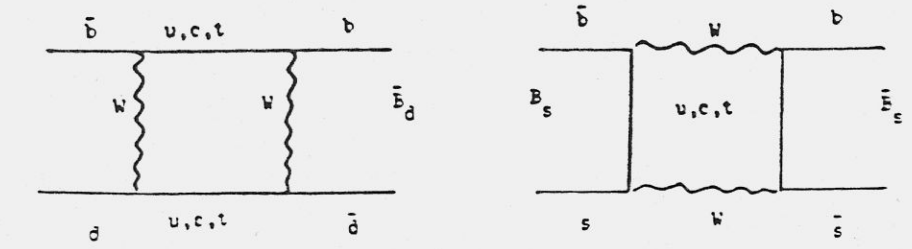

Fig. 2.4

Predictions of the Standard Model are not very reliable because of the unknown t-quark mass. Recent experimental data from ARGUS and CLEO indicate at a notable B-mixing (20 %). There is also evidence for the mixing (B_d or B_s) from the UA1 and MAC experiments [28]. The investigation of this problem has only recently begun.

The Standard Model predicts substantial CP-violation in B-decays. Its observation would allow one to discriminate between existing models. The most convenient way

to observe this is to use $B_d\overline{B_d}$-mixing with an interference of amplitudes :

$$\begin{array}{ccc} B_d & \longrightarrow & f \\ & \searrow\nearrow & \\ & \overline{B}_d & \end{array}$$

where f is a state common to B_d and $\overline{B_d}$ decays: ψK_s, $D\overline{D}K_s$, D^+D^-, $\pi^+\pi^-$, $K_s\rho$. The expected value of the amplitude is ~ 0.1; however the branching ratios are very small and require very high statistics.

Besides B_d and B_u-mesons their vector partners $B^*_{u,d}$ have been observed. Theory predicts more than 30 new particles with a b-quark and a mass less than 6 GeV. The cross section of their production are large enough, so that one believes that an integrated luminosity of about 100 pb^{-1} will be sufficient for their discovery. The detailed investigation of the energy range from 10.8 up to 12 GeV will clarify the problem of the $\Upsilon(5S)$ etc. [29].

2.4 Investigation of the continuum.

Below we list briefly some interesting problems:

1. Measurements of R with high accuracy to determine QCD parameters. A large solid angle of the detector combined with a good particle identification will provide much lower systematic uncertainties due to the dependence of the detection efficiency on the production model.
2. Study of quark and gluon fragmentation by the comparison of the inclusive yield of different mesons and baryons. To this end good separation of π^0 and η-mesons is needed.
3. Investigation of the correlations between identical final state particles to determine the size of the source of their production, comparison with the Υ-meson.
4. Study of the τ-lepton physics. At the energy of 10 GeV the cross section of $\tau^+\tau^-$ pair production is $\simeq 0.9$ nb, so that the integrated luminosity of 100 pb^{-1} corresponds to $9\cdot10^4$ $\tau^+\tau^-$ pairs. The high detection efficiency allows the investigation of decay modes with high multiplicity (particularly with π^0 and η-mesons), the search for possible deviations from the Standard Model and the improvement of the limit on the mass of the τ-lepton neutrino.
5. Study of production and properties of charmed mesons and baryons (F, F^*, Λ_c, $\cdots$). Estimates indicate that 100 pb^{-1} correspond to $5\cdot10^4$ events, containing such particles.

2.5 $\gamma-\gamma$ Physics

A tagging system providing high resolution in $\gamma-\gamma$-mass W ($\sigma_W \simeq$ 15–20 MeV) and sufficiently high detection efficiency will allow qualitative improvement of our understanding of γ - $\gamma \rightarrow$ hadrons physics in the mass region from 0.5 up to 4 GeV. Together with radiative decays of Υ-mesons, it will provide information which is complementary to that from the single photon channel of $e^+e^- \rightarrow$ hadrons. Below we list some

problems which are interesting for double-tag experiments, i.e. experiments in which both scattered electrons are detected.

- Measurement of the total cross section $\gamma\gamma \rightarrow$ hadrons can be performed with much better accuracy than in previous experiments [30,31] allowing comparison to theory. The W dependence of the number of detected hadrons is shown in Fig. 2.5 for the integrated luminosity of 100 pb^{-1}. The attractive feature of the double-tag experiment is the possibility of model-independent reconstruction of the photon-photon mass W. Good resolution in W is of special importance at low masses where processes with different mass dependence contribute to the total cross section and fine structure of the cross section should be resolved.

- Determination of the properties of C-even resonances is independent of a specific final state. Measurement of the two-photon widths provides important information about the quark structure of these states. Only resonances with $J^{PC} = 0^{-+}$ and 2^{++} belonging to the nonets of light quarks have been well studied [32].
  Very interesting for theory are $c\bar{c}$ resonances. Although a two-photon width of η_c was recently measured in several experiments [33], its accuracy is still bad and needs impovement to allow comparison to theory. Situation with χ_0 and χ_2 is much worse because only single experiments exist. For mentioned above values of tagging system parameters and the integrated luminosity of 100 pb^{-1} one expects about 100 events each of η_c, χ_0, χ_2 production allowing a 10 % accuracy in their two-photon width.
  One can also expect improvement of the accuracy in measuring $a_0(980)$ and $f_0(975)$ two-photon widths as well as placing a factor of 5 better upper limits for two-photon widths of $\eta(1430)$, $f_0(1590)$, $f_2(1690)$ and X(2220) resonances candidates to glueballs or other exotics.

- One should try to study the exclusive channel γ - $\gamma \rightarrow \pi\pi$ at small W < 600 MeV. There is rather contradictive evidence for some excess over the Born contribution in γ - $\gamma \rightarrow \pi^+\pi^-$ absent in γ - $\gamma \rightarrow \pi^0\pi^0$ [33]. There are speculations relating this effect to the anomalies in $\pi\pi$ transitions of Υ (3S) and J/ψ [34].

- Double tagging allows determination of the inclusive spectra of π, K, ρ in $\gamma\gamma$ collisions which are sensitive to structure functions and fragmentation. Inclusive spectra of η and η' may facilitate a search for exotic states like $f_0(1590)$, $f_2(1720)$, etc.

- In the entire energy range a search for new narrow C-even bosons predicted in some composite models [35] will be possible with a sensitivity by one-two orders of magnitude better than that of the TPC/2 group which performed such a search at 4.5 < W < 19 GeV and placed an upper limit on the two-photon width from 50 keV to 10 MeV [36].

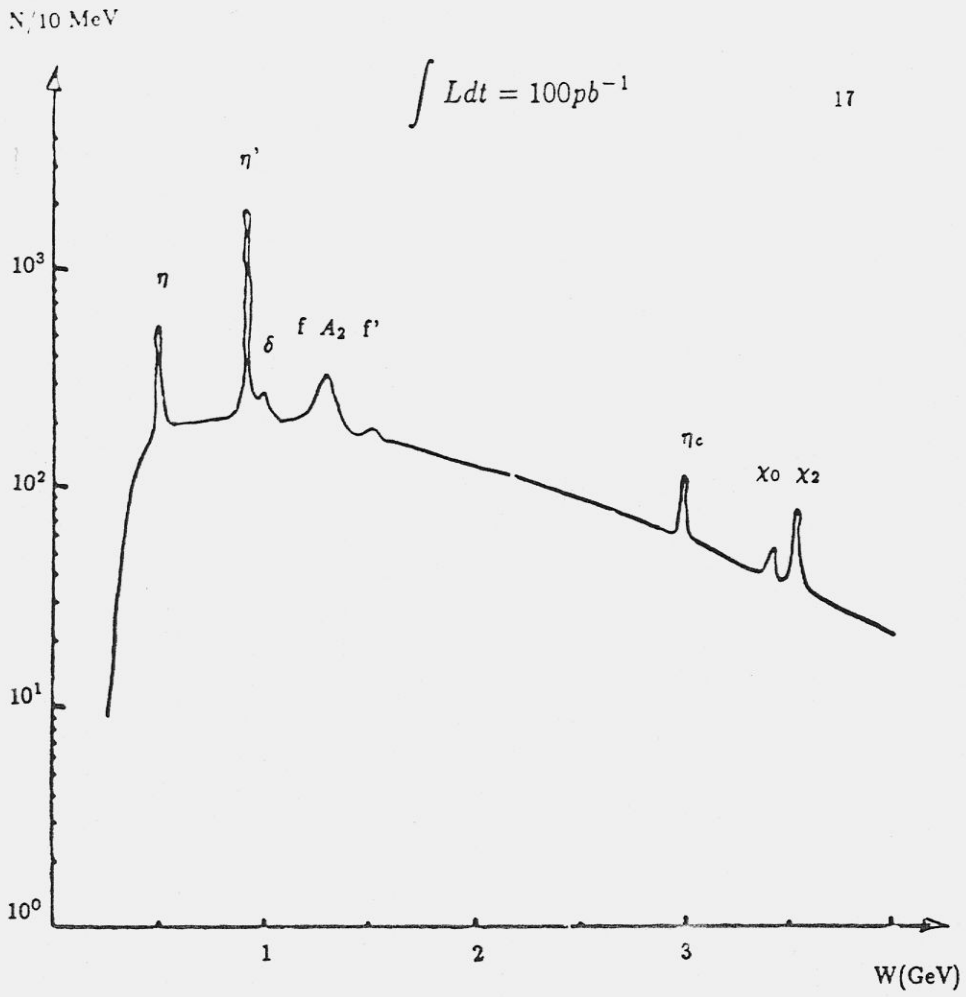

Fig. 2.5 Number of detected hadrons vs $\gamma\gamma$ mass

References

1. Review of Particle Properties, Phys. Lett. 204B (1988) 1
2. S. E. Baru et al., Z. Phys. C30 (1986) 551
3. A. Bizzeti, Proc. of XXIV Intern. Conf. on High Energy Phys., Munich, 1988
4. S. Behrends et al., Phys. Rev. D31 (1985) 2161
   H. Albrecht et al., Z. Phys. C39 (1988) 177
   H. Albrecht et al., Z. Phys. C44 (1989) 547
5. A. Babaev et al., Phys. Lett. 236B (1990) 102
6. B. Andersson et al., Phys. Scr. 32 (1985) 574
7. V. L. Chernyak and A. R. Zhitnitsky, Phys. Rep. 112 (1984) 173
8. F. Fulton et al., Preprint CLEO 89-7
9. Y. P. Kuang and T. M. Yan, Phys. Rev. D24 (1981) 2874
10. T. M. Yan, Phys. Rev. D12 (1980) 1652
    M. Voloshin and V. Zakharov, Phys. Rev. Lett. 45 (1980) 688
    V. A. Novikov and M. A. Shifman, Z. Phys. C8 (1981) 43
11. M. Goldberg, Proc. of XXIV Intern. Conf. on High Energy Phys., Munich, 1988
12. G. Mageras et al., Phys. Lett. 118B (1982) 453
13. W. Walk et al., Phys. Rev. D34 (1986) 2611
14. M. B. Voloshin, Yadernaya Fizika 43 (1986) 1571
15. P. Moxhay and J. L. Rosner, Phys. Rev. D28 (1983) 1132
16. P. Hasenfratz et al., Phys. Lett. 95B (1980) 299
17. W. Buchmuller and S. H. H. Tye, Phys. Rev. Lett. 44 (1980) 850
18. E. Rice et al., Phys. Rev. Lett. 48 (1982) 906
19. A. E. Blinov et al., Preprint INP 85-99, Novosibirsk, 1985. Submitted to Z. Phys.
20. J. Lee-Franzini,Proc. of XXIV Intern. Conf. on High Energy Phys., Munich,1988
21. J. G. Korner et al., Nucl. Phys. 229B (1983) 115
22. F. Wilczek, Phys. Rev. Lett. 39 (1977) 1304
    M. I. Vysotsky, Phys. Lett. 97B (1980) 159
23. M. Chanowitz, Phys. Rev. D12 (1975) 918
    L. B. Okun and M.B.Voloshin, Preprint ITEP–95, Moscow, 1976
24. R. D. Schamberger et al., Phys. Lett. 138B (1984) 225
    S. E. Csorna et al., Phys. Rev. Lett. 56 (1986) 1222
25. S. J. Brodskyet al., Phys. Lett. 73B (1978) 203
26. D. M. Photiadis, Phys. Lett. 164B (1985) 160
    R. D. Field, Phys. Lett. 133B (1983) 248
27. H. Albrecht et al., Phys. Lett. 185B (1987) 218
    C. Bebek et al., Preprint CLNS 86/742, Cornell, 1986
28. M. G. D. Gilchriese, Rapporteur Talk at the XXIII Inter. Conf. on High Energy Physics, Berkeley, July 1986
    H. R. Band et al., Phys. Lett. 200B (1988) 221
29. D. M. J. Lovelock et al., Phys. Rev. Lett. 54 (1985) 377
    D. Besson et al., Phys. Rev. Lett. 54 (1985) 381
30. D. Bintinger et al., Phys. Rev. Lett. 54 (1985) 763

31. S. E. Baru et al., Preprint INP 86-108, Novosibirsk, 1986
32. H. Kolanoski, Preprint DESY 88-167, 1988
33. R. N. Cahn, Proc. of the XIV Inter. Symp. on Lepton and Photon Interactions, Stanford, 1989
34. A. Falvard et al., Phys. Rev. D38 (1988) 2706
35. F. M. Renard, Phys. Lett. 126B (1983) 59
    U. Baur et al., Phys. Lett. 135B (1984) 313
36. H. Aihara et al., Phys. Rev. Lett. 57 (1986) 3245
37. H. Albrecht et al., Phys. Lett. 234B (1990) 409
    P. Avery et al., Phys. Lett. 183B (1987) 429

3. Collider VEPP-4M

3.1 Description of the complex

VEPP-4M is a facility constituted by a linac at an electron energy of 50 MeV, a synchrotron at an energy of 350 MeV, an intermediate storage ring VEPP-3 with a maximum energy of 2.2 GeV and the storage ring VEPP-4M. Fig. 3.1 illustrates the arrangement of the devices in the complex.

The linac and the synchrotron provide a mean rate of positron accumulation in the VEPP-3 of about $2 \cdot 10^8$ particles/s and that of electron accumulation of about $2 \cdot 10^9$ particles/s. The positrons are produced by a conversion of 50 MeV linac electrons with further collections of 7 MeV positrons in the $\pm 3\%$ energy range before their injection into the synchrotron. The electrons from the linac are directly injected into the synchrotron. With a change of sign of the particles, the polarity reversal of the magnetic field in the synchrotron and storage ring takes place.

Injection into VEPP-4M occurs at an energy of 1.8 GeV. In view of this, the physics run interrupts once every two hours and, hence, the magnetic field in the storage ring reduces, the positrons and electrons are injected in turn and the magnetic field returns at the initial level. The pause in the work is usually about 15 min and, thus, the maximum luminosity differs from the average one no more than by a factor 1.5.

3.2 Storage ring VEPP-4M

The storage ring VEPP-4M is designed to operate with electron and positron beams at an energy up to 6 GeV. The circumference of the storage ring is 366 m and is composed of two semi-rings with radius 45.5 m and two straight sections, each 40 m long.

The semi-rings are filled with FODO-type cells with combined focusing and turning. In the centre of each semi-ring, on the 18^0 arc, these elements are replaced by an equivalent magnetic structure with a larger vertical aperture. This offers the possibility of arranging here the separation of electron and positron orbits in the vertical direction to avoid the beam-beam interaction, during operation with two electron and two positron bunches.

One of the straight sections serves mainly as utility one. In it there are input magnets, inflectors plates, cavities of the RF system. For the power supply of the cavities, a 1 MW RF generator at a frequency of 180 MHz is being designed. The collision point in the straight section has no use in experiment. Here the electron and positron orbits are separated in the vertical plane.

The second straight section is entirely involved in the experiment. The detector is located on a 4 m long section in the centre of the straight section. The remaining part is occupied by the lattice. It is assumed to be of variable shape depending on the character of the experiment. At the first stage, besides the arrangements of low beta-functions at the collision, the optics of the straight section enables to solve the problem of detection and measurement of the energy of electrons leaving the collision point in photon-photon interaction. For details see Section 5.

Here below are listed the basic parameters of the storage ring VEPP-4M:

Maximum energy, E	6 GeV
Betatron oscillation frequency, ν_x, ν_z	8.53, 7.57
Compaction factor, α	0.017
Values of the dispersion and beta-functions at the collision points ψ_x, β_x, β_z	80 cm, 5 cm, 75 cm
Radiation losses of energy per revolution (here and below E = 6 GeV)	3.5 MeV
Emittance, ϵ_x	$2.4 \cdot 10^{-5}$ cm rad
Energy spread, σ_ϵ	10^{-3}
Frequency of the RF generator	180 MHz
RF multiplicity, ν	220
RF voltage, eV	8 MeV
Power of RF generator	1 MW
Synchrotron oscillation frequency, ν_s	0.03
Bunch length	4 cm

3.3 Luminosity

Fig. 3.2 shows the calculated luminosity of VEPP-4M in 4-6 GeV range of the beam energy. The diagram 1 corresponds to the luminosity at a vertical 5 cm beta-function at the collision point at a natural value of the beam emittance. This luminosity can be achieved after the several months of the VEPP-4M commissioning.

Diagram 2 shows the luminosity achieved at the same beta-function with an increase in the beam emittance up to $4 \cdot 10^{-5}$ cm rad. For these purposes, a superconducting three-pole wiggler magnet is assumed to be installed in the middle of each semi-ring. The desing and production of this wigglers will start after the begining of the VEPP-4M operation and will need about two years for a completeness.

Diagram 3 is referred to the situation when the increase in emittance accompanied with a two-fold reduction of the beta-function at the collision point. Such a reduction of this function must be followed by a proper shortening of the bunch length. For bunching, a section of superconducting cavities is suggested to be placed in the utility straight section. The latter increase in the luminosity is very problematic and will need an experiment study on VEPP-4M.

Beam currents corresponding to the three regimes discussed above are shown in Fig. 3.3.

3.4 Longitudinal polarization

At present, the project is prepared to generate longitudinally polarized colliding beams at VEPP-4M [1]. The project is based on the well known scheme according to which the vertical direction of the spin is at first converted to a horizontal one using solenoidal spin rotators and then to the horizontal by a 90 rotation in the horizontal plane in the magnet with vertical magnetic field. The symmetrical part of the scheme after the collision point is used to restore the initial vertical direction of the spin in the major part of the ring. Since the angle of rotation of the spin in the horizontal plane depends on the particle energy, the energy of the Υ-resonance is considered optimal when the degree of the longitudinal polarization must be maximum. The longitudinal polarization degree vs. the beam energy is shown in Fig. 3.4. Considerable losses of polarization at some energies are attributed to the manifestation of various spin resonances.

3.5 Status of the work and plans

At present, all parts of the new units of VEPP-4M have already desinged and are being manufactured. The transport channel from VEPP-3 to VEPP-4M is fully assembled and tested with the electron beam. All standard cells of VEPP-4M with the vacuum chamber are installed in the right position and the designed vacuum is achieved. As a result a half of the ring is ready for the beam test. By the end of 1990 year all the new units of utility and experimental straight section must be manufactured. It allows to begin the commissioning of the VEPP-4M in the begining of 1991.

References

1. Yu.I.Eidelman et al., Project of obtaining longitudinal polarization at the storage ring VEPP-4M. Proc. of the 10th National Meeting on Charged Particle Accelerators, Dubna, 1986.

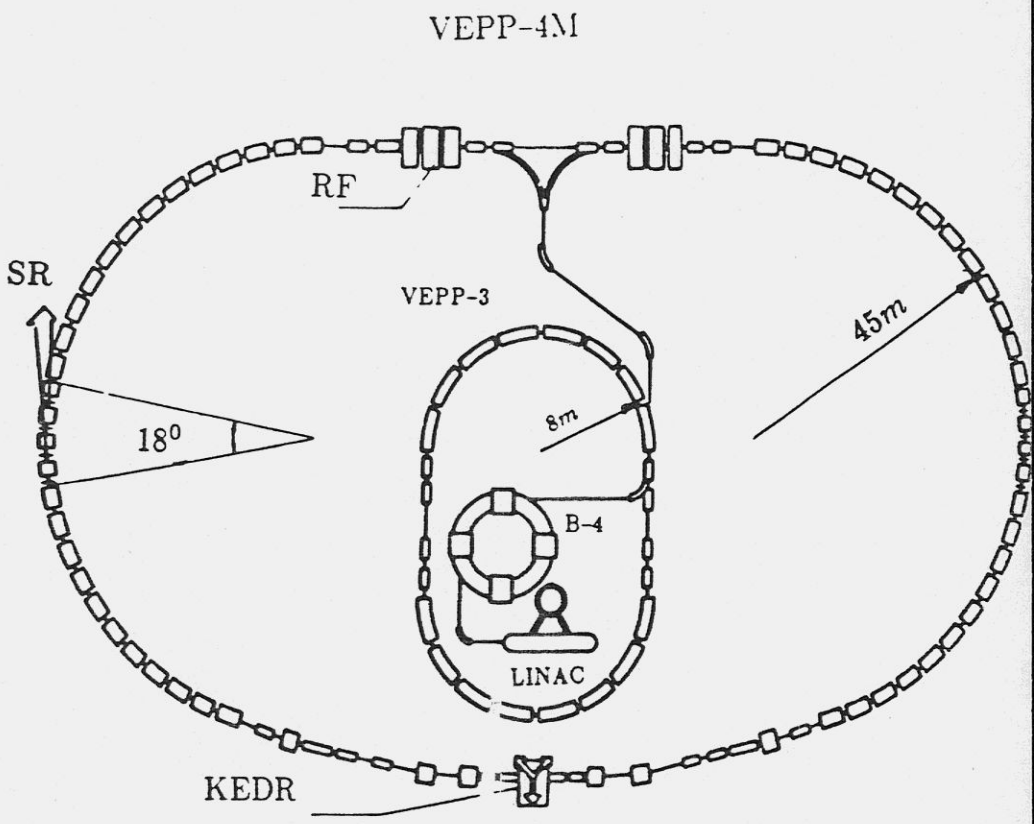

Fig. 3.1 The VEPP-4M complex

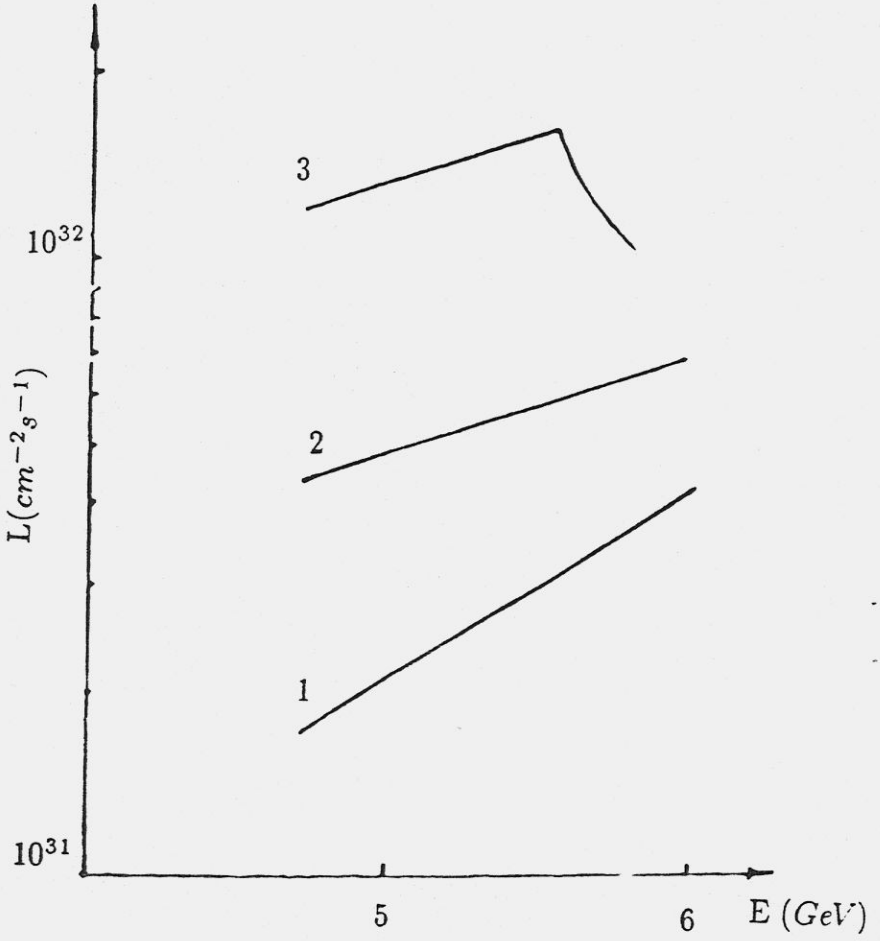

Fig. 3.2 Luminosity of the storage ring VEPP-4M

diagram 1: 5cm β-function and natural emittance at the collision point.
diagram 2: emittance increased up to 4 $10^{-5} cm\ rad.$
diagram 3: 2.5cm β-function at the collision point

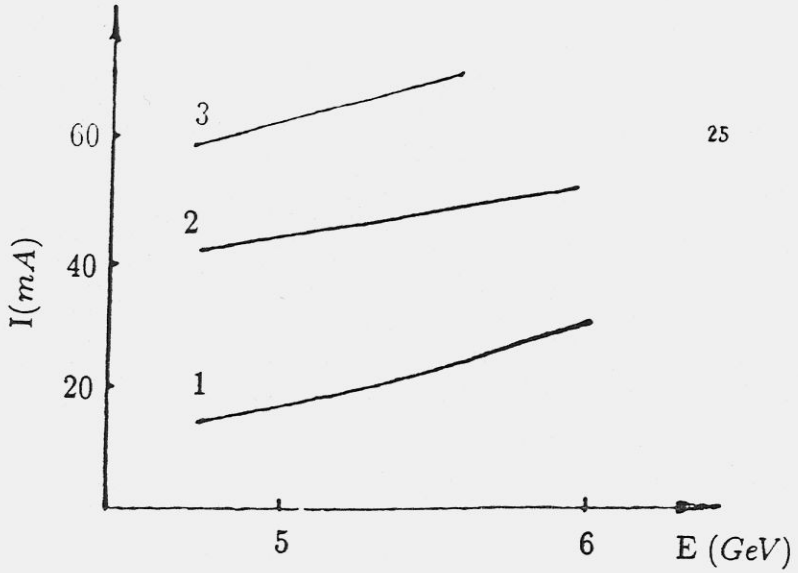

Fig. 3.3 Beam current; diagrams 1,2,3 correspond to the regimes of Fig. 3.2

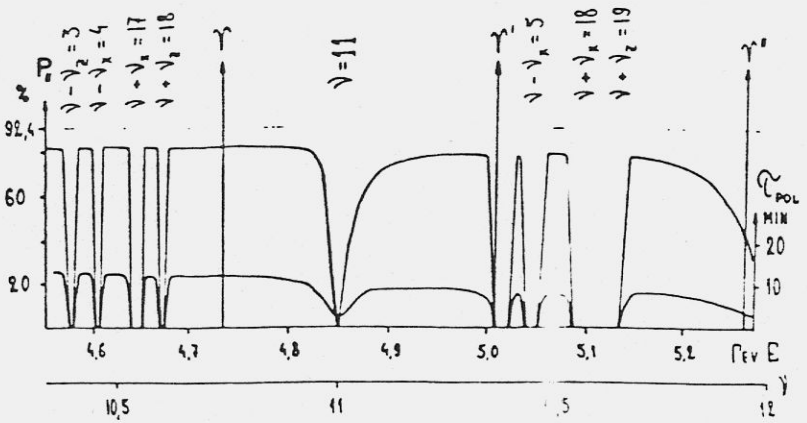

Fig. 3.4 The dependence of the polarization time and the longitudinal polarization on the beam energy

4. General layout of the detector

The general layout of the detector is shown in Fig.4.1. Starting from the interaction point, the detector KEDR has the following systems :

1) Vacuum chamber 1 with a thin wall berillium beam pipe in the interaction area. Superconducting compensating solenoids 14 with magnetic field up to 7 T, symmetric with respect to the interaction point, are also used as cryogenic pumps.
2) Tracking system for charged particle momentum and position measurements, consisting of a silicon microvertex detector 2, a vertex detector 3 and a drift chamber 4.
3) Hadron identification systems, consisting of longitudinal 5 and endcap 11 aerogel Cherenkov counters and one layer of TOF scintillation counters, consisting of longitudinal 6 and endcap 12 counters.
4) Electromagnetic calorimeters, based on liquid krypton 7 and CsI(Na) crystals 13.
5) Magnet superconducting coil 8 providing a field up to 1.8 T and an octagonal shape magnetic yoke 9 serving also as hadron absorber.
6) Muon system 10 and 16, based on streamer tubes.

Moreover, an electron tagging system for the study of two-photon processes is situated behind the quadrupole lenses.

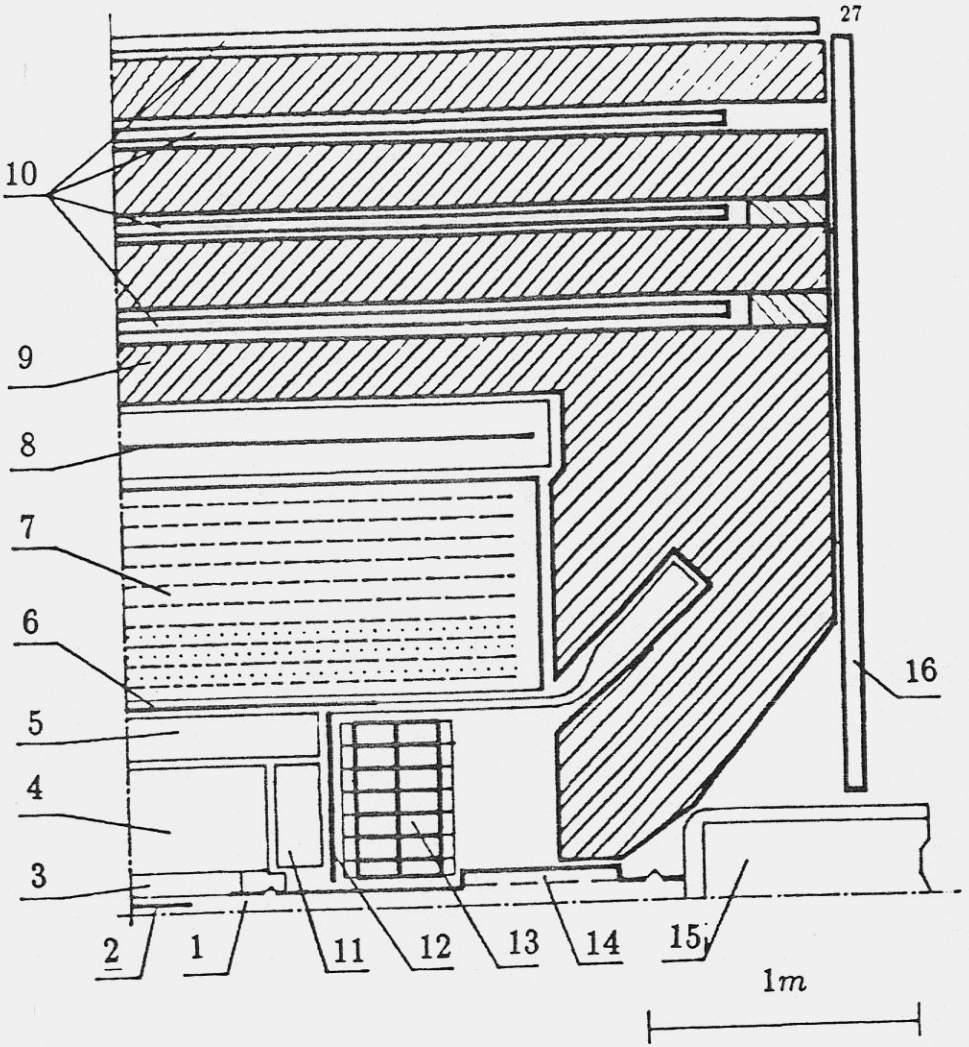

Fig. 4.1 1 - Beam pipe; 2 - Silicon microvertex detector; 3 - Vertex detector, 4 - Drift chamber; 5,11 - Hadron identifier; 6,12 - Time of flight; 7 - LKr calorimeter; 8 - Superconducting coil; 9 - Yoke; 10,16 - Muon chambers; 13 - CsI endcap calorimeter; 14 - Compensating solenoid; 15 - Quadrupole

5. Electron tagging system

The diagram of the two-photon production $e^+e^- \to e^+e^-$ X is shown in Fig. 5.1.

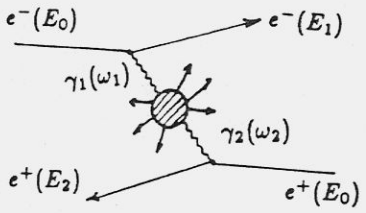

Fig. 5.1

Electron and positron radiate virtual photons which produce a particle system X with even C parity. Distribution over the photon energy and angle is given approximately by

$$N(\omega)d\omega d\theta_\gamma = \frac{\alpha}{\pi}\cdot\frac{d\omega}{\omega}\cdot\left(1-\frac{\omega}{E_0}+\frac{\omega^2}{2E_0^2}\right)\cdot\frac{d\theta_\gamma^2}{\theta_\gamma^2+m_e^2/E_0^2}$$

One can see from this formula that the photon energies follow roughly the characteristic bremsstrahlung spectrum $\sim \frac{1}{\omega}$ and photons are radiated mainly at very small angles of the order of m/E. The angles of the scattered leptons (traditionally called "tagged electrons" or "TE") are related to the photon angles by the momentum conservation and, therefore, are small too.

The kinematical variables of the $\gamma\gamma$ system can be expressed in terms of the variables of TE: photon energy corresponds to a TE energy through energy conservation law , $\omega = E_0 - E$, and the TE's angle characterises photon's "virtuality". In principle, the detection of both TE fixes the kinematics of $\gamma\gamma$ system with a precision determined by the resolution of the detection system.

The problem of the TE detection arises from the fact, that as a rule TE come out from the interaction point with very small angles, so the tagging system should be located as close to the beam as possible (especially if one wants to study the small invariant mass region when electrons lose only a small part of their energy). An important step in the development of the instrumentation for two-photon processes was made by providing detectors with a special system to tag a scattered electron - Electron Tagging System (ETS). ETS should fulfill two basic requirements: high detection efficiency and the maximal accuracy in the measurement of TE energy.

In order to reach a high efficiency in the detection of the electrons coming out at zero angles, it is of great importance to take into account the kinematics of the two-photon processes. This can be done by deflecting from the beam those electrons which have lost part of their initial energy. The bending magnet applied for this together with the doublet of mini-β quadrupoles would be natural to use as a strong focusing magnet spectrometer to measure TE energy.

The scheme of ETS is presented in Fig. 5.2. TE, coming out from the interaction point passes through the main solenoid,the compensating solenoid, the quadrupole lenses L_1 and L_2 and the bending magnets M_1 and M_2. TE is detected by four tagging systems TS_1, TS_2, TS_3 , TS_4 , whose basic parameters are given in the Table 5.1. The focus energy is the energy of TE, whose coordinate in TS due to the focusing properties of quadrupoles is independent of TE's emission angle.

Table 5.1

Number of TS	Region of tagged energies (*)	Focus Energy	Size of TS (cm)
1	0.40–0.60	0.58	10
2	0.60–0.73	0.66	6
3	0.73–0.85	0.80	10
4	0.85–0.92	0.98	18

(*) related to the energy beam

So mini-β quadrupoles at the same time are also the essential part of strong focusing magnet spectrometer. This solution allows to move quadrupoles closer to the interaction point to increase the luminosity and to improve energy resolution for TE as compared to a usual magnetic spectrometer.

For the particles emitted at zero angle from the interaction point the coordinate in TS is unambiguously determined by their energy. The TE angular distribution, despite its sharp peaking behaviour, destroys this unambiguity.It means that the non zero emission angle leads to an error in the energy measurement. But for the TE with the focus energy such an unambiguity restores. The more is the deviation of TE's energy from the focus energy, the larger is the error in energy measurement due to unknown emission angle. This is why ETS is divided into four TS, providing a small enough error in energy measurements in a wide TE energy region.

The resolution of the reconstructed invariant mass of the two-photon system is shown in Fig. 5.3.

Double tag detection efficiency is presented in Fig. 5.4. In these calculations TE was considered as "detected" if it not only met all aperture requirements and hit one of TS but also the error in TE energy measurement not exceeded 40 MeV.

The ETS coordinate system is based on drift tubes (DT) hodoscopes. Each TS includes one hodoscope, designed as an independent module which contains six detecting planes (see Fig. 5.5). A detecting plane is made of two rows of stainless steel drift tubes, 6 mm diameter, 90 μ m wall thickness. The distance between tubes in the row is equal to 8 mm, the second row is shifted as a whole by 4 mm. Anode wires are streched with a displacement of 0.3 mm from the center of the tube, displacements having an opposite sign in different rows. This allows to remove "left-right" umbiguity during track reconstruction. In TS_1 , TS_2 , TS_3 modules each row consists of 12 tubes, TS_4 module has the row of 24 tubes. The total number of tubes in ETS is 1440.

Each DT is read out by preamplifier and shaper located on the hodoscope. The rise of the output signal is 5-7 ns and the time decay is about 25 ns. Front-end electronics is arranged into independent blocks of 12 channels which are mounted directly on the wire pins. Logical signals from these blocks are transported to the intermediate block of electronics to match the front-end and digitizing electronics. Analog to digital conversion is made by blocks following a special standard (see the chapter " Electronics"). Time intervals are measured by the method of direct count 2 ns per channel. The threshold of electronics is $7 \cdot 10^{-15}$ Q.

The average spatial resolution of DT, measured with a prototype of 11 tubes, was 300 μ m at the gain of $5 \cdot 10^5$. By increasing the gain up to $2 \div 4 \cdot 10^6$, a resolution of 200 μ m is obtainable.

The most crucial problem which should be solved at the design of ETS is the preservetion of longterm reliable performance of the system in high count rate conditions. For instance, a rate of bremsstrahlung electrons in the 5 mm layer of beam orbital plane reaches 200 kHz. To manage this problem, the system will be operated at the lowest possible gain. The opportunity of hodoscope movement has been considered and this allows to decrease the density of irradiation dose by 10 times approximately.

To study the problem of radiation hardness several single tube modules were constructed using the materials employed for the production of ETS. They were irradiated by an isotope source Sr^{90} and X- ray tube.

During the irradiation of DT which was blown through with a gas mixture of Ar and CO_2, substantial gain deterioration of 300 % cm/Q has been observed, which makes this mixture unsuitable for the system. At the moment a 90 % CF_4 +10 %C_4H_{10} gas mixture looks quite satisfactory. In this case the dose of 5 Q/cm does not show any noticeable variation in the gain. The reproducibility of irradiation results and the influence of the irradiation rate on the damage of the system require more detailed studies.

Each TS includes a scintillation hodoscope to realize the possibility of rejecting a "horizontal region". Hodoscope consists of 10 plastic scintillator counters read out by the photomultiplier FEU-60. The regulated gap between opposite counters determines the region to be rejected.

The dominant background in ETS comes from electrons which lose energy by beam bremsstrahlung. The cross section of this process is so large that the counting rate of background electrons will be $dN/dt = 1.8 \cdot 10^6$ Hz at the luminosity $L = 2 \cdot 10^{31} cm^{-2} s^{-1}$, i.e. $\sim$ 2 particles per collision. Let's enumerate various methods to reduce the

background from bremsstrahlung.

1. The rejection of horizontal region.

The anglular distribution of bremsstrahlung photons is more sharp compared to that of two-photons ones. This fact can be used for background suppression. One can improve the effect to background ratio by selecting a TE emission angle with respect to the orbit plane $|\Theta_{z0}| < \Theta_0$. The main disadvantage of this way is a significant loss in the detection efficiency.

2. The determination of the interaction point from the time of flight of tagged electrons.

One of the ways to reduce the background from bremsstrahlung is to measure the time when TE come to the tagging system. The bunch is about 5 cm long, but TE from the two-photon process should originate from the same point of the bunch as hadrons that came to the central part of the detector. It's necessary to measure the vertex of interaction in the detector. In this case one can reduce the background by the determination of the initial point of TE from the time of flight and comparing it with the vertex. It is clear that the quality of such a method of reducing the background is determined by the time resolution of the TOF systems which are proposed to be located behind TS. This work is in progress, and we have a resolution of about 30 ps.

3. The lead-scintillator sandwich.

The most proper way to suppress background would be the detection of bremsstrahlung photons. Howewer, it's hard enough to separately measure the energies of every photon because there are few photons per every collision with very small angles with respect to the beam axis. Use of calorimetry permits to measure only the sum of all photon energies together with those which don't match ETS acceptance.

One can use this information in order to suppress the background by selecting those tagged electrons which have the sum of lost energies corresponding to energy deposition in the calorimeter.

For this purpose there will be two lead-scintillator sandwiches (at both directions from the interaction point) to detect the photons that come at small angles from the interaction point. The sanwich consists of 4 blocks having 25 layers each. A layer consists of 1 mm thick lead and 5 mm thick scintillator plates. So the overall length of the calorimeter is 18 radiation lengths. Each block is read out by a plane-parallel plexiglass light guide coupled to 4 photomultipliers (FEU-110).

4. The pair spectrometer.

For a more effective suppression of the background it is necessary to separately measure the energy of every photon. It can be realized with the help of a pair spectrometer which consists of thin convertors in the magnetic field and a system of coordinate detectors. In this case photons produce a e^+e^- pair in various convertors. The

photon energy is determined from the curvature of electron and positron tracks in the magnetic field.
It is suggested to use semiconductor strip detectors with size 50x50 mm^2 and the step between strips 50 μ m. The structure of the pair spectrometer is shown in Fig. 5.6. The detectors are located behind every convertor and between them. So there are three points to determine the curvature of the particle track. There is a lead-scintillator sandwich at a distance of 2 m behind the pair spectrometer to detect photons which haven't produced the pair (the total thickness of convertors is 3 radiation lengths).
At present the status of the system is the following: The vacuum chamber, the lenses and the magnets of the experimental region (which at the same time are elements of ETS) have already been produced. The coordinate system , the scintillator hodoscope and lead-scintillator sandwich are under production. All manufacturing is planned to be completed by the end of 1990. The first beam tests should begin in the middle of 1991.
The pair spectrometer is under discussion, yet.

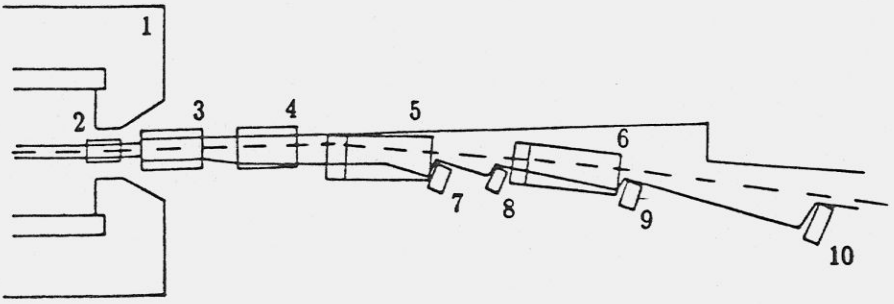

Fig. 5.2. The scheme of Electron Tagging System.
1–The detector; 2–compensating solenoid; 3,4– quadrupole lenses L_1,L_2; 5,6-bending magnets M_1,M_2; 7,8,9,10– tagging systems TS_1,TS_2,TS_3,TS_4.

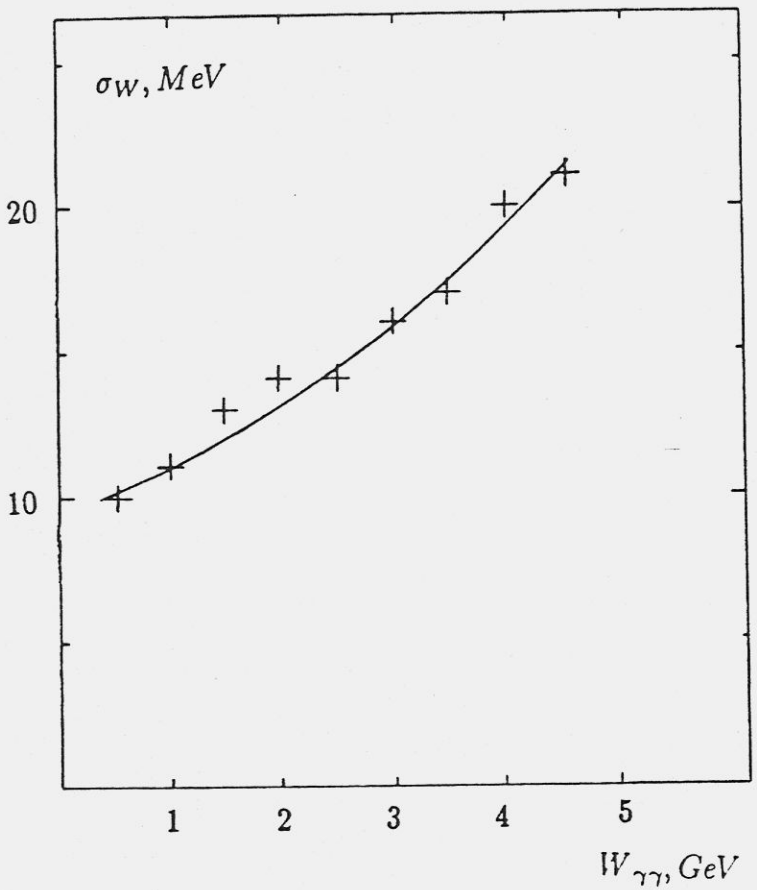

Fig. 5.3. The resolution of the reconstructed invariant mass of the two-photon system.

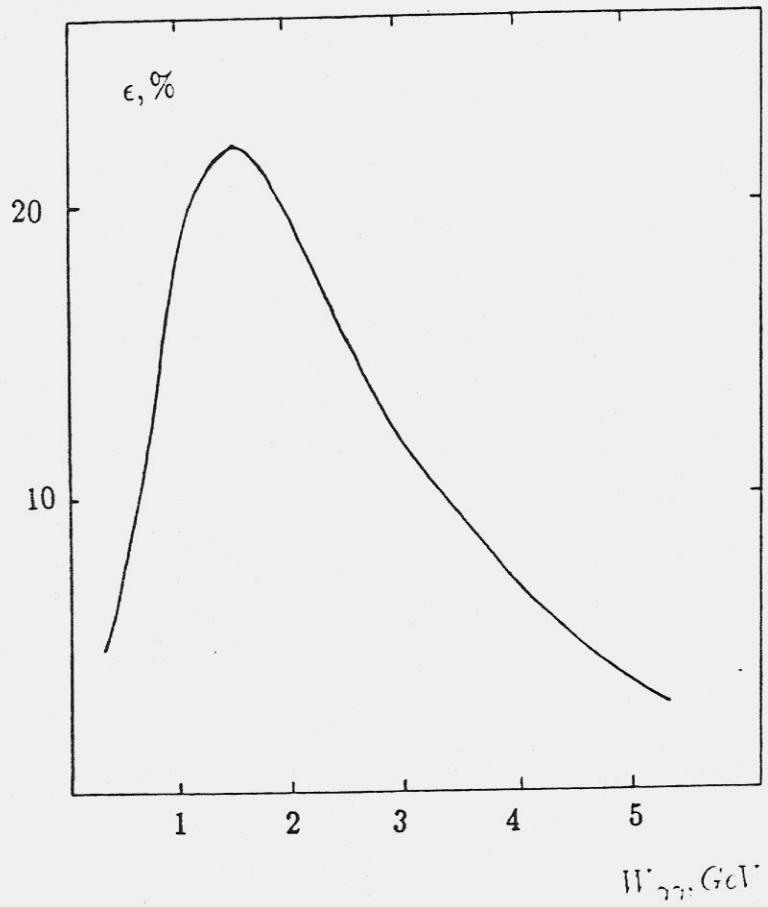

Fig. 5.4. Double t[illegible] detection efficiency.

36

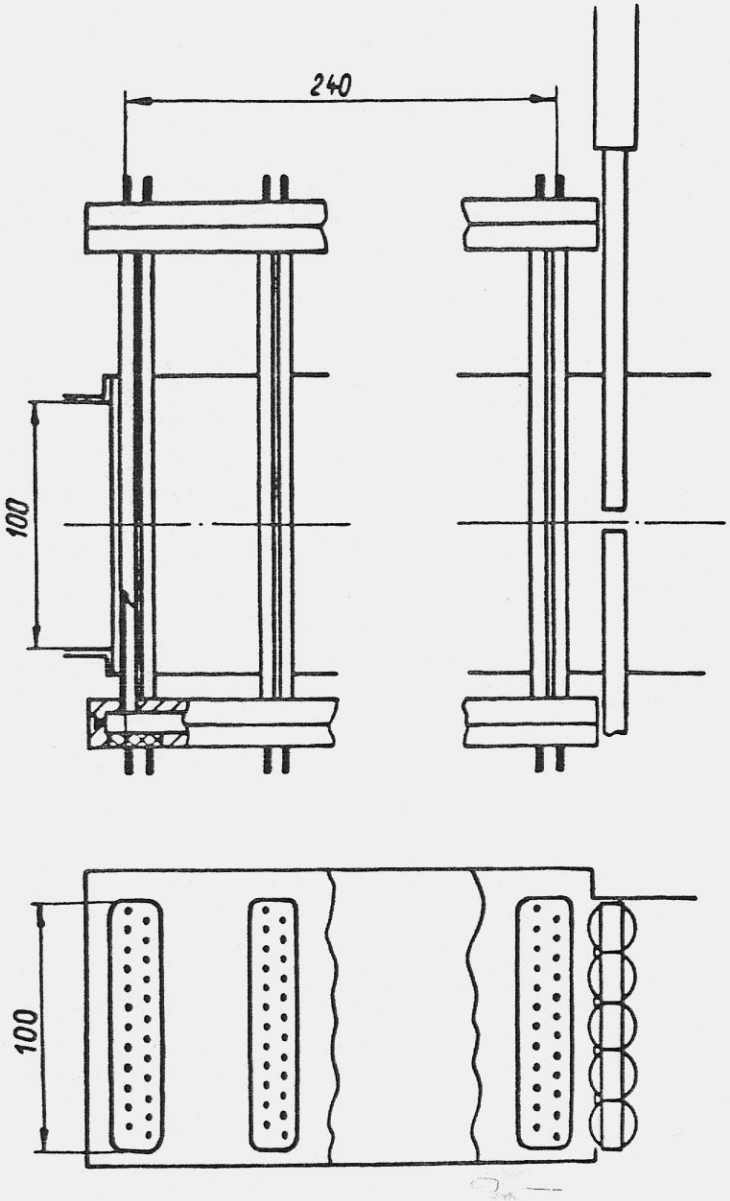

Fig. 5.5, The scheme of drift tubes hodoscope.

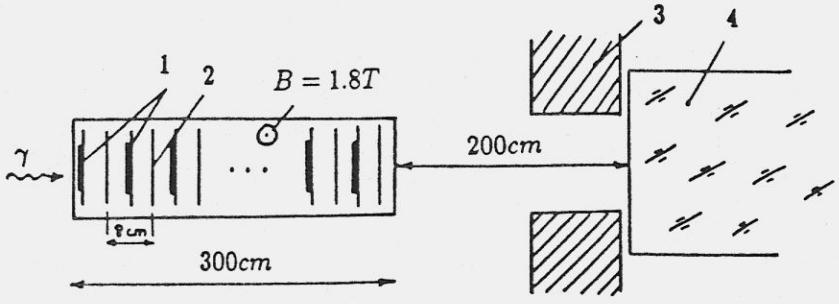

Fig.5.6 The pair spectrometer. 1- Tungsten convertors (total number 38); 2- Semiconductor detector (total number 77); 3- Diaphram; 4- The calorimeter (lead-scintillator sandwich).

6. Microvertex detector

6.1 The detector

The main part of the microvertex detector will consist of two modules with a sensitive area of about 50 × 150 mm^2. The positions of microvertex and vertex detectors are shown in Fig. 6.1. Each module will include 3 separate detectors having 1024 strips with 50 μm pitch. The detectors will be glued to a ceramic frame and their strips will be connected in series thus giving 1024 output channels fed into 16 amplifiers of CAMEX chips [1], placed on both ends of the module. The general view of the detector module is shown in Fig. 6.2.

The expected noise of one CAMEX channel optimized to our 600 ns repetition time is about 1400 electrons r.m.s. This figure is based on the published technical data of CAMEX. The tests with real chip will start in the near future.

It is planned that flat vacuum chamber will consist of Be with 1.5 mm thickness (0.4 % X_0) that is almost the same amount as 350 μm of Si detector. The minimal distance between the detector and the beam is 15 mm.

The vacuum chamber will be strong enough to keep atmospheric pressure, therefore microvertex detector may operate directly in air. It will cover about 65 % of 4π. The expected resolution should not be much worse than $\sigma = 50/\sqrt{12} = 14$ μ m but it is not quite clear yet at what angle to the vertical detector the resolution will deteriorate noticeably. The answer to this question will depend critically on the achieved noise level.

The detectors will be produced by Zeuthen group and will have DC decoupling capacitances integrated with the detector itself. The first detectors of this type have been recently produced . Up to now we worked with those detectors having ordinary DC coupled strips. The reason for decoupling is to diminish the influence of different and growing dark currents at the amplifiers operation during an experiment.

By the end of 1990 the first prototype module equipped with only few CAMEX chips, but in all other respects completely identical to the final one should be assembled at Zeuthen. It will be extensively tested at Novosibirsk in the first half of 1991.

The time schedule for the production of the final modules will be defined after the successful production of the prototype.

A series of measurements of radiation damage of the detectors were performed with 1.5 MeV electrons and synchrotron radiation in the 6 - 30 keV energy range. The results are published in 1989 Munich Conference proceedings [2]. The main conclusion is that the detectors will be able to operate after 1 Mrad dose of irradiation with such particles. The increase in the dark current will be of about 100 nA/strip (see Fig. 6.3). The main problem therefore with radiation damage is expected for CAMEX chips that can tolerate only about 20 krad if they are irradiated with power on [3]. Fortunately special shielding against synchrotron radiation may be foreseen for the electronics which is installed at the detector. The SR is expected to produce a substantial part of the radiation load in our case.

Parallel work on microstrip detectors is performed by the Italian group. Some pro-

totypes have already been produced in Modena and tested in π and μ beams in Serpukhov [4]. The detectors show very low dark current and very good resolution. Test of radiation damage has been done by exposing one detector to a 40 GeV π beam during one month for a total dose of 10^{12} particles/cm^2; the analysis of this sample is in progress.
The aim of this job is two-fold. One is the extension of the microvertex detector by 4 more modules to cover as much as possible the solid angle.Approximate position of these additional detectors is also shown in Fig. 6.1. Each module is made by three wafers 35×50 mm^2 wire-bonded together to obtain a detector of 35×150 mm^2 sensitive area. A ceramic frame will support the detector. The front-end electronics will be the same as for the above described detector, i.e. CAMEX chip. With this extension the solid angle coverage in ϕ direction may be done almost complete.
Another aim is the two-coordinate microstrip detector which is now under development in Modena. By the end of 1990 test of double facing read-out will be performed.

6.2 The Front-End electronics

In the framework of the front-end development for the microstrip vertex detector, a new JFET, compatible with the CMOS process, has been developed. This device has 1.5 μm gate length and it will replace, in the upgraded version of the 64-channel read-out chip, the present N-channel JFET , which has 4 μm gate length [5,6,7]. According to the simulation, the new JFET should feature about 2 GHz transition frequency and is expected to improve the speed of operation of the chip in a considerable way. Very preliminary tests carried out on the short channel JFET have demonstrated its very good transconductance behaviour, by virtue of which it features about 1.1 mA/V at a standing drain current of 100 μA. Besides, in spite of its short channel, the new JFET has a comparatively small 1/f-noise. The spectral noise density of the short channel JFET is plotted, as a function of frequency, in Fig. 6.4.
As shown in Fig. 6.4 at 1.6 mA the JFET features 3.3 nV/$\sqrt{Hz}$ white noise, about 20 % more than that theoretically predicted and about 6 nV/$\sqrt{Hz}$ at 10 Hz.
The front-end read-out electronics for all microstrip detectors will be supplied by the Italian group. Initially it will be based on CAMEX chips. Later on they will be changed by the new chips that are now under development.

References

1. W. Buttler et al. ICFA Instr. Bull. n.5 (1988) 32
2. A. Chilingarov et al., Nucl. Instr. and Meth. A288 (1990) 62
3. W. Buttler et al. Noise Performance and Radiation Hardeness of the CAMEX 64 talk at Munich 22 High Energy Physics Conference
4. F. Nava et al., Nucl. Inst. and Meth. A290 (1990) 418
5. H. Vogt, Nucl. Instr. and Meth. A253 (1987) 434
6. W. Buttler et al., Nucl. Instr. and Meth. A279 (1989) 204
7. W. Buttler et al., Nucl. Instr. and Meth. A288 (1990) 140

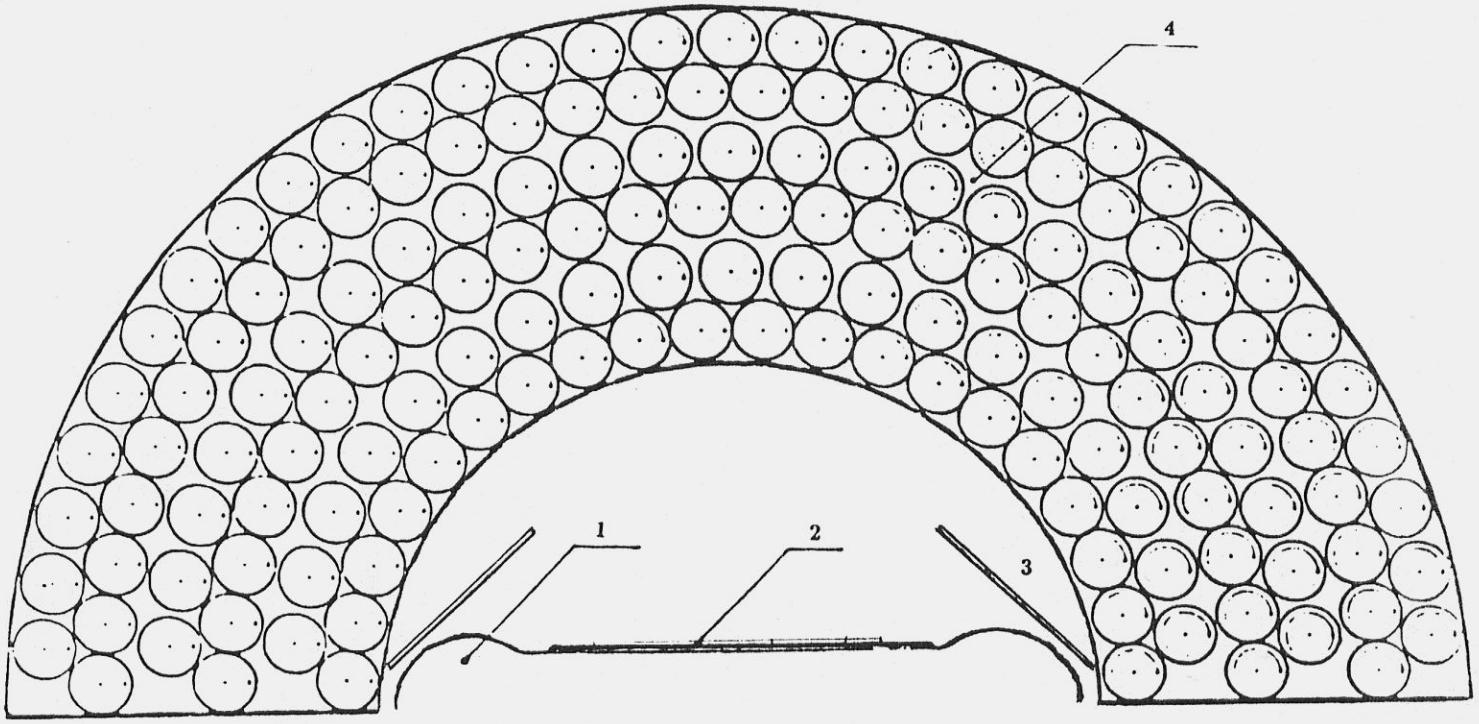

Fig. 6.1 General view of vertex and microvertex detector: (1) Beam pipe, (2) Microvertex detector (50×150 mm^2), (3) Microvertex detector (35×150 mm^2), (4) Vertex detector.

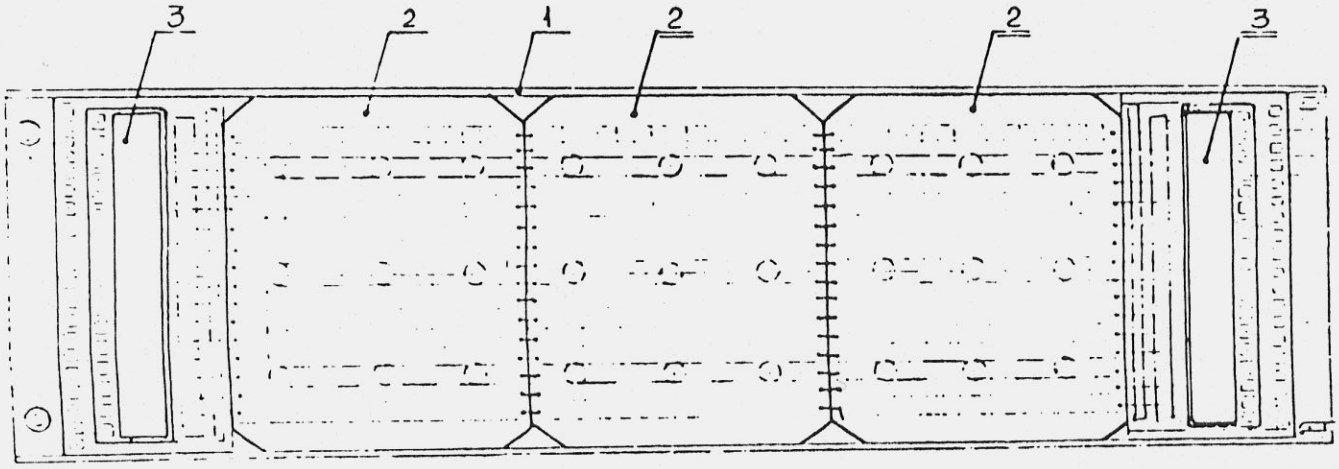

Fig. 6.2 Microvertex detector module: (1) Ceramic frame, (2) Silicon microstrip detector, (3) CAMEX chips on a special hybrid support.

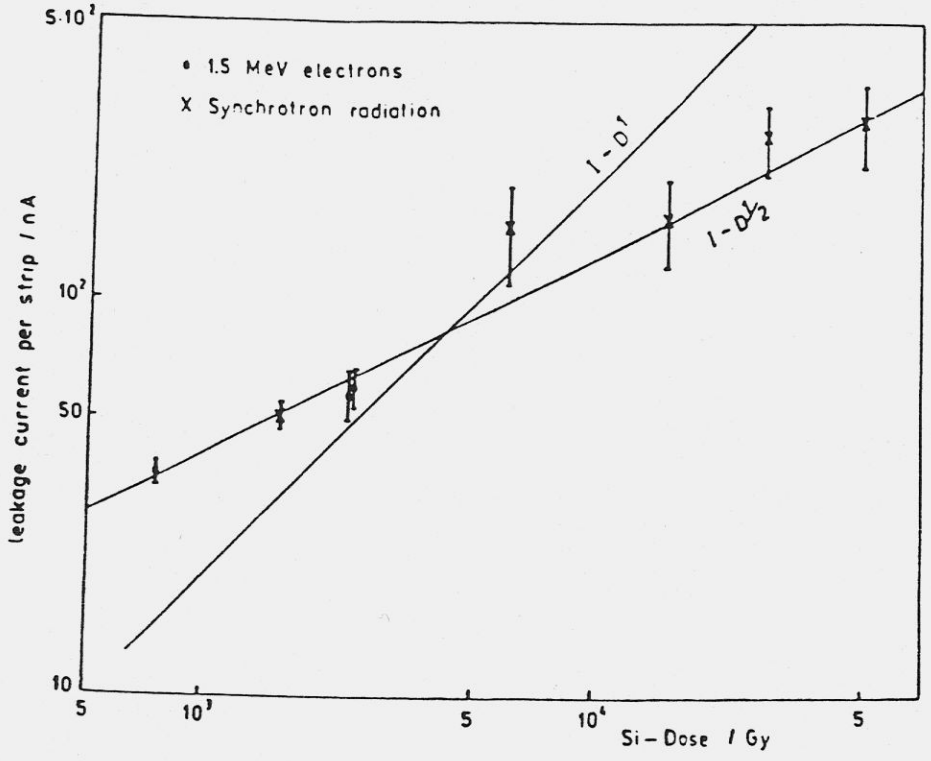

Fig. 6.3 Dark current via irradiation dose

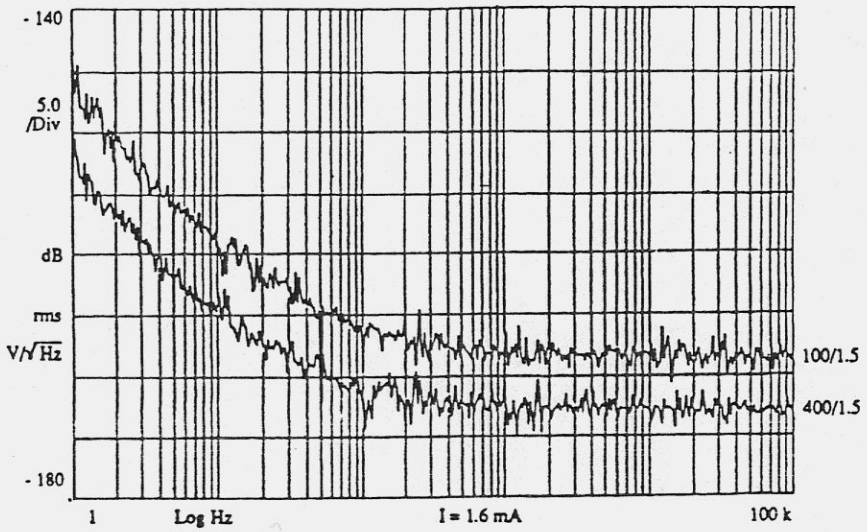

Fig. 6.4 Spectral power density of the series noise for the N-channel JFET with 1.5 μm gate length.

7. Vertex detector

The vertex chamber (VC) is a straw-type drift chamber made of mylar tubes with 20 μm thick walls. Such cells are mechanically isolated and the electric field in them is completely symmetric. Due to these features straw chambers are now rather popular [5]. Usually the access to the vertex chamber is rather difficult so the chamber has to be reliable enough. Tubes suit that requirement very well.

The radial dimensions of the vertex chamber are limited to 120 and 246 mm diameters. The sensitive length is 670 mm. The chamber consists of two independent halves. The positions of the tubes are shown in Fig. 7.1. There are 312 tubes in 6 cylindrical layers which form 3 double layers. Those in an odd layer are separated by as small intervals as possible. The angular intervals between the tube centers in the next layer are the same and tubes are shifted by half a period. Thus there are no holes in a double layer. The inefficiency of a single odd layer results mainly from the inability to detect two particles in one tube. In this case only the particle closest to the wire will be detected. But if the particles come from the beam, the second one becomes the closest in the next layer and hence it is detected too. The inefficiency of the first layer is 13 % and for the first double layer it is 3 % (without the edge holes).

The geometry of the vertex chamber provides the accuracy of the impact parameter reconstruction at the beam region:

$$\sigma_d = 2.2\sigma_0$$

where σ_0 is the rϕ resolution in a single tube. The contribution of multiple scattering is 40 μm/P [GeV] and results mainly from the material of the vacuum chamber and the inner wall of the vertex chamber. The longitudinal coordinate is not measured by the vertex chamber.

The tubes are produced in the laboratory by means of ultrasonic welding. The tubes produced by this method keep the cylindrical shape very well, especially after being glued to the end plugs. An unloaded tube with fixed plugs has a gravitational sag of about 0.1 mm. An additional tension of 200 g will be applied to each tube after installation in the end plates.

The attractive feature of the module is that it can keep a pressure up to 3 atm. The tubes may operate directly in air, so that there is no need for a leakproof gas vessel around the VC.

The slightly overpressurized tube becomes rigid and stable against twisting along its axis. This is essential, because the mylar wall shows very weak resistance to any sort of transverse tension, and special attention must be paid to keep the correct cylindrical form of the cell.

The aluminized mylar we use has been irradiated by 1.5 MeV electrons to a dose of 1 Mrad, which is 3 orders of magnitude higher than one could expect in an experiment. No visible damage or change of mechanical properties has been observed.

The electronics channel is shown in Fig. 7.2. It consists of a preamplifier, a shaping amplifier and a digitizer. Preamplifiers are situated near the wires on both flanges of the vertex chamber. They have a rise time of 5 ns and a response of 0.3 V/pC. The output pulse is transferred via 5 m long twisted-pair cables to the shaper which is installed near the detector. The effective threshold of the shaper together with the preamplifier is 0.01 pC. It is approximately two times lower than the average pulse produced by a single electron. The total slewing from twice the threshold up to very high values does not exceed 4 ns. It mainly contributes to the spatial resolution near the wire.

The logic signals from shapers are transferred to digitizers through a 50 m line. The digitizers are direct counting TDCs with 2 ns resolution [3].

We plan to use cool gas mixtures in the vertex chamber to minimize diffusion. This choice has some other advantages. In a major fraction of a tube the electric field and the drift velocity are low. This results in a low contribution of the timing accuracy to the spatial resolution. For a cool gas the drift time is almost the same with and without magnetic field.

On the other hand, the long drift time makes it difficult to use the vertex chamber in the trigger system. The main problem of operation with cool gases, of course, is the strong dependence of the drift velocity on temperature and pressure, and one has to control them very carefully.

To study different gases, electronics and reconstruction procedures, we have built a small pressurized chamber consisting of 14 tubes which were positioned in 6 layers, just as the VD geometry. The mylar thickness and length were different, 50 μm and 200 mm respectively. The chamber was tested in a 1 GeV positron beam at the storage ring VEPP-3.

The temperature and the pressure were measured during the prototype tests, and their total variations did not exceed 0.3 %.

In Fig. 7.3 the resolutions versus radii for different gases are shown. Among the three mixtures shown, that with Ar:CO_2 (50:50) has the poorest resolution. In the main part of the tube it is about 50 μm. This result is in reasonable agreement with our Monte Carlo simulations, taking into account ionization statistics, diffusion and electronics response. Near the wire ,however, σ_r is somewhat larger than that predicted by the simulations.

The results with CO_2 + i C_4 H_{10} (10 %) very much resemble those of Commichau et al. [4]. In the main part of the tube the resolution is 22 μm at 2 atm. The difference of σ_r for 1 atm and 2 atm was found to be in good agreement with the expected difference due to diffusion. Again, the resolution near the wire is rather poor. We also made a test run with DME gas at 1 atm. It is very cool gas with very low drift velocity. The result is similar to that for CO_2 + i C_4 H_{10} at 2 atm. The resolution is better at smaller radii. Note the very long drift times in this case (see Fig. 7.4).

A t[illegible] mylar tube vertex chamber is presently designed for the KEDR detector. The prototype tests show its ability to reach a resolution of 20-30 μm in the main part of a tube. Cool gases like CO_2 +10 % iso-C_4 H_{10} or DME and pressures

up to 2 atm are necessary for this purpose. The detector, now under production , is supposed to be finished by the end of 1990. The assembly in the laboratory and the tests are planned for the first half of 1991. In autumn 1991 the vertex detector may be installed at VEPP-4M.

References

1. V. V. Anashin et al., Proc. Int. Symp. on Position Detectors in High Energy Physics, Dubna (1988) p.58
2. V. M. Aulchenko et al., Preprint INP 84-166, Novosibirsk
3. V. M. Aulchenko et al., Preprint INP 88-29, Novosibirsk
   V. M. Aulchenko et al., Preprint INP 88-22, Novosibirsk
4. V. Commichau et al., Nucl. Instr. and Meth. A239 (85) 487
5. J. Adler et al., SLAC-PUB-4371 (1987)
   W.W. Ash et al., Nucl. Instr. and Meth. A261 (87) 399
   P. Baringer et al., Nucl. Instr. and Meth. A254 (87) 542

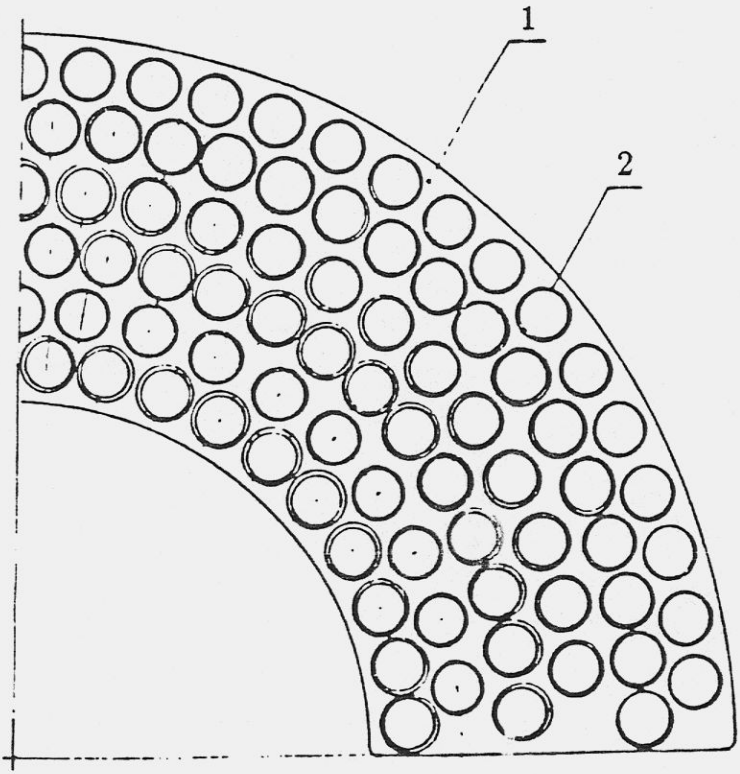

Fig. 7.1 The position of the tubes in the VC: (1) tubes, (2) end flange

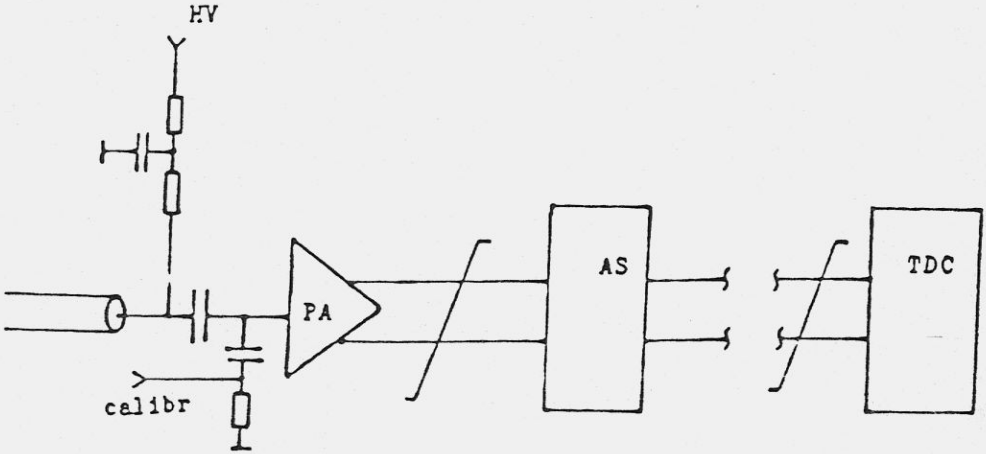

Fig. 7.2 Electronic channel: PA - preamplifiers, AS - amplifier-shaper

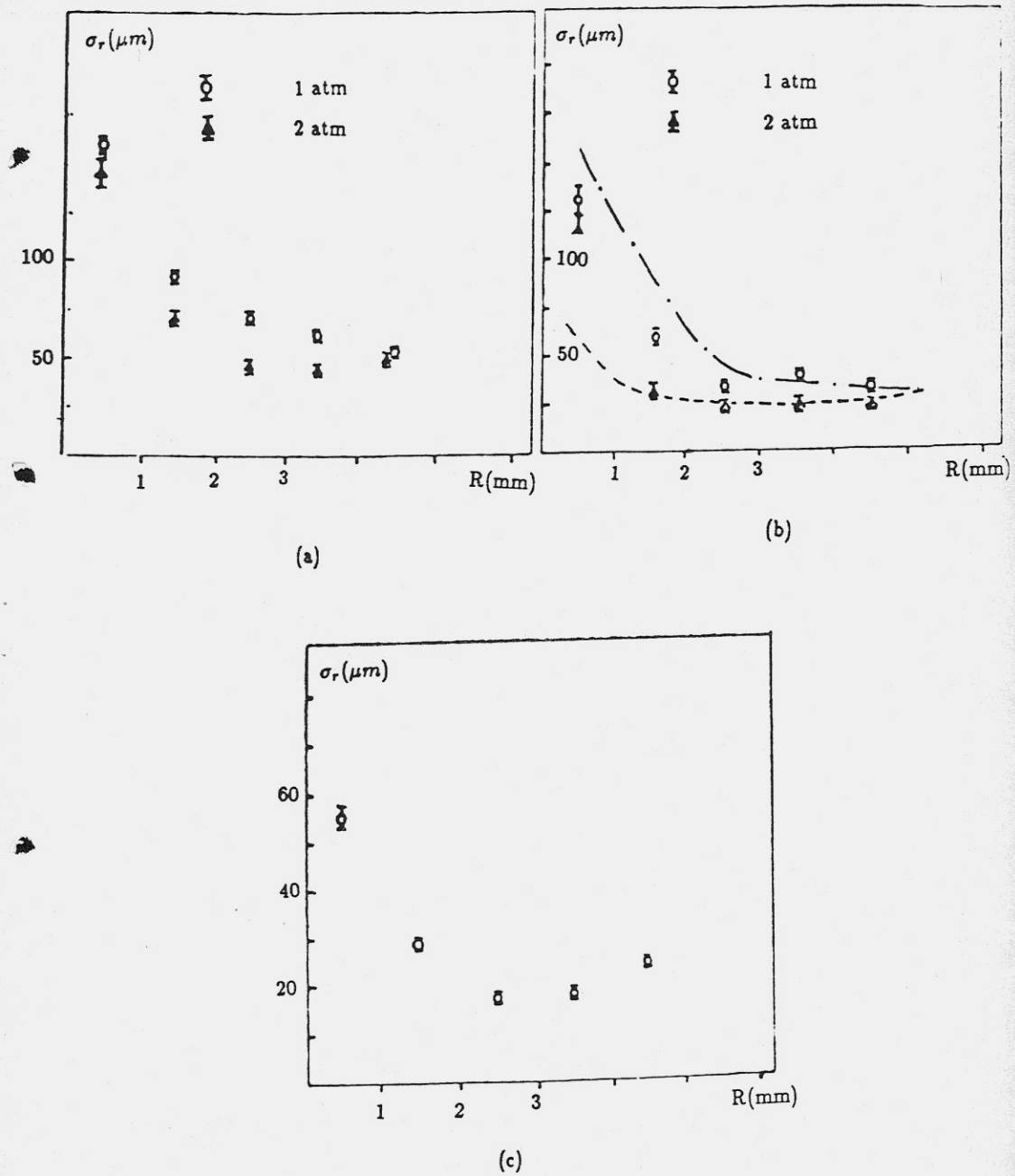

Fig.7.3. (a) The resolution σ_r as a function of R for Ar + 50 % CO_2 at 1 and 2 atm. (b) as a function of R for a CO_2 + 10 % C_4 H_{10} mixture. The lines are the result of Commichau et al.[4] for CO_2 + 15 % C_4 H_{10} Dash-dotted line: at 1 atm; dashed line: at 2 atm. (c) The resolution for DME at 1 atm.

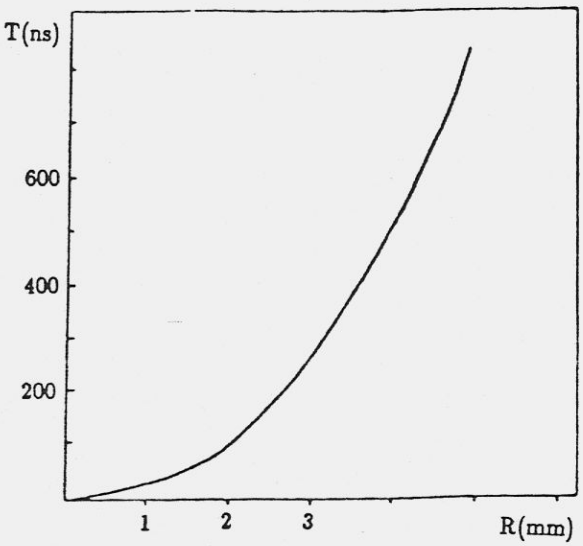

Fig. 7.4 The R(T) dependence for DME

8. Drift chamber

8.1 Description

The drift chamber (DC) occupies the volume defined by two concentric cylindrical walls with a length of 1100 mm, and two end plates with an outer diameter of 1070 mm. An inner pipe of 250 mm diameter separates it from the vertex detector. The inner pipe, the outer pipe and the endplates form the gas sealed volume where a large set of wires are located (Fig.8.1). The chamber wires are arranged in drift cells and held under tension by the two endplates.

The drift cells are collected in 7 superlayers, four of which (first, third, fifth, seventh) have axial wires while the other three have wires inclined with respect to the cylinder axis. Stereo layers serve to the polar angle measurement.

The preamplifiers are located at one endplate. The signals from sense wires are amplified and transmitted to the data acquisition electronics by twisted pair cable 30 m long. The arrival time and amplitude of the pulse are measured. The threshold of time discriminator is $3 \cdot 10^{-15}$ C. The time is measured by direct counting method with a 6 ns step. Dynamic range of the amplitude measurements is 12 bits. Ionization losses are supposed to be measured in DC for particle identification. The high voltage supply is placed on the other endplate. The DC parameters are summarized in Table 8.1.

Tab. 8.1: Drift Chamber Parameters

Inner radius	$125mm$
Outer radius	$535mm$
Length	$1100mm$
Wire length	$970mm$
Number of superlayers:	
Axial	4
Stereo	3
Total	7
Stereo angle	$100mrad$
Number of layers	42
Number of cell	252
Number of wires:	
Sense	1512
Field and focus	11772
Shield	2748
Total	16032

8.2 DC design

DC consists of two endplates supported by inner and outer cylindrical walls. The wire tension is 250 g for field and focus wires with a 150 μm diameter made of Ti and 100 g for gold plated tungsten anode wire with a 28 μm diameter. The total wire tension applied to the endplates is equal to 3.4 tons.
The outer cylindrical wall is made of G10 type plastic of 5 mm thickness, the inner wall of 1.5 mm thick carbon fiber reinforced. The endplates are made of G10 plastic 20 mm thick. The amount of material is listed in Table 8.2.

Tab. 8.2: Amount of material

	Thickness	% X_0
Inner wall:		
Carbon fiber reinforced	1.5*mm*	0.54
G10	0.1*mm*	0.05
Cu foil	0.2*mm*	0.13
Total		0.72
Wires (average)		0.25
Gas (DME)		0.17
Outer wall (G10)	5.0*mm*	2.5
End plates (G10)	20.0*mm*	10.0

The holes for fixing the wires are drilled precisely in the endplates. The position accuracy of the holes is 20 μm. Metal pins, 1 mm diameter, are inserted into these holes. Wires are crimped in the pins. These crimp pins are made of stainless steel tube ; the inner diameter of the pins is 60 μm for anode wires and 200 μm for field wires. DC components are shown in Fig.8.2.
The endplates are glued with inner and outer cylindrical walls making the construction rigid. Before wiring the endplates, they are deformed with force imitating that of the stretched wires. Maximum endplates deformation is 1 mm. During the wires stringing the external force decreases.

8.3 DC cell design

The choice of cell design is defined by the requirement to have the best momentum resolution. The space available for DC in the detector is rather limited (outer radius 535 mm); for a good momentum resolution, therefore, it is necessary to have a cell with the best attainable spatial resolution. The cell used in our detector is identical to that of SLD [1]. The cell (Fig.8.3) contains 8 anode wires : 6 of them are sense with a

28 μm diameter and are made of gold-plated tungsten and the outer two are dummy; they are used for field formation and have a diameter of 150 μm. Their signals are not read-out. The distance between the anode wires is 4.5 mm. To the left and to the right of the anode wires there are 9 focus wires. The distance between the rows of focus wires is 7 mm. The field wires shape the region from where the ionization is collected. The field wires are placed with a 4.5 mm step. Focus and field wires have 150 μm diameter (gold plated Ti). The radial dimension of a cell is 36 mm. Maximum drift distance is 30 mm. The anode, focus and edge field planes are inclined 3^0 relative to the radial direction. This is done to compensate the shift of the electrons drifting in the crossed electric and magnetic fields. The tuning of the gas amplification is done by the change of the voltage at the focus wires. The distributed potential at the field wires produces the uniform electric field in the drift cell. To restrict the influence of the neighboring superlayers additional shielding wires are used between the superlayers and they are connected to some fixed potential. The potential value is determined by the drift field homogeneity. This shield allows to have a distance of 21 mm between the superlayers without significant deterioration of the space resolution. On both the inner surfaces of the cylindrical walls there are axial metal strips with an optimal potential. This allows to have a distance of 5 mm between the extreme superlayers and the walls without distortion of the field in the cell. The geometrical parameters of DC are listed in the Table 8.3.

Tab. 8.3: Parameters of the cell

Number of sense wires	6
Wire diameter:	
Sense (W/Au)	28 μm
Field and focus (Ti/Au)	150 μm
Shield (Ti/Au)	70 μm
Wire tension :	
Sense and Shield	100 g
Field and focus	250 g
Surface field at wires :	
Sense	360 kV/cm
Focus	8 kV/cm
Field	15–47 kV/cm
Maximum field wire voltage	8 kV
Gas	DME (C_2H_6O) at 1atm
Drift field	2.0 kV/cm
Drift velocity	6.0 $\mu m/ns$

For the uniformity of the drift field near the endplates there are metal strips on

inner surface of the endplates, inside the cell (Fig.8.3). These strips are electrically connected with appropriate field wires. The use of these strips decrease the distance from endplates, where error in distance measurement due to electric field distortion is more than 100 μm from 9 cm (no strips) to 1.5 cm (8 strips in cell).

8.4 The spatial resolution

The chamber operate with "cool" gas - dimetylether (DME) at atmospheric pressure [2]. The diffusion for DME is minimum and have a value D = 60 $\mu m/\sqrt{cm}$ cm. The drift velocity depends on the electric field and is equal to 6 μm/ns at E = 2 kV/cm. The measurements of the spatial resolution on one-cell prototype of the DC has been done with DME. Data were taken with cosmic particles. Figure 8.4 shows the measured drift resolution as a function of drift distance at two values of the high voltage on focus wires. The average resolution as a function of the high voltage on focus wires is presented in Fig.8.5. The average resolution with high voltage on focus wires equal to 2.9 kV is 60 μm and 40 μm with 3.1 kV.
dE/dx measurements in DC determine the high voltage value on focus wires. This is caused by saturation effects in the gas gain. The operating high voltage value is 2.9 kV and the gas gain is $2 \cdot 10^5$. We estimate that the rms dE/dx resolution will be 10 %. This make available the π/K separation up to momentum 600 MeV/c and K/p up to 1200 MeV/c at 2 sigma level.
The use of "cool" gas puts serious requirements to the stability of the working conditions of the system. An error of 10 μm for a 1 cm drift distance is induced when the parameters change inside the following limits:

temperature $dT = 0.3\ ^{o}C$
pressure $dP/P = 10^{-3}$
electric field in the cell $dE/E = 10^{-3}$

We assume to calibrate the drift velocity during the experiment. We use the same method proposed for the drift chamber of the SLD detector [3].
The drift velocity calibration system is shown in Fig.8.6. Photons from pulsed nitrogen laser with 337 nm wavelength are transmitted through optical fibers to the photo-electron sources situated inside the active volume of the DC. The photo-electrons from the tip of the source drift to anode wire. One of the optical fiber is connected with photodiode to produce the trigger signal. By measuring the drift time of the photo-electrons we find the drift velocity. In Fig.8.7 the active tip of the photo-electron source is shown. The drift velocity calibration will be done in 24 cells (12 cells on each endplate). Measured value of expend laser pulse energy to one photo-electron production is 0.6 μJ. The laser model LGI-505 with an energy of 120 μJ per pulse and repetition frequency of 1 kHz produces on the average 3 photo-electrons on one source per pulse with a 50 % energy loss in the optical fiber.
The time spectrum of anode wire signals from laser is shown in Fig.8.8. The time rms resolution is 60 ns. Consequently, for drift time measurement with an accuracy of 2 ns we need to detect 1000 laser pulses. Thus a developed system let us calibrate the

drift velocity during the experiment.

8.5 DC aging studies.

An important features of the DC is the ability to operate at high rates of the particle flux during a long time period. The aging tests of the DC cell have been done with DME gas.

Schematic layout of the setup is shown in Fig.8.9. Gas flow pass through the volume with a tested material and then enters into the chamber. The influence on aging gas impurities from different materials was measured in the drift tube. The last test was done with the cell placed in the box made of the same material as DC.

The aging effect was characterized by a gain drop dependent on the total charge accumulated on one unit wire length . A collimated source of Sr90 was used as radiation expose. Irradiated length of wire was about 2 cm. For amplitude measurements we use the collimated source Fe55 at the aged spot.

Anode current under radiation was equal 1 mA/cm. The gas flow rate was adjusted that to change the gas in chamber per hour and was equal 1-50 cm^3 /min. The results of measurements are shown in Table 8.4.

Tab. 8.4: Tests for DME

	Tested Material	Charge Dose (C/cm)	R ($\%cm/C$)
Tube	DME	2.8	1.7
	PVC tube	0.1	97.0
	Teflon tube	1.1	7.2
	G10	0.95	11.2
	Epoxy	0.95	7.1
	Gas seal paste	0.8	7.7
	Pump oil	1.2	0.4
	Alpha-Naphtylamine	0.6	2.0
Cell	DC's materials	0.6	45.0

The relative gain drop R is determined as R=-dA/A/Q, where dA/A is the relative amplitude decrease (%) and Q is the total charge accumulated on 1 cm of wire length. This results show that pure DME have small aging effect (R=1.7 %·cm/C). For the DC cell R is equal to 45 %· cm/C. This value leads to a 2 % amplitude signal decrease per year with a gas amplification of 10^5 and with a flux of charged particles equal to

1 kHz/cm^2 . Such conditions are acceptable for DC.

8.6 DC characteristics

The momentum resolution of the drift chamber may be expressed in the following form :

$$(\sigma_P/P)^2 = B^2 + A^2 \cdot P^2$$

where P is the momentum in GeV/c, A is determined by the measuring accuracy of the chamber and B by the multiple scattering in the chamber medium.

If the momentum is determined only by DC (σ chamber = 100 μm, measuring distance L=370 mm; number of measurements N=42), the A and B coefficients are: A=$5 \cdot 10^{-3}$, B=$3 \cdot 10^{-3}$.

Estimating the coefficient B, we have taken into account scattering by gas and wires. We assume that if a particle hits a wire, the trajectory is fitted with a kink in the intersection point. Such a fitting method results in the smallest value of that term in B which is due to the scattering by the wires. Compared to the case when the wire material is uniformly distributed over the volume, this gives a decrease by a factor of 1.6.

The use of the vertex detector VD improves the measuring accuracy with the increase of the measuring distance and the number of measurements (L=460 mm, N=48). The A value becomes $3 \cdot 10^{-3}$. The multiple scattering contribution does not change.

The accuracy of the polar angle measurements depends on the value of the angle and is equal to

$$\sigma_\theta = 2 \cdot 10^{-3} \cdot sin^2\theta \qquad for \qquad \theta > 45^0$$

8.7 Status and plans.

The tools for wire straining and crimping have already been prepared. The DC prototype 1 m long with 500 wires has been produced .

The technology of the crimp pin production have been developed. Up to now five thousands of crimp pins have been manufactured.

All elements of DC have been manufactured (both endplates with the holes, the inner and outer cylindrical walls). The time schedule of the DC production is shown in Table 8.5

Table 8.5

DC time schedule	
Chamber gluing	June 1990
Chamber wiring	Febr. 1991
HV and wire tension testing	April 1991
Gas sealing, preampl. and HV mounting	June 1991
Ready for VEPP-4M installation	August 1991

References.

1. SLD Design Report, SLAC-Report-273, May 1984
2. F. Villa , Nucl. Instrum. Methods, 217 (1983) 273
3. R. Yamamoto, Report No. DOE/ER/03069-490A SLD Memo 25.01.89.

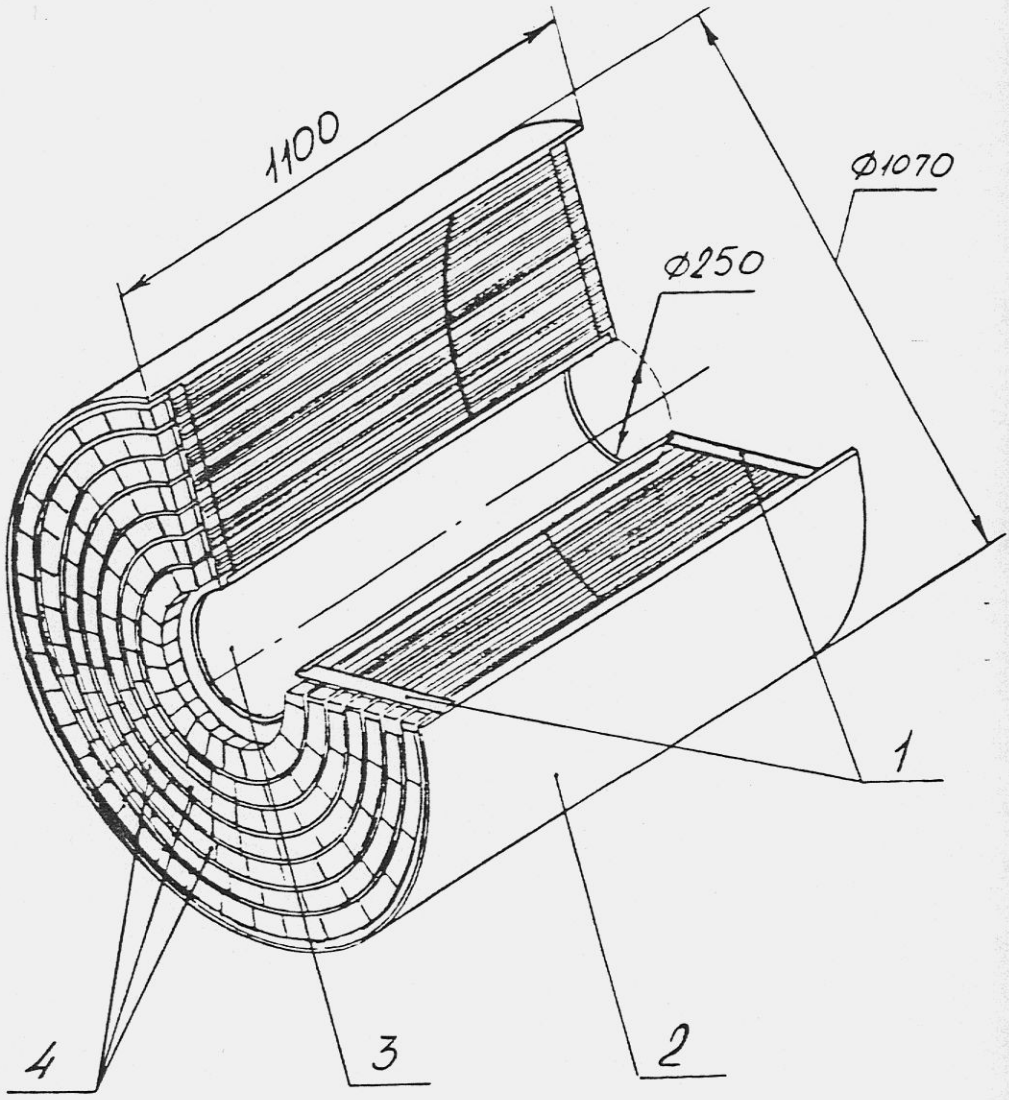

Fig. 8.1 DC design. General view. 1 - endplates; 2 - outer wall; 3 - inner wall; 4 - drift cells.

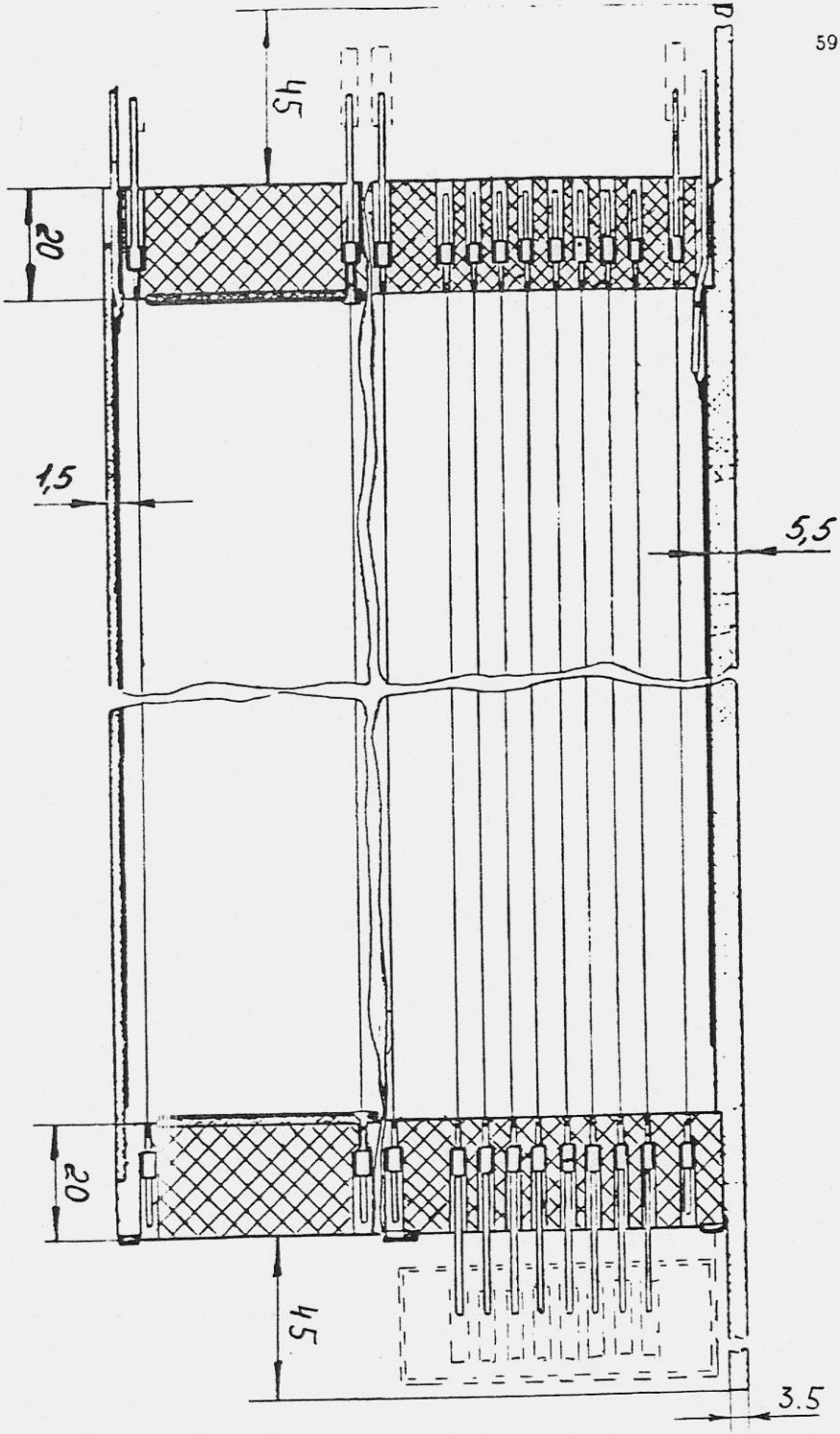

Fig. 8.2 Elements of DC construction.

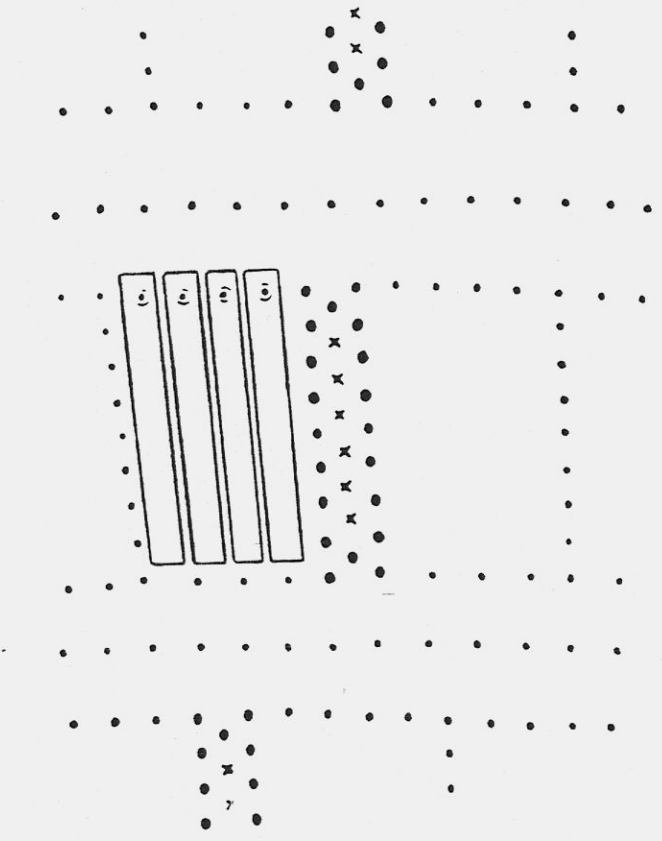

Fig. 8.3 DC cell. x - anode wires; ● - focus wires; · - field and shield wires.

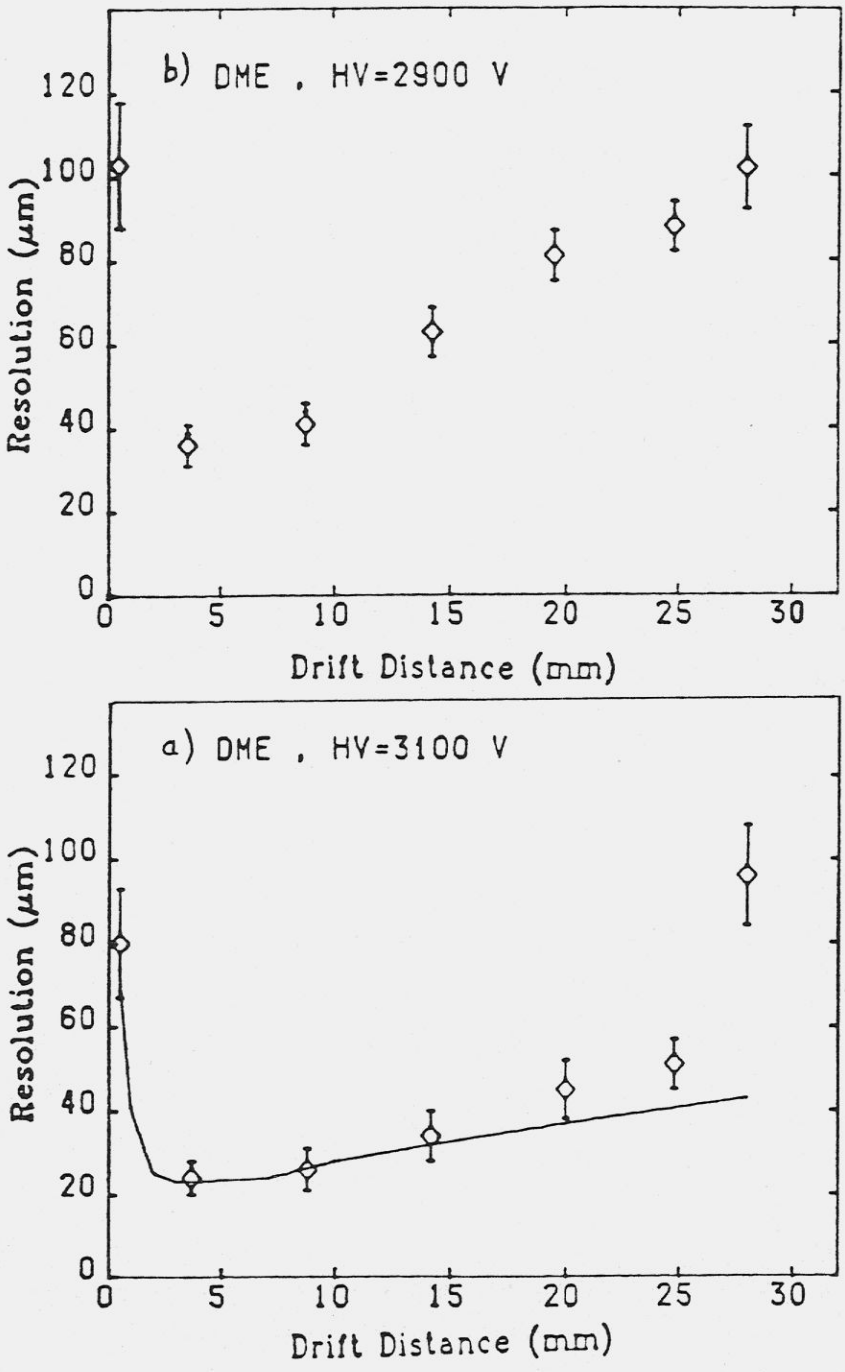

Fig. 8.4 Drift resolution versus drift distance with DME. a - Ufoc = 2900 V; b) Ufoc = 3100 V.

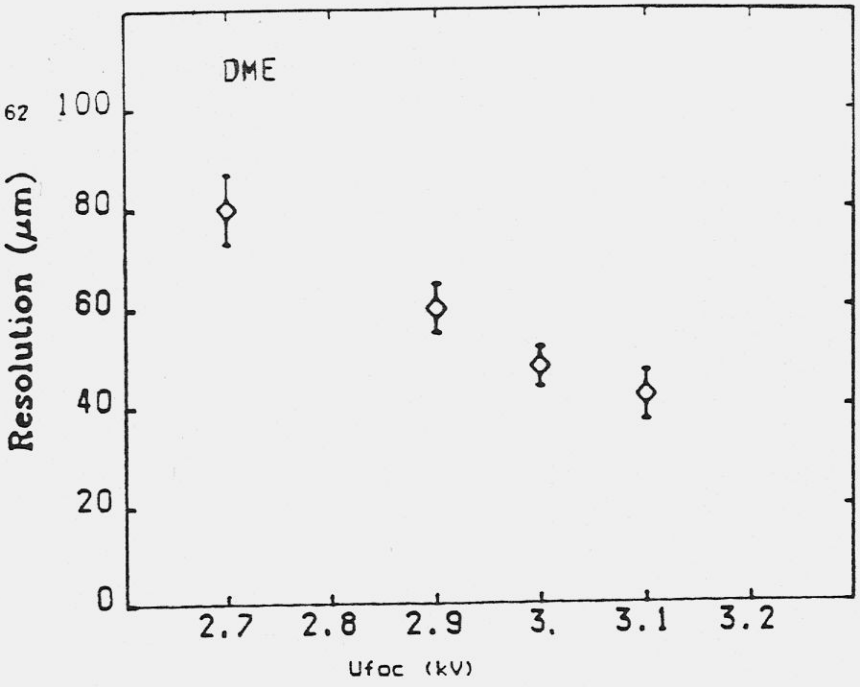

Fig. 8.5 Average drift cell resolution versus high voltage at focus wires with DME.

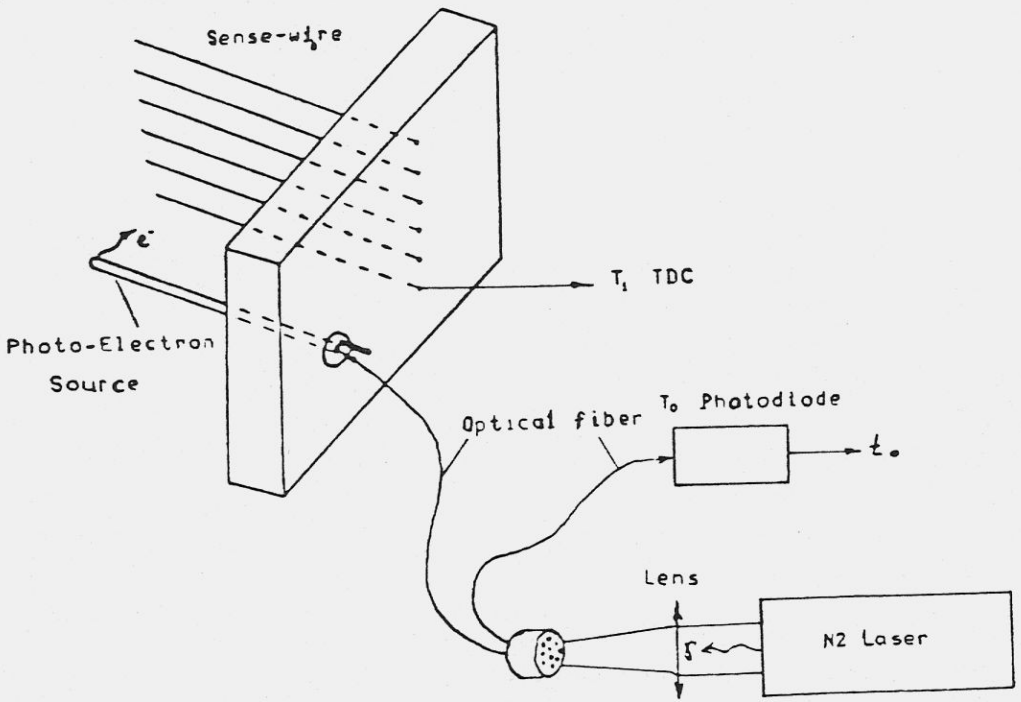

Fig. 8.6 Drift velocity calibration system layout.

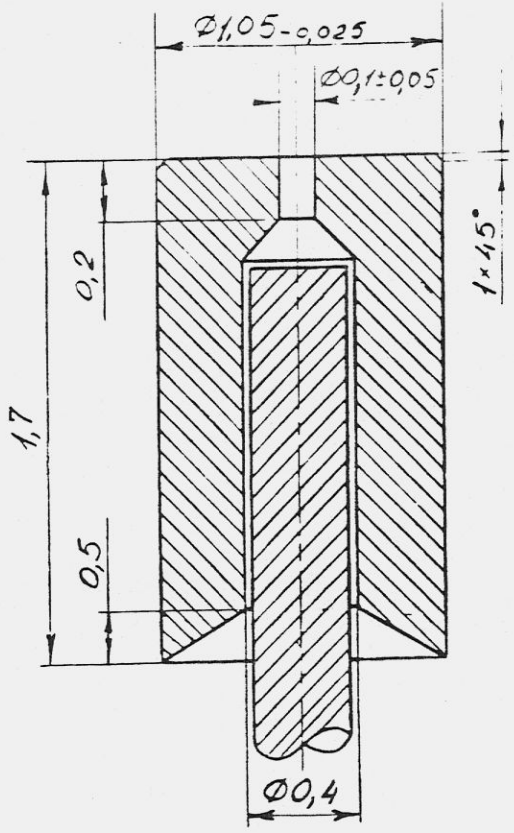

Fig. 8.7 Active tip of the photo-electrons source.

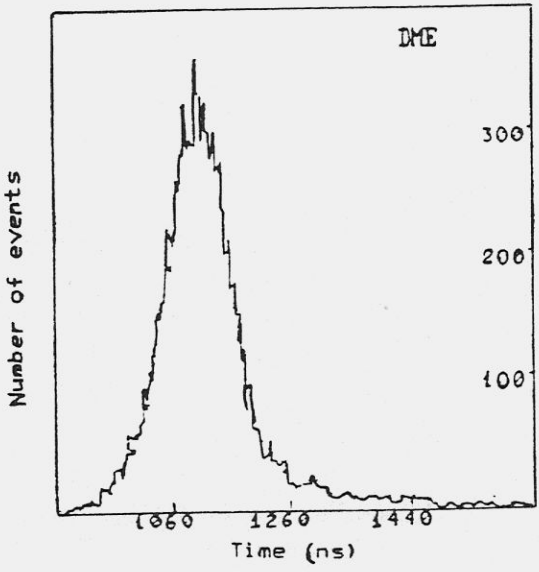

Fig. 8.8 Time spectrum of anode wire signals from laser.

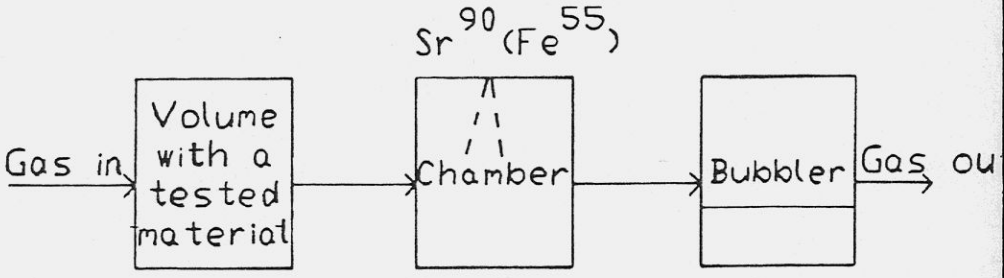

Fig. 8.9 Schematic of the aging test setup.

9. Particle identification

9.1 Time of flight hodoscope

A hodoscope of scintillation counters for time of flight (TOF)measurements has been designed in order to make a fast trigger, to help in fast tracks finding, to identify the charged particles using TOF and ionization losses. Moreover this hodoscope will be useful for γ-rays pattern which converted before the calorimeter. The barrel system (see Fig. 9.1) consists of 32 scintillation counters covering the angular region $30^0 < \theta < 141^0$ which corresponds to a solid angle of $0.77 \cdot 4\pi$ sr, the average distance from the beam is 71 cm. Each counter, approximately $14 \times 180 \times 1$ cm in size, is viewed through bent lightguides by two photomultipliers placed inside the iron yoke. The screens were designed to suppress the tension of the magnetic field to the value of not more than 0.1 mT within the PM position. We plan to use PM of R1828 type in the barrel TOF.

Endcaps will be made of one layer of scintillation counters, 2 cm thick, with a trapezoidal shape, viewed by one PM XP2262. In each endcap 32 counters are needed.

PILOT-F is supposed to be applied as a scintillator in TOF system.

Both measurements, made with the prototype and the computer simulation, give a time resolution better than 300 ps. Such a resolution allows the identification of π and K up to 620 MeV/c momentum (at 2 σ).

We have no components for TOF in the Institute ,yet. Provided that the PM tubes and the scintillator will be received this summer, the endcap system could be done at the beginning of 1991 and the barrel one will be completed within the end of 1991.

9.2 Aerogel Cherenkov counters

The known specific feature of B-mesons decays is the appearance of K-mesons in almost all channels. The momentum spectrum of kaons continue up to half of B-mesons masses. For full reconstruction of B decays it's necessary to separate π/K in this momentum range. This is the main aim of particle identification system in the detector, which consists of threshold Cherenkov counters together with other devices. Cherenkov counters are placed behind the drift chamber (Fig. 4.1). We propose to use a silica aerogel with refraction index n=1.035 (threshold of $\gamma = 3.9$) as radiator in counters . It allows to separate π and K in range of 0.65 to 1.9 GeV/c. π/K discrimination outside this region will be performed by dE/dx measurement in the drift chamber and in the liquid krypton calorimeter (Fig. 9.1) and by time of flight measurement in scintillation counters.

Design of Cherenkov counters and their layout in the barrel part of the detector is shown schematically in Fig. 9.2. The area of one counter is expected to be about 400 cm^2, the aerogel thickness is 10 cm. The 5 cm empty space behind aerogel is needed to improve light collection and for phototubes installation. The counter inner surface is coated with highly reflecting paint. Two phototubes are used in each counter. The phototubes looking into one counter are placed in special pockets, which are made in the neighbouring counters. Such a design reduces the number of events with one

particle crossing the aerogel and the phototube simultaneously. The total number of Cherenkov counters in the detector is expected to be 180 , the necessary number of phototubes is 360 and the total volume of aerogel is 700 liters.

In the Cherenkov counters we are planning to use 5 cm diameter and 7 cm length Hamamatsu phototubes R 2490-01. This choice has been made after testing 5 samples of such tubes. We have measured the gain of phototubes with a magnetic field up to 2 T. The gain of 5 samples in a 2 T magnetic field environment was in the range of 6 to 12 thousands and the dark current was 1-10 nA. Such a gain of tubes is enough for the detection of the signals from one photoelectron if low noise amplifiers are used. This possibility was experimentally tested. The phototubes were placed in a 2 T magnetic field and they detected the weak flash from light diode. During the measurements we used an amplifiers with 700 electrons effective noise charge. Flash detection efficiency versus detection threshold is shown in Fig. 9.3. Average numbers of photoelectrons from light flashes are shown near the curves. The value of accidental coincidences which appeared due to phototube's and amplifier's noise is also shown. Time resolution of coincidence scheme was equal to 3 μs amplifier pulse duration. It's possible to decrease the value of accidental coincidence by the optimization of the amplifier pulse duration.

We expect that aerogel for Cherenkov counters will be produced in the Institute of Catalysis (Novosibirsk).A group from this institute has organized the production of aerogel with the following parameters: size of pieces $6\times6\times2.5$ cm^3, range of possible refraction index n=1.015-1.040, light scattering length L_s = 2.6-3.0 cm at λ =436 nm and the average value of light absorption length L_a is about 1 m in the range of λ = 300-600 nm. These optical properties are comparable with those of the aerogel produced in other places [1]. The same group is working on the organization of the production of aerogel with size about $20\times20\times2.5$ cm^3. The refraction index and the light scattering length of aerogel were obtained by straightforward measurements. The light absorption length was estimated indirectly by comparison of Monte Carlo simulation with measured value of Cherenkov light collected on phototubes in the counter prototype.

We have produced a prototype of Cherenkov counter and we have measured its parameters. The prototype design was almost the same as shown in Fig. 9.2. The prototype area was 18×12 cm^2 and the aerogel thickness was 10 cm. In prototype we used aerogel with refraction index n=1.034-1.036, which have been produced in the Institute of Catalysis (Novosibirsk). Two phototubes of the type R 2490-01 were used for detection of light. The measurements have been made without high magnetic field environment but the supply voltage on tubes was chosen low (1 kV) to have the same gain as it would be at full voltage (2.5 kV) in a 2 T magnetic field. The amplified signals from tubes went to ADC. The amplitudes of pulses were measured when cosmic muons crossed the counter. The energy of cosmic muons was measured by their range in lead. Two pulse height spectra from one of the phototubes are shown in Fig. 9.4. There are the results obtained in two different conditions: with muon momenta less than 340 MeV/c (no Cherenkov radiation in aerogel) and with muon momenta greater than 1.1 GeV/c (more than 88 % of full Cherenkov radiation

). From relativistic particle the total number of photoelectrons on two phototubes in the prototype counter was obtained equal to 6.3 $\pm$ 0.2. The main parameters of the Cherenkov counter are the detection efficiency for particles which give Cherenkov radiation versus the efficiency for particles which don't give this radiation. The dependence of the prototype detection efficiency versus muon momenta is shown in Fig. 9.5. Muons were assumed to be detected if any pulse height of tubes was greater than some threshold one. The curve in Fig. 9.5 was obtained by calculation which was based on the knowledge of the aerogel refractory index and number of photoelectrons from relativistic particles. In the calculation of efficiency for low momentum particles we took into account the Cherenkov light from delta-rays and the light from paint produced by the crossing particle.

The area of the prototype counter was about 200 cm^2. According to calculation we expect near 4.5 photoelectrons from relativistic particle in those counters with 400 cm^2 area and so 99 % detection efficiency. Due to nuclear interaction of hadrons with matter in front of the Cherenkov counters their detection efficiency will be lower of about 1 % in the barrel part of the detector and about 4 % in the endcup.

The obtained results show the possibility to realize a system of aerogel Cherenkov counters which are able to work in the high magnetic field of the detector and can extend the range of π/K separation up to 1.9 GeV/c. It significantly improves the reconstruction of B-mesons decays.

In order to construct the whole system of these Cherenkov counters we need 360 pieces of Hamamatsu phototubes R2490-01. We don't know a real alternative to these tubes now. For their purchase we need about 360 thousands dollars and this is the main problem concerned with the Cherenkov counters. If this problem will be solved we can produce the counters according to the following scheme :

1990 - design of counters
- organization of the production of aerogel with size $20\times20\times2.5$ cm^3

1991 - production of counters
- production of aerogel (70 %)
- design and production of electronics
- painting of counters (10 %)

1992 - end of aerogel production
- end of counter painting
- assembling of counters
- installation of counters in detector

1993 - beginning of work

References

1. G.Poelz, Nucl.Instr.and Meth. A248 (1986) 118

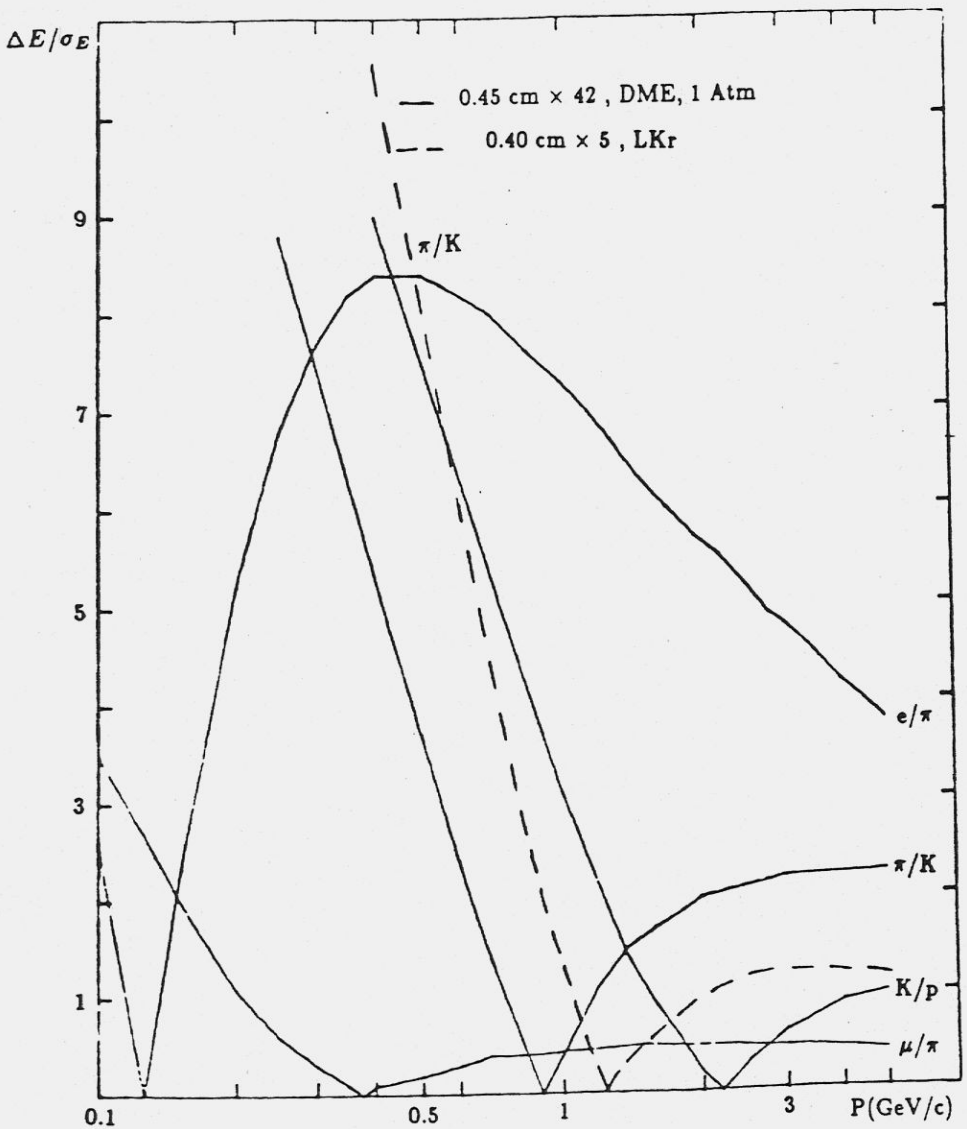

Fig. 9.1 Level of particle separation by dE/dx measurements in the drift chamber (solid lines) and in the liquid krypton calorimeter (dashed line)

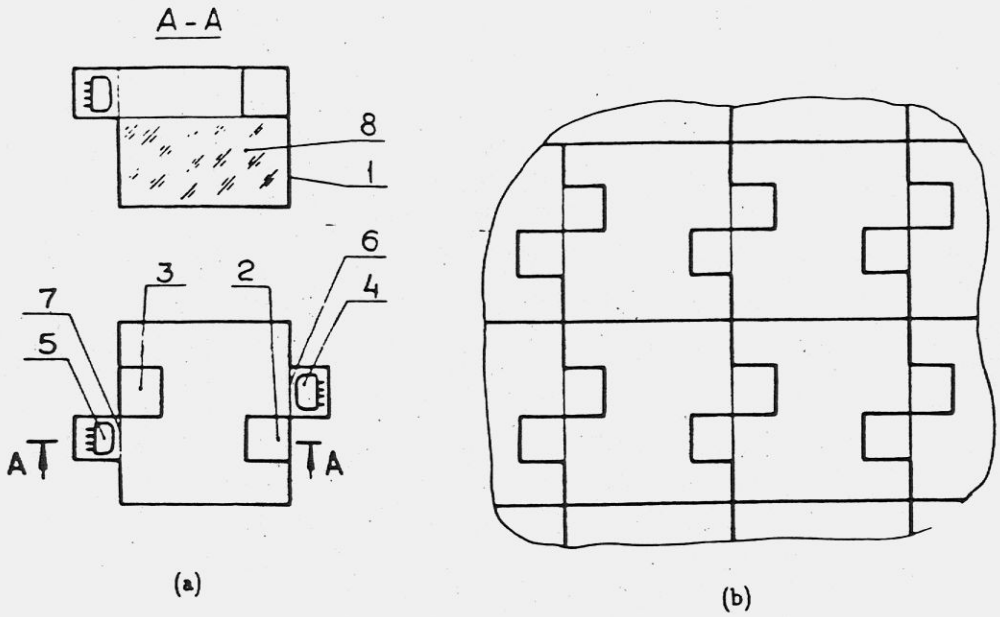

Fig. 9.2 (a) Schematical design of Cherenkov counter : 1 - walls of counter ; 2,3 - pockets for installation of phototubes from neighbour counters ; 4,5 - phototubes ; 6,7 - windows in walls ; 8 - aerogel ; (b) Layout of the counters in the barrel part of detector.

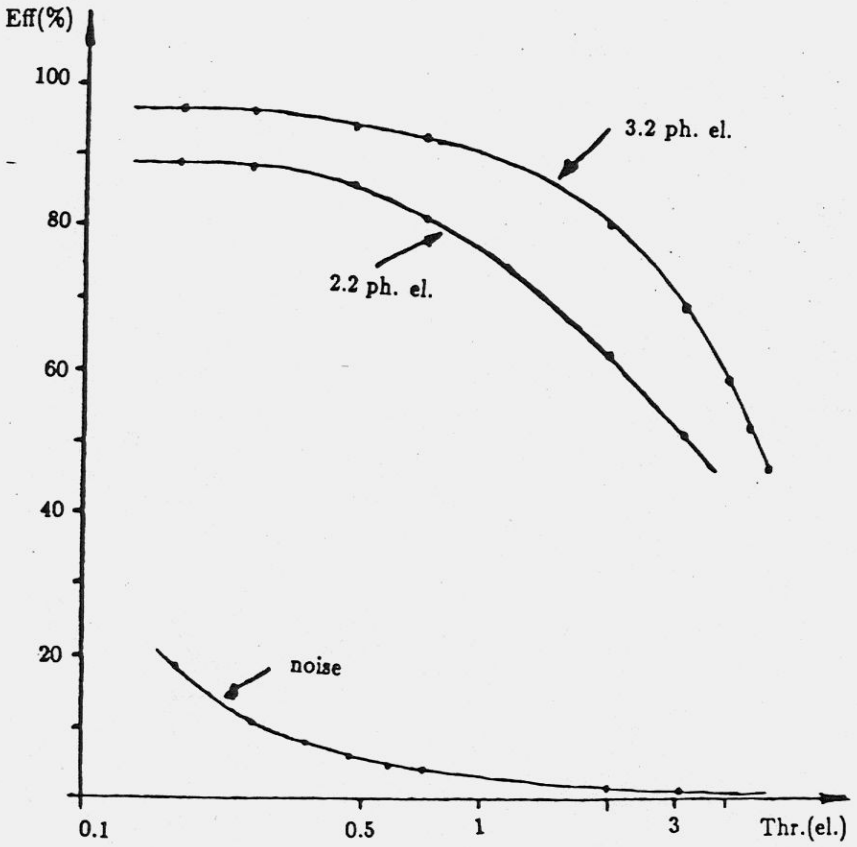

Fig. 9.3 Detection efficiency of weak light flashes by a phototube R 2490-01, working i a 2 T magnetic field environment. Average number of photoelectrons are show near the curves.

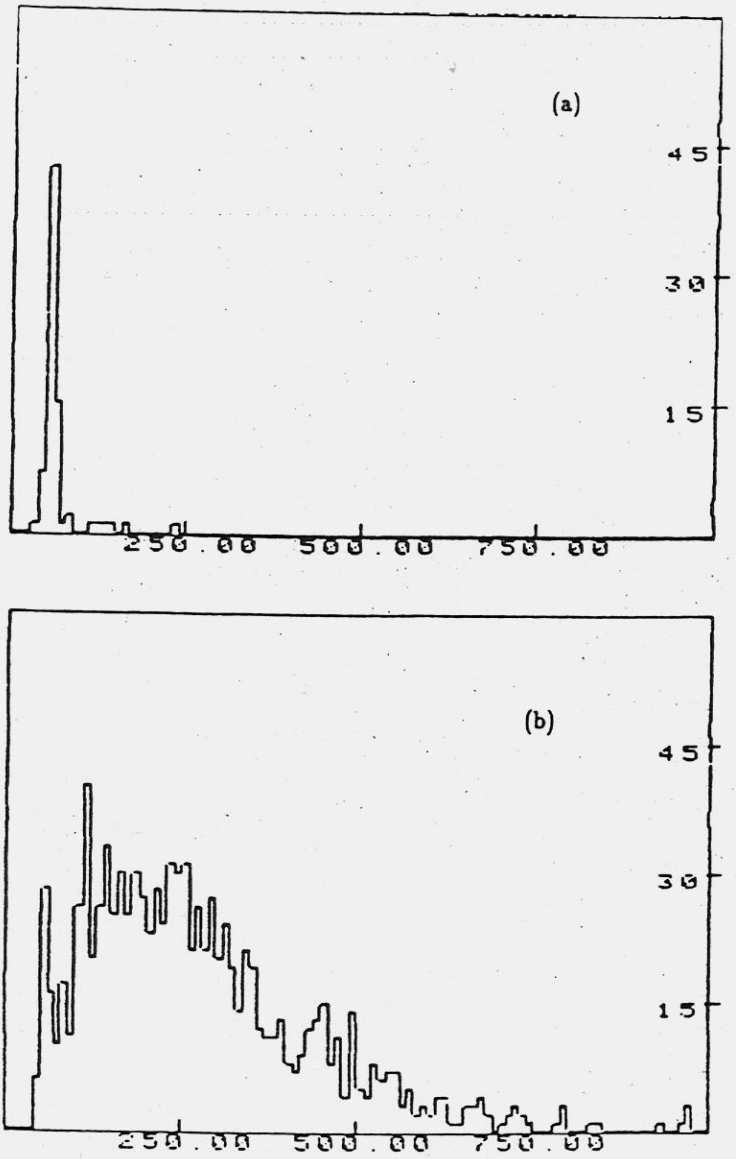

Fig. 9.4 Pulse height spectra from one of the two phototubes in the Cherenkov counter prototype : (a) - spectrum from muons with momenta less than 340 MeV/c ; (b) - spectrum from muons with momenta greater than 1.1 GeV/c.

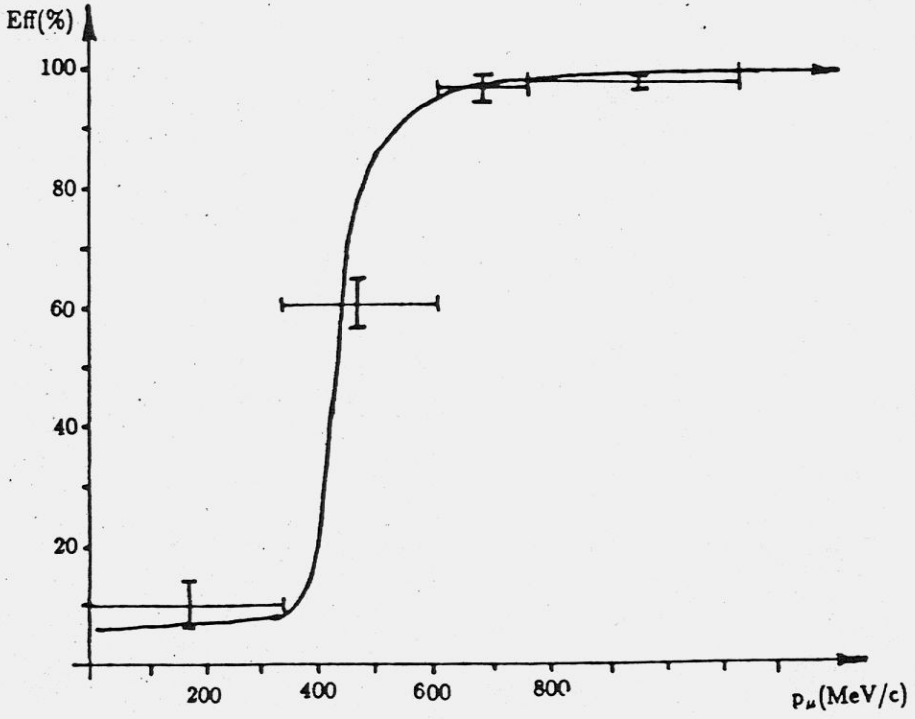

Fig. 9.5 Detection efficiency of muons versus their momentum in the Cherenkov counter prototype

10. Electromagnetic calorimeter

10.1 Endcap electromagnetic calorimeter with CsI crystals.

The main goals of the endcap electromagnetic calorimeter based on cesium iodide crystals are the measurement of the γ-quanta energy in a wide range (50 MeV - 3 GeV) and the electron-hadron separation. The properties of CsI scintillators are described in several works (see,for example, Refs. 1,2). This calorimeter, covering a solid angle of about 0.19 4π sr, consists of two endcaps with the basic characteristics listed in the following table.

Table 10.1

Type of crystals	CsI(Na)
Number of crystals	1200 arranged in 600 double blocks
Crystals sizes, $[mm]$	$60\times60\times150$
Total thickness	$30cm$ or 16.1 X_0
Total mass, $[ton]$	3
Readout	$50mm$ vacuum phototriodes CSPA, SA($\tau \simeq 3\mu s$), ADC
Signal level	$2000ph.el./MeV$
Electronic noise	$250 + 6C(pF) = 0.2MeV/crystal$
Energy resolution	2% at $1000MeV$ 3.5% at $150MeV$
Spatial resolution	6–$12mm$ depending on energy

The scheme of one module is shown in Fig.10.1. Two CsI crystals covered by optically transparant laquer and wrapped by a white teflon tape are placed inside common aluminized mylar container. The edges of it are fixed with special details and mylar is shrinked by short heating. Each crystal is viewed by a 52 mm phototriode through a 2 mm thick glass window glued to the scintillator with an optical epoxy.

Some test measurements were performed with a prototype, in order to study the CsI calorimeter with phototriode readout. This prototype was a matrix 5×5 elements containing a central crystal of $60\times60\times300$ mm^3 size and 24 double blocks described previously. In this work 30 mm phototriodes with the value of quantum efficiency times gain equal to 50-70 % were used.

The electronics channel consists of a charge-sensitive preamplifier (CSPA), a shaping amplifier (SA) with $3\mu s$ shaping time and a 4096-channel ADC.

This prototype was exposed to electrons of ETAP device produced by bremsstrahlung photons emitted from VEPP-3 [3].

The energy and space resolution obtained in these mesuarements are presented in Fig.10.2. The value of the energy resolution, σ_E/E , varies from 3.5 % at 160 MeV to 1.6 % at 1200 MeV.
At the present time the necessary number of crystals is available in the Institute. The distribution over lightoutput and its inhomogenity for a small sample of delivered crystals are shown in Fig.10.3. Double blocks are being produced now and this work is planned to be completed in the first quarter of 1991. The support construction is under design now and it could be produced at the beginning of the 1991. Thus, we plan to complete the endcap calorimeter toward the middle of 1991.

10.2 The electromagnetic calorimeter based on liquid krypton

10.20 Introduction

The use of noble condensed gases as calorimeter media is attractive due to the possibility to have not only a good energy resolution (like NaI and CsI calorimeters) but a better space resolution for photons.
Longitudinal segmentation can provide information for particle identification by dE/dx and also e/π–separation based on the longitudinal structure of the shower.
The best material for this aim is of course liquid Xenon, but it is impossible to get the necessary amount of it in reasonable time. Therefore we have stopped our choice on the next candidate - liquid krypton (LKr).
A sufficient amount can be obtained before the beginning of the experiment [5].

10.21 The main properties of LKr

The main physical properties of LKr are presented in Tables 10.21 and 10.22 together with other materials for calorimeters.

Table 10.21

	NaI	CsI	BGO	BaF_2	LAr	LKr	LXe
$\rho[g/cm^3]$	3.67	4.50	7.13	4.90	1.41	2.45	3.06
$X_0[cm]$	2.59	1.85	1.12	2.10	13.5	4.60	2.80
$\lambda_0[cm]$	41	84	22	30	84	60	55

Table 10.22

	Ar	Kr	Xe
T (boiling at 1 atm),[K]	87.3	119.8	165.1
T (freezing at 1 atm),[K]	83.8	116.0	161.4
liquid/gas density ratio	784	641	519
ionization energy, [$eV/pair$]	24.4	20.5	15.6
dE/dx, [MeV/cm]	2.3	3.4	3.9
e^- drift vel. at $1kV/cm$, [$mm/\mu s$]	1.8	2.4	2.2

10.22 LKr calorimeter design

A combined decision has been chosen for KEDR calorimeter: an endcap shower detector made of CsI crystals and a cylindrical (barrel) part built of LKr ionization chambers. The electrodes of the chambers are made of G10, foiled by copper. The thickness is 0.5 mm of G10 + 2×18 μm of Cu. A gap of 20 mm width is formed by the cells of thin G10 spacers. The internal radius of the calorimeter is equal to 75 cm and the thickness is 68 cm, i.e. 15 r.l.. Due to the small electrodes thickness, the calorimeter is practically homogeneous in contrast to the usual liquid argon one, where the energy resolution is determined mainly by the sampling fluctuations.
The signal read-out is carried out from high voltage electrodes, divided into rectangular pads, forming towers, oriented to the interaction point. The entrance size of the towers is 10×10 cm^2. In the radial direction all the towers are divided into three layers. The grounded electrodes of the first layer (30 cm thickness) are divided into strips of about 5 mm width in the direction along the beam line (z-axis) and in the orthogonal one (ϕ). These strips are used for the measurement of the photon coordinates. There are in total 8 strip layers for coordinate measurements. The width of the towers and z-strips is increased along the z - axis to provide uniform resolution in the polar angle. The electrode system is inserted into an hermetic aluminium volume. For the thermostabilization this volume is located inside another one made of stainless steel. The space between the walls is occupied by shield–vacuum thermo–insulator. The cooling of the cryostat is realized by liquid nitrogen pumping through the tubes welded to the walls of the internal volume under the pressure of 20 bar. The thickness of the entrance wall is 1 mm of stainless steel and 14 mm of aluminium, for a total 0.2 r. l.. The lay-out of the calorimeter is shown in Fig.10.4 and 10.5. The total amount of

LKr in the calorimeter is 35 t.

10.23 Electronics

The ionization chambers of the calorimeter are operated in the electron - pulse mode. The electrons drift time at the electric field of 1 kV/cm is close to 10 μs. Measurement of the collected charge is provided by charge sensitive preamplifiers based on FET SNJ-903L. With the RC-2CR shaper with a time constant of 1 μs the equivalent noise charge (rms) is $< ENC >$ =750+3.2· C (pF) units of electron charge. For the typical value of the tower electric capacitance (C) 300 - 500 pF, $< ENC >$ is about 1500 - 2500 electrons. The digitalization is carried out by ADC operating in the peak detecting mode.
The total number of electronics channels is 7240, among them: towers - 2304, z - strips -1864, ϕ - strips - 3072.

10.24 Energy resolution

The energy resolution of the LKr calorimeter is mainly determined by the following factors :

- Longitudinal (L) and Transverse (T) fluctuations of the energy leakage
- Sampling fluctuations in the dead materials (S)
- Geometric (induction) effect (G)
- Electronics noise (N)
- Radioactivity of LKr (R)
- Variation of the gaps (V)
- Calibration inaccuracy, electronics instability
- Algorithm of energy reconstruction

Fig. 10.6 shows the result of Monte-Carlo computation of the contribution of the longitudinal leakage and sampling fluctuations (L+S). The simulation was made for the real structure of the calorimeter in the presence of the magnetic field. The result is 1.8 % at the energy 0.1 GeV and 1.1 % at 0.5 GeV.
The contribution of the transverse leakage (T) is presented in Fig. 10.7, for the case when a photon falls on the calorimeter at some distance (dx) from the boundary between two large blocks. The fluctuations of the energy leaking the neighbouring block are shown also in Fig. 10.7. These data are useful for the estimation of the energy resolution in events with photons close in space. If for example photons have an energy about 0.5 GeV and are at a relative distance of 16 cm, their energy can be reconstructed with a 3 % accuracy.
The geometric (induction) effect (G) arises from the dependence of the collected charge on the ionization distribution inside the gap. The magnitude of this effect is decreased with the ratio (r) of the charge integration time to the electron drift time. The calculated energy dependence of this effect at r=0.1 is shown in Fig.10.8. This

dependence can be well fitted by the following simple function: $G(\%) = 0.84 \cdot E^{-0.4}$ (GeV).

The contribution of the gap size variation (V) is shown in Fig.10.9 as a function of the ratio σ_d/d, where d is the gap size, and σ_d - its rms variation. This contribution is V = 1.7 % at the energy 0.1 GeV and 0.8 % at 0.5 GeV when σ_d/d=5 % .

The electronics noise has to be treated together with the LKr radioactivity, which arises due to an admixture of the β- active isotope Kr^{85} . The end of the β spectrum is 0.67 MeV, the mean energy is 0.25 MeV and the half decay time is 11 years. In 1 cm^3 300 decays per second occur. The electronics and radioactive noise contribution is shown in Fig.10.10 versus time constant of the RC-2CR shaper containing 1 integrating and 2 differentiating cells. The calculation has been performed for a tower channel with an electric capacitance of 250 pF and LKr volume equal to 5000 cm^3. The equivalent noise of one tower is 1.0 MeV, the time constant is 1 μs.

Taking into account the above effects, the energy resolution as a function of the photon energy is shown in Fig.10.11 .

The results of using two different algorithms are presented; the former is obtained by summing the amplitudes of 27 towers (the full size is 30×30×70 cm^3); the latter by summing the optimal (for each energy) number of towers from the same volume. The result of the best (second) algorithm can be fitted by the following simple formula :

$$\sigma_E/E = 1.9\% \cdot E^{-0.4}(GeV)$$

10.25 Space resolution

The space resolution is determined by the strip width and by multiple scattering in the case of anode read-out. In Fig.10.12 the space resolution is calculated as a function of the photon energy by Monte-Carlo method. The strip width is 5 mm and a magnetic field of 2.0 T is taken into account. For a photon energy greater than 0.5 GeV, $\sigma_z = \sigma_\phi$ = 1.4 mm, while for an energy equal to 0.1 GeV the main contribution is given by multiple scattering and the result is σ_z = 4mm and σ_ϕ = 8mm (conversion occurs in the z - layer).

For the cathode readout one can have much better resolution using the center-of-gravity technique, as it is described in the 10.27 section.

10.26 Particle identification

Pulse height measurements from the strips can be used for charged particles identification by the dE/dx method. The calculation shows that π/K separation could be done at the level > 2σ up to the momentum of 1 GeV/c.

10.27 Experimental results

For the experimental study of the LKr technique we built two prototypes: Prototype-7 (7kg of LKr) and Prototype-400 (400kg of LKr). The first one was aimed at the

measurement of the space resolution for the charged particles. It consisted of four ionization chambers with a gap of 1 cm. The electrodes were made of foiled G10 with a 15 cm diameter and a thickness of 1 mm (Fig. 10.13). The read-out electrodes were divided into 5 strips each one with a width of 1 cm, all oriented in the same direction. The high voltage was applied to five solid electrodes, connected one to another. Signal processing was carried out by charge sensitive preamplifiers, RC-CR shaper and a peak ADC connected to each strip. The time constant of the shaper was 3 μs, the drift time was about 5 μs at a high voltage of 1 kV.

The quantity of LKr was 3000 cm^3 . To provide thermostabilisation the stainless steel volume containing the electrodes system was inserted into an external volume also filled with LKr and surrounded by foam plastic thermoinsulator. In the experiment with cosmic particles we obtained a space resolution $\sigma_x = 3$ mm in the anode readout mode and $\sigma_x = 0.4$ mm in the cathode readout with the center of gravity method. The result of cathode readout is shown in Fig.10.14. The details of this experiment are described elsewhere [7].

The experiment with the Prototype-400 was devoted to the energy resolution measurement. The electrode system consisted of 19 flat ionization chambers, the gap being 20 mm wide. The thickness of electrodes was 0.5 mm G10 + 2×35 μm of copper. The diameter of this calorimeter was 45 cm, the length being 76 cm. All odd electrodes were connected to charge sensitive preamplifiers based on FET SNJ-903L. All even electrodes were connected one to another and they were used as high voltage electrodes.

Signal processing was carried out by an RC-2CR shaper and peak ADC. The Prototype-400 lay out is shown in Fig.10.15.

The experiment was performed with positrons obtained by the conversion of the single bremsstrahlung photons from the VEPP-3 circulating electron beam. The positron momenta were measured by a magnetic spectrometer and could be varied in the region from 0.13 to 1.2 GeV/c.

The details of the experiment are described in the paper [7] and the results are shown in Fig. 10.16 and 10.17. The obtained energy resolution is practically the same as that obtained in CLEO-II and KEDR CsI calorimeters prototype experiments.

We have performed a new experiment with Prototype-400 during the period from March to April 1990 . The electrode system was replaced by that close to the KEDR calorimeter electrode structure, containing towers and strips. It also included the possibility of read-out from both sides of the ionization chambers. The data analysis is now in progress.

10.28 Front-end electronics

For signal processing associated with the liquid Kr calorimeter two goals have been set forth. One of them, which had to be achieved on a very short time scale in order to provide a solution of immediate use, was the development of discrete junction field-effect transistors with gate width W intermediate between the existing $2.2 \cdot 10^4$ μm of NJ 903 and the $9 \cdot 10^4$ μm of NJ 3600. This device has to provide better conditions

of capacitive matching in the amplification of signals from the calorimeter and should be employed as a front-end element in the hybrid preamplifiers that will be designed for that purpose.

A second project, which implies an advanced technological development and requires, therefore, a longer time scale aims at arriving at a monolithic charge-sensitive preamplifier intended for the replacement of the hybrid one. This project is presently being carried on and some results that have been already obtained and seem to be encouraging will be presented here. Both projects above are being carried on within the frame of a collabotration between the Pavia University and Milan INFN, the Instrumentation Division of Brookhaven National Laboratory and Interfet Co.

As previously said, the development of discrete junction field-effect transistors to be employed as input elements in the hybrid, thick-film, version of the front-end electronics for the liquid Kr calorimeter was assumed as a goal to be achieved on a very short time scale. The idea was to have a single type of device allowing a limited extent of capacitive mismatch in the amplification of the signals from both strips and towers in the calorimeter. Intentionally, the device had to lend itself to trasformerless operation with detectors of moderately large capacitance, 200 - to - 400 pF.

The target was a JFET of large transconductance/drain current ratio, able to yield outstanding noise performances at comparatively low power values, with an input capacitance around 200 pF. In developing such a device it was decided to reduce the length of the channel cycle, that is, the distance between the drain and source midpoints and, correspondingly, the gate length, to obtain over the existing devices also an advantage in terms of transition frequency. The device realised, called 1800D, has the gate structure shown in Fig. 10.18.

As shown in Fig. 10.18, NJ1800D is a large interdigitated structure. The total gate width W is about $4.4 \cdot 10^4$ μm. The transconductance characteristics of NJ1800D are shown in Fig. 10.19, where the transconductance g_m and the ratio g_m/I_D are plotted as functions of the drain current I_D.

As apparent from Fig. 10.19, the device at a current as low as 2 mA features a g_m of more than 33 mA/V, that is, a g_m/I_D ratio of about 17. These features make the device suitable as a front-end element in a monolithic preamplifier, as it presents a white noise spectral density of 0.6 nV/$\sqrt{Hz}$ at an acceptable low power consumption, about 7 mW. The low frequency noise behaviour of NJ1800D is good. The $H_f = A_f C_i$ coefficient of 1/f-noise, that is, the product of the spectral power density of 1/f-noise at 1 Hz and the device capacitance, is as small as $3.3 \cdot 10^{-27}$ J.

The program which produced as a result the 1800D JFET included also the design of tetrode structures with the same gate area as 1800D [8]. The name tetrode refers to a JFET configuration where the width of the conducting channel can be controlled by two independent gates. Such a configuration is obtained by making the gate fingers and the lateral P^+ diffusions isolated from each other. The fingers constitute the topside gate, while the substrate, along which the lateral diffusions that go all the way through into it, represent the backside gate. A problem which arises with the tetrode configuration is that the topside gate may present a non negligible spreading resistance, due to the fact that the fingers and the connecting bar are made of thin diffused

layers. Because of this, the tetrode may have a larger series thermal noise than the corresponding triode structure. To avoid this additional noise, the topside gate should be metallized, which creates non trivial problems of topological and technological nature. For instance, the 1800C tetrode has the structure of the topside gate shown in Fig. 10.20. The gate fingers run between two metallized gate bars, at 90^0 angles. Still , the gate fingers are not metallized, which seems responsible for an increase in the white noise spectral density over the value which, according to the measured g_m should be expected for the channel thermal noise. Effort aiming at removing this limitation by implementing a fully metallized structure of the topside gate is presently being produced.

Availability of a low noise tetrode structure may be of some importance in the domain of signal amplification with detectors of large capacitance, as it would openup interesting possibilities in the design of the feedback loops around the preamplifiers. Trasformerless capacitive matching with large JFETs and tetrode structures belongs to the discrete device program, which is still going on. The second program which is developing in the framework of the same collaboration, as previously said, aims at realising a monolithic preamplifier employing N-channel JFETs with epitaxial channel and diffused gate. It is known that this type of JFET provides the best noise performances. This statement is confirmed by the fact that the epitaxial-channel JFET, out of all field-effect devices, has the lowest amount of 1/f-noise and that its channel thermal noise complies quite accurately with the theoretically predicted expression of the spectral power density :

$$\frac{de^2}{df} = 4kT \cdot \frac{0.7}{g_m} \qquad (1)$$

In eq. (1), k is Boltzmann's constant, T the absolute temperature and g_m the transconductance.

In order to preserve the noise characteristics of the individual JFETs in going from the discrete structure to the monolithic implementation, dielectric isolation techniques have been considered the most suitable approch. Three different processes, illustrated in Fig. 10.21, are presently being employed during the preliminary realisations of the preamplifier structure.

As clarified in Fig. 10.21 one of the processes is based upon two different epitaxial layers, one P-type which will act as a part of the backside gate and one N-type, where the gate will be realized. The process b) employs dielectrically isolated tubs to house the different devices. Process c) makes use of dielectrically isolated mesas.

The circuit diagram of the preamplifier which has to be implemented in monolithic form is shown in Fig. 10.22. It employs only N-channel JFETs as active elements and a level shifter realized as a string of diodes. No resistors and no capacitors will be implemented on the chip, at least in the preliminary versions of the circuit. The feedback resistors R_f and the feedback capacitor C_f will be connected externally. As shown in Fig. 10.22, the preamplifier consists of a cascode (J_1, J_2) which has as an active load the current source made of (J_3, J_4) and J_7. J_7 has also a buffering function on the signal. J_9 is a second buffer. The signal goes through J_1, J_2, J_7

and J_9, that are realized as short channel devices (SC) in order to achieve a large gain-bandwidth product. All the other JFETs are employed in current sources. For them a large dynamic impedance at the drain output is essential. For this reason they are all realized as long channel devices (LC). The channel cycle is 15 μm for the SC elements and 25 μm for the LC ones [9].

The preamplifier shown in Fig. 10.22 has been simulated, optimised from the point of view of dynamic response and noise and realised in a breadboard version using, as discrete devices, the same JFETs that are foreseen for the monolithic version. The circuit has been realised, along with individual components and partial test structures, according to the three processes described in Fig. 10.21 [10]. Some of the monolithic circuits have already been delivered and are undergoing now the characterisation tests. As a very preliminary result, the JFETs realised with process a) have shown a transconductance behaviour which is very closed to that of discrete devices of the same gate size. Their noise behaviour, however, is not equally good and this seems to depend on a large gate spreading resistance which is present in the monolithic parts. The reason why this resistance is present has been understood and measures to remove it are now being taken.

10.29 The calorimeter prototype in Milan

Another small calorimeter prototype has been designed by the Collaboration and built at INFN Milan with the purpose of testing the new front-end electronics and of investigating the possibility to obtain the π-K discrimination by the dE/dx method. The usefull volume of the prototype is 6 l. For the first tests we use a system of electrodes consisting of 9 planes, 5 among them are cathodes. The distances between the electrodes is 2 cm and the electrodes are subdivided into strips, 1 cm wide.
The prototype has been tested by liquifing and retrieving argon. A data acquisition system based on peak-detecting SILENA ADCs with FERA read-out and CAMAC transfer to dedicated personal computer has been set up. The software has been written and tested. At present 32 channels of electronics and data acquisition are assembled. The preamplifiers make use of the newly-developed NJ1800D FET.

Time schedule

The LKr calorimeter will be put into operation in the middle of 1992. The time schedule is the following :

1990 - Obtaining of 22 t (65%) LKr
- Manufacturing of cryostat, Cryogenmasch, Moscow
- Manufacturing of storage vessels for LKr, Cryogenmasch,Omsk
- Manufacturing of electrodes (700 m^2 area), Italy
- Manufacturing of multipin hermetic feedthroughs (300 pieces), Novosibirsk
- Manufacturing of chamber electronics, 5000 chan., Italy

- Obtaining of 5000 high voltage capacitors, Italy

1991 - Assembly and testing of cryostat
- Assembly of the electrode system
- Manufacturing of the rest chamber electronics, Italy
- Assembly and testing of chamber electronics
- Manufacturing of digital electronics

1992 - Assembly and start of the external cryogenic system operation
- Obtaining of the rest LKr amount
- Assembly of the rest chamber electronics
- Mounting of LKr calorimeter into KEDR detector and start of the experiments

References

1. Yu. A. Tsirlin et al. Scintillation detection units. Moscow, Atomizdat, 1979.
2. M. R. Farukhi IEEE Trans. on Nucl.Sci. NS-29 (1982) pag. 1237
3. S. A. Belomestnykh et al., Proceedings of the IX All-Union Work- shop on Charge Particle Accelerators., Dubna 25-27 oct. 1988 v.I, pag. 410
4. E. Blucher et al., Nucl. Instr. and Meth., A249 (1986) 201
5. V. M. Aulchenko et al. Proceedings of the 24 International Conference on High Energy Physics, Munich, 1988 (contributed paper)
   V. V. Anashin et al. Proceedings of the International Simposium on Position Detectors in High Energy Physics Dubna,1988,pag. 58
6. C. N. Anisimov et al. Preprint ITEPH-16, Moscow, 1984
7. V. M.Aulchenko et al., Nucl. Instr. and Meth. A289 (1990) 468
8. S. Rescia, private comunication
9. M. Demicheli et al., Nucl. Instr. and Meth. A289 (1990) 418
10. L. A. Rehn and D. E. Roberts, Monolithic JFET preamplifiers for Ionization Chambers Calorimeters. Paper presented at the " International Industrial Symposium on Supercolliders ", Miami Beach (Fla), March 14 - 16(1990)

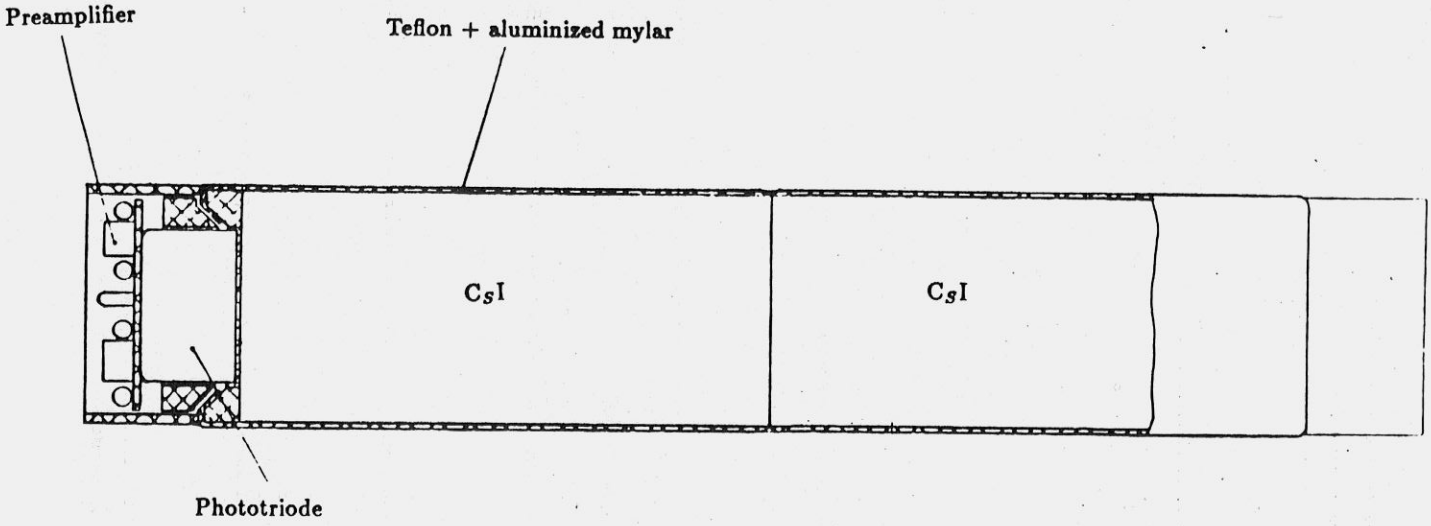

Fig. 10.1 Schematic view of the endcap module

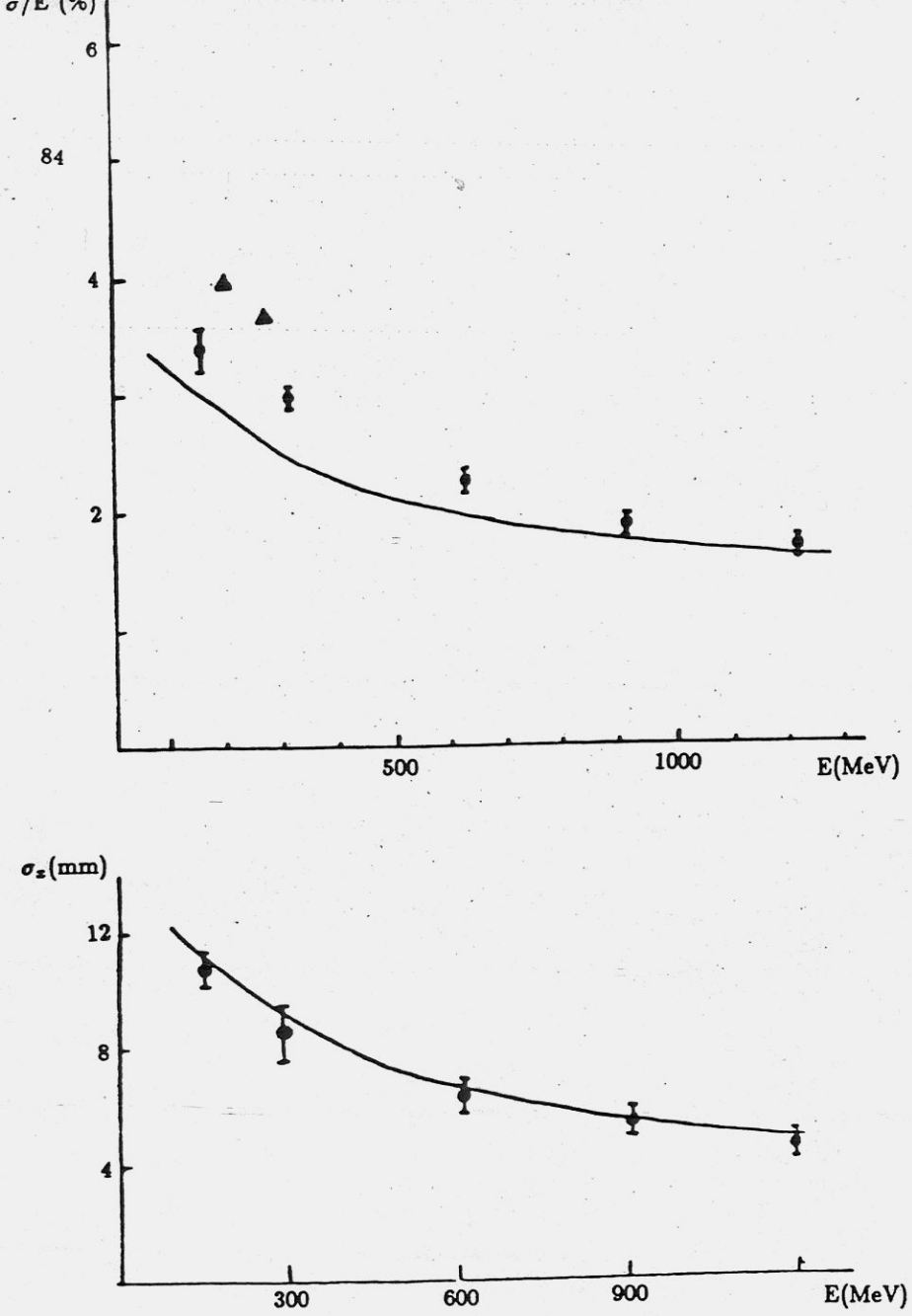

Fig. 10.2 The energy and position resolution obtained in this work – ● and CLEO-II[4] – ▲ . The curve corresponds to Monte-Carlo simulation.

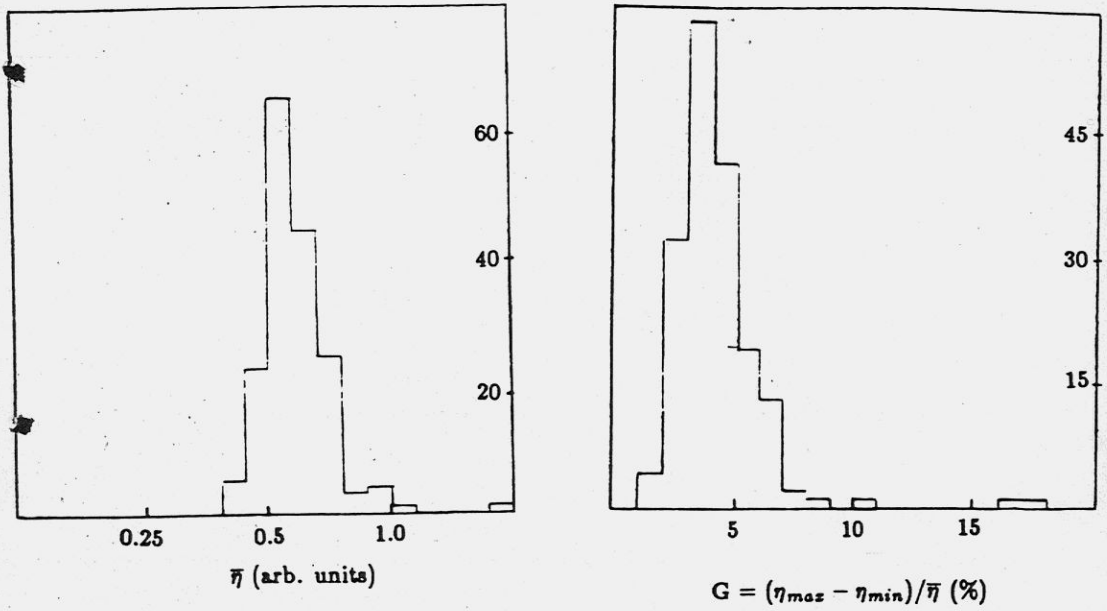

Fig. 10.3 The distribution over lightoutput (η) and its inhomogenity (G) for a sample of crystals.

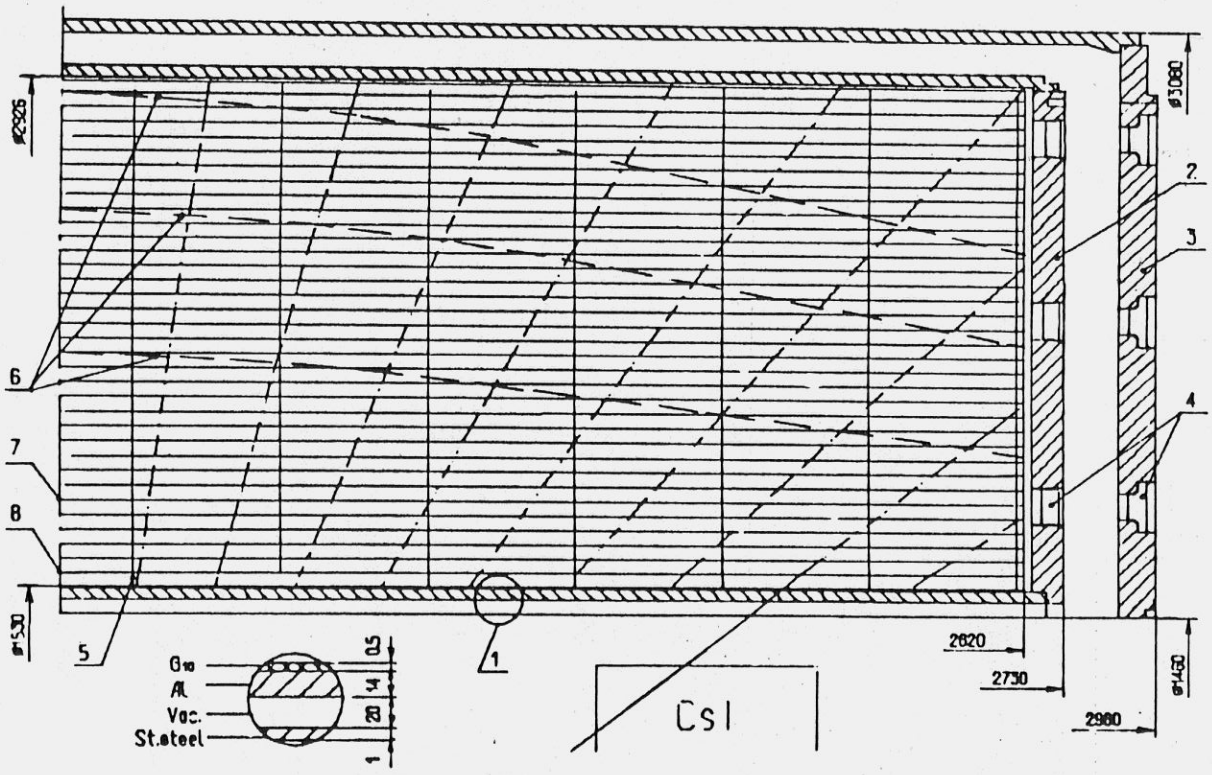

Fig. 10.4 Lay out of the LKr calorimeter. 1- entrance wall, 2-cold flange, 3-warm flange, 4- feedthroughs, 5- spacers, 6- lines of equal thickness, 7- strip electrode, 8- high voltage (tower) electrode

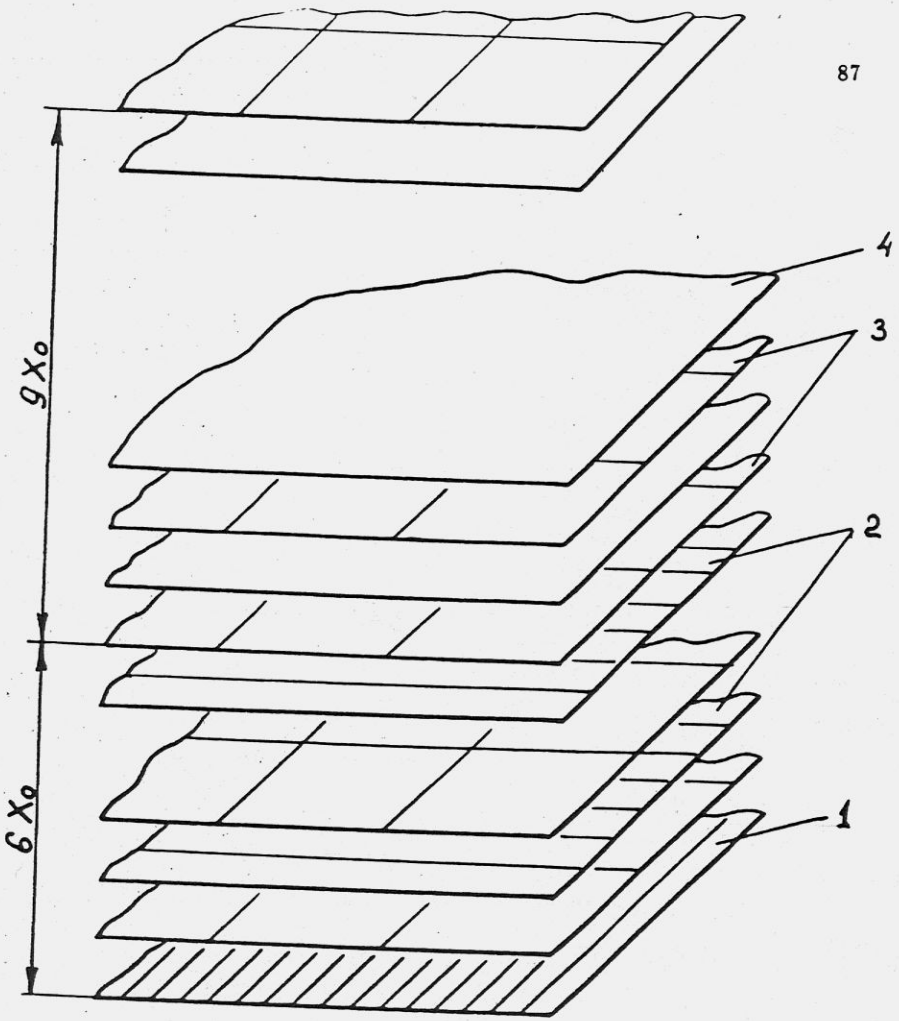

Fig. 10.5 Scheme of the electrodes structure. 1- z-strips, 2- ϕ strips, 3- towers, 4- grounded electrodes

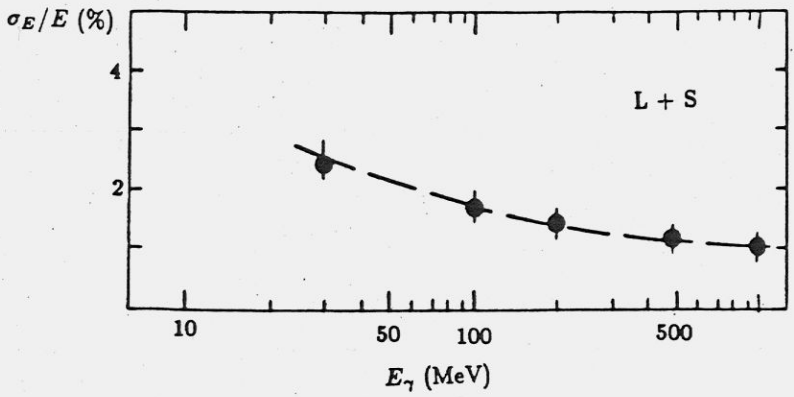

Fig. 10.6 Energy resolution. Contribution of the longitudinal leakage and sampling fluctuations

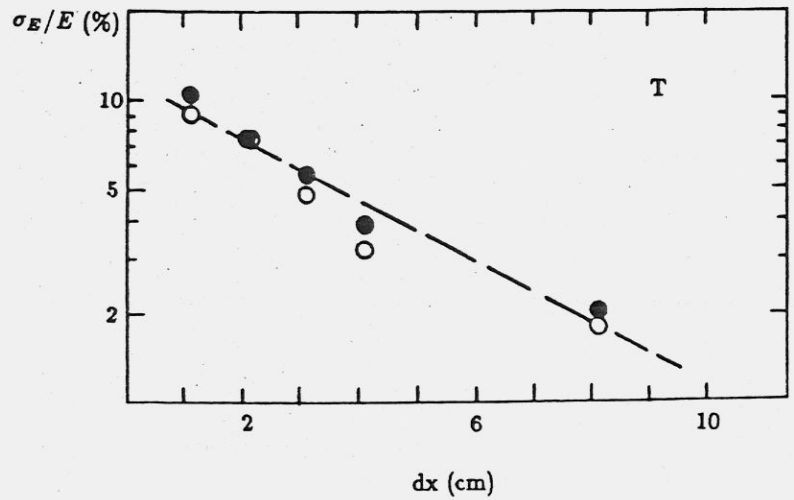

Fig. 10.7 Energy resolution. Fluctuation of the fraction of energy going to the neighbouring block as a function of the distance of the photon from the boundary between the blocks. Black circles - E = 0.1 GeV, open circles - E = 0.5 GeV.

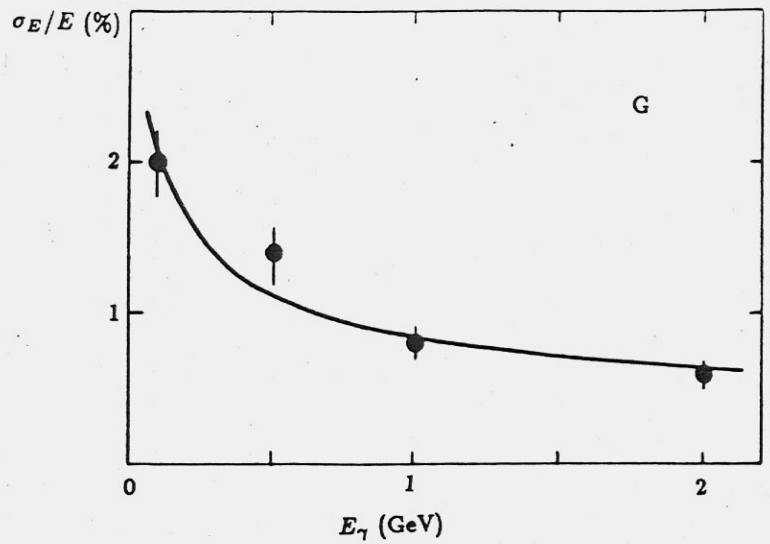

Fig. 10.8 Energy resolution. Contribution of the geometric effect; shaper time constant/drift time = 0.1

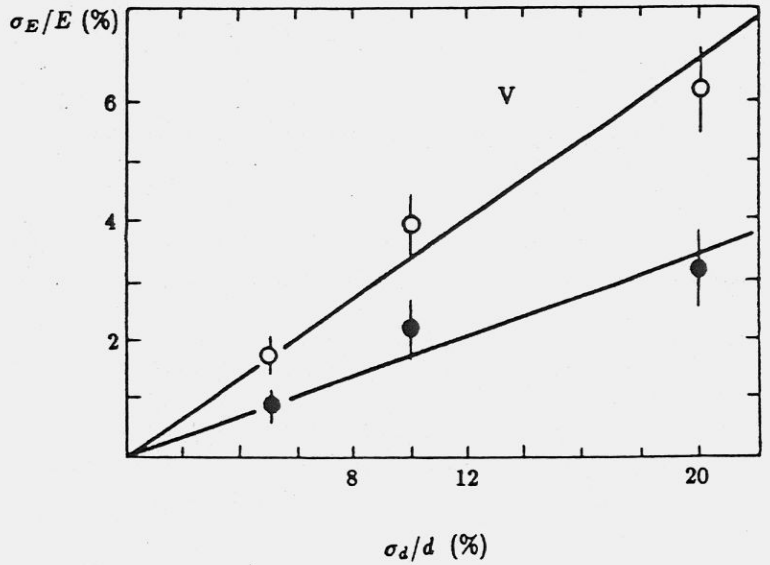

Fig. 10.9 Energy resolution. Contribution of the gap size variation. Black circles - E = 0.5 GeV, open - E = 0.1 GeV.

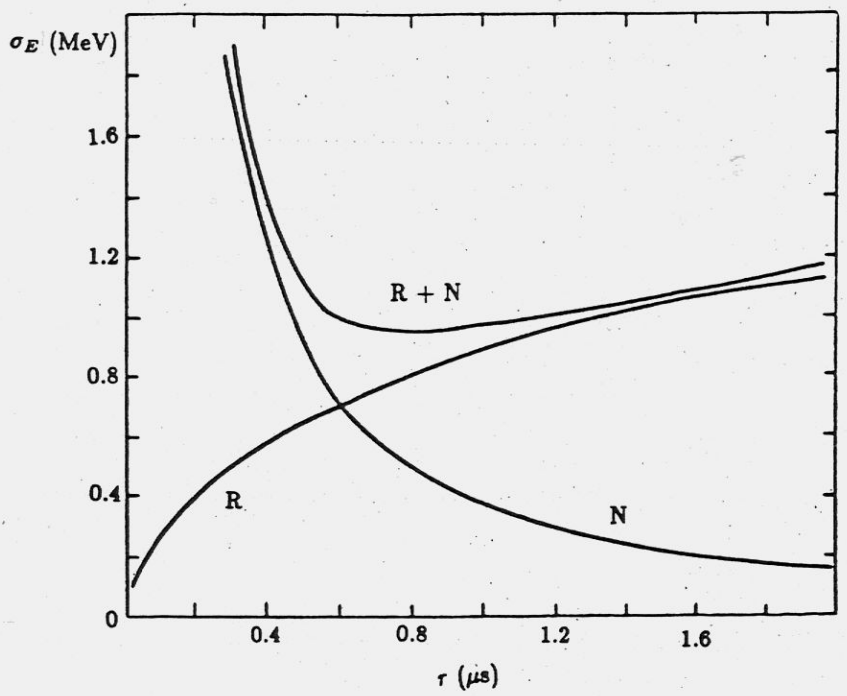

Fig. 10.10 Energy resolution. Electronics and radioactive noise for 1 tower versus time constant.

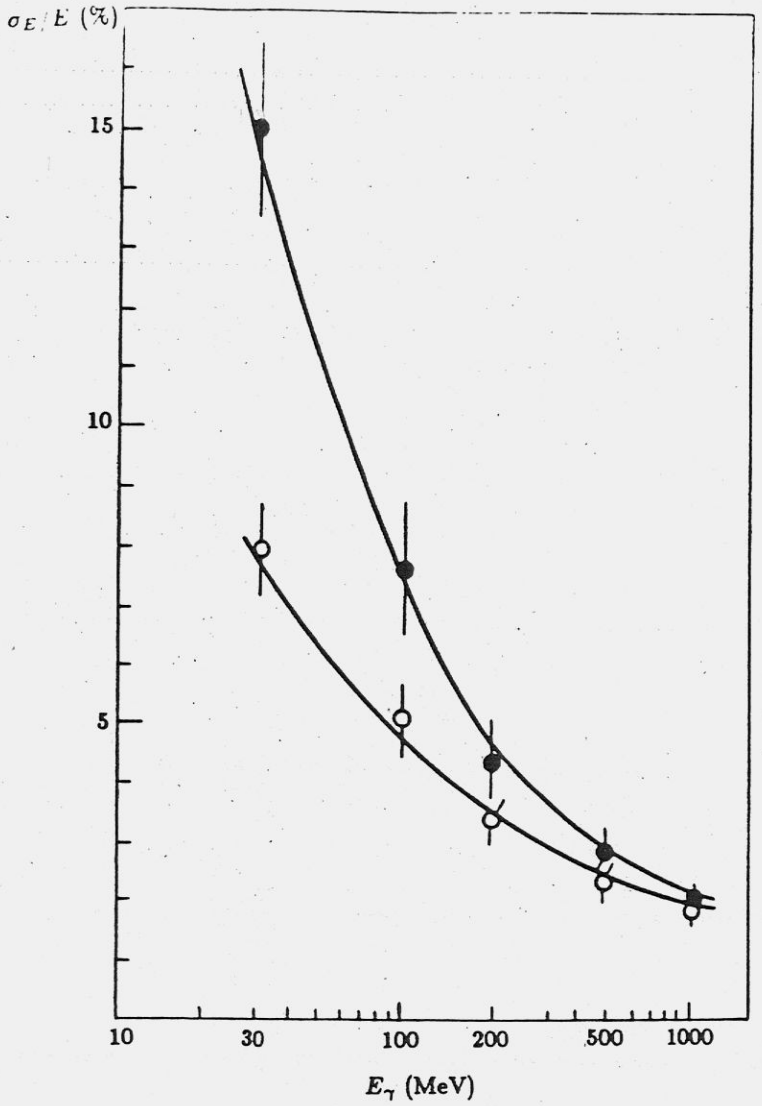

Fig. 10.11 Resulting energy resolution. Black circles- sum of amplitudes from 27 towers, LKr volume $30\times30\times70$ cm^3 , open circles - sum of the optimal number of towers amplitudes from the same volume.

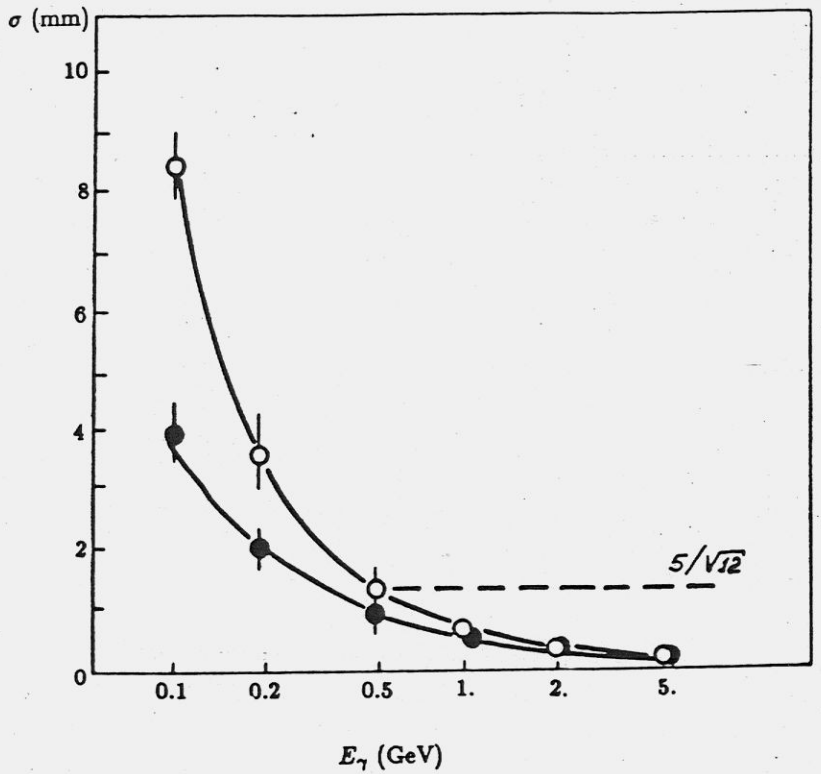

Fig. 10.12 Space resolution. Black circles- z-projection, open circles - ϕ-projection

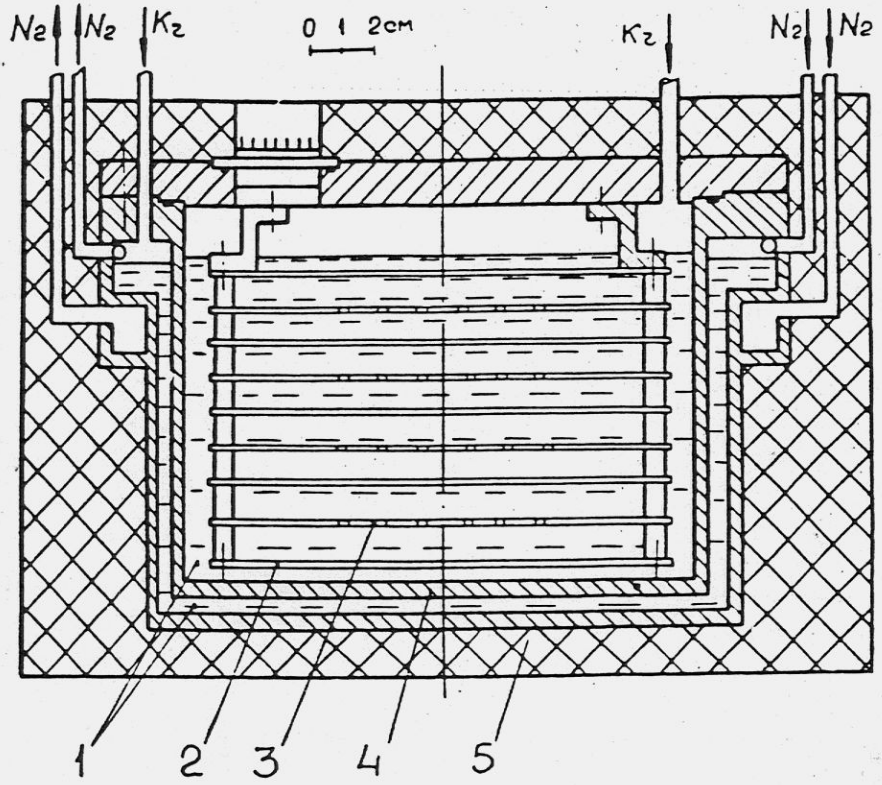

Fig. 10.13 Prototype-7 lay out : 1- LKr, 2- high voltage electrodes, 3- signal electrodes, 4- internal volume, 5- foam plastic

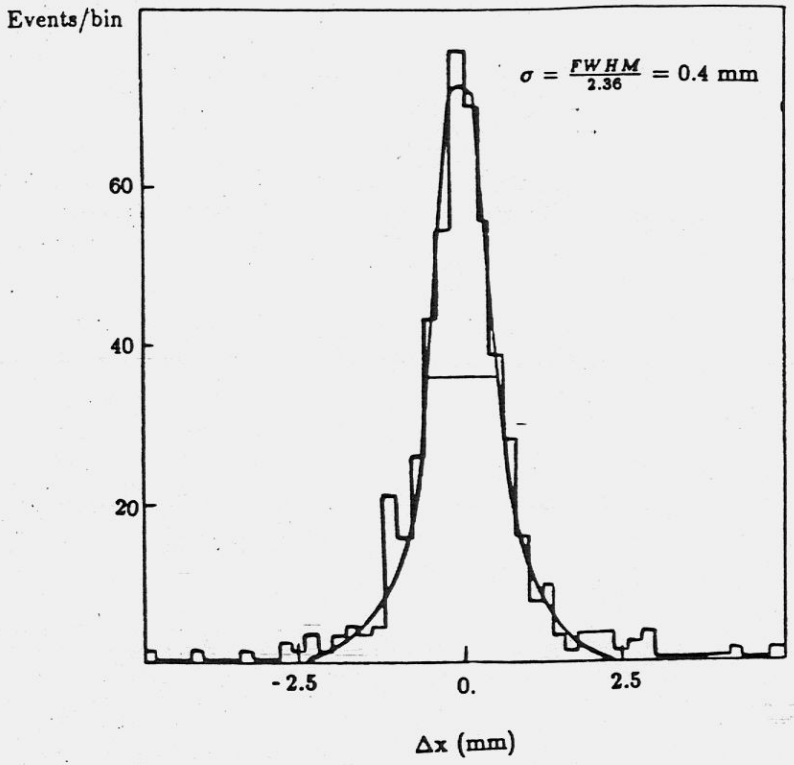

Fig. 10.14 Prototype-7 : space resolution with cosmic particles.

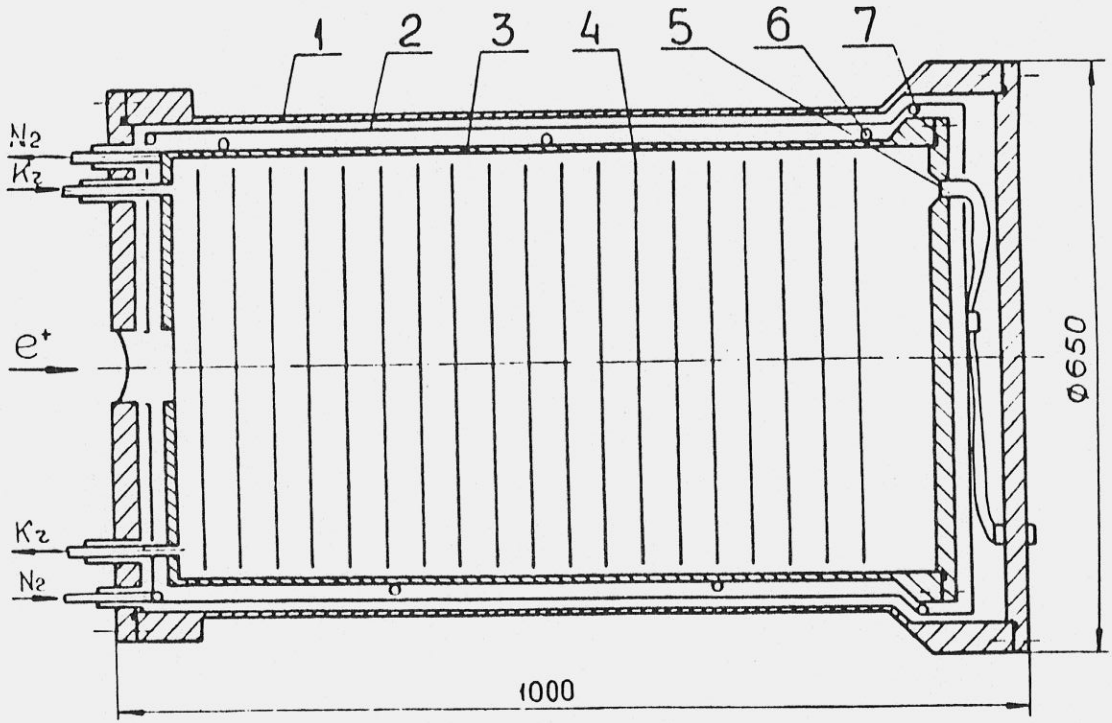

Fig. 10.15 Prototype-400 lay out : 1- external volume, 2- liquid Nitrogen copper screen, 3- internal volume, 4- electrodes, 5-feedthrough, 6,7- cooling pipes.

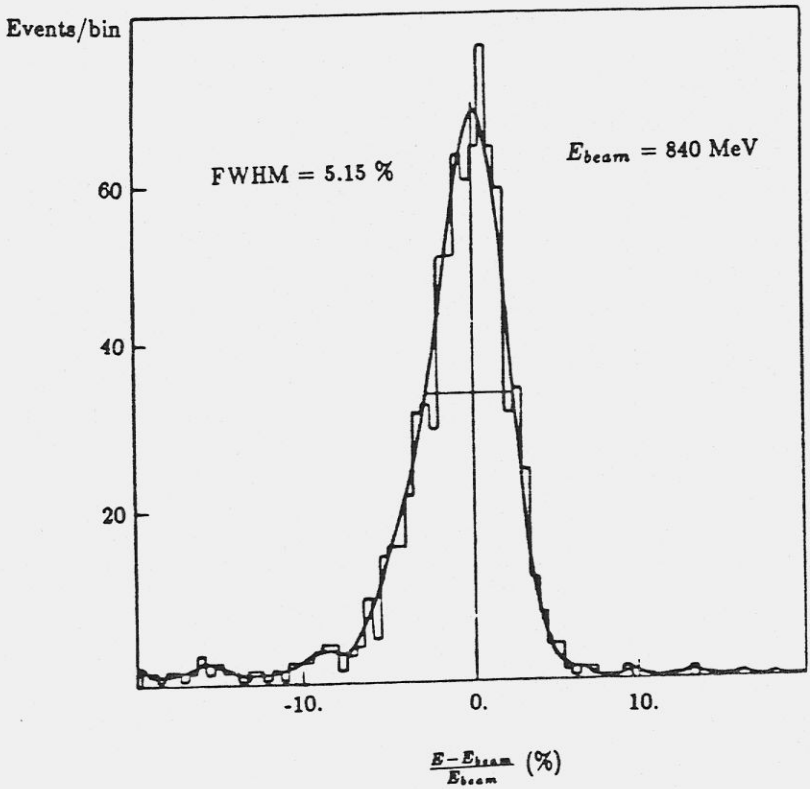

Fig. 10.16 Prototype-400 : energy resolution at E_γ = 840 MeV.

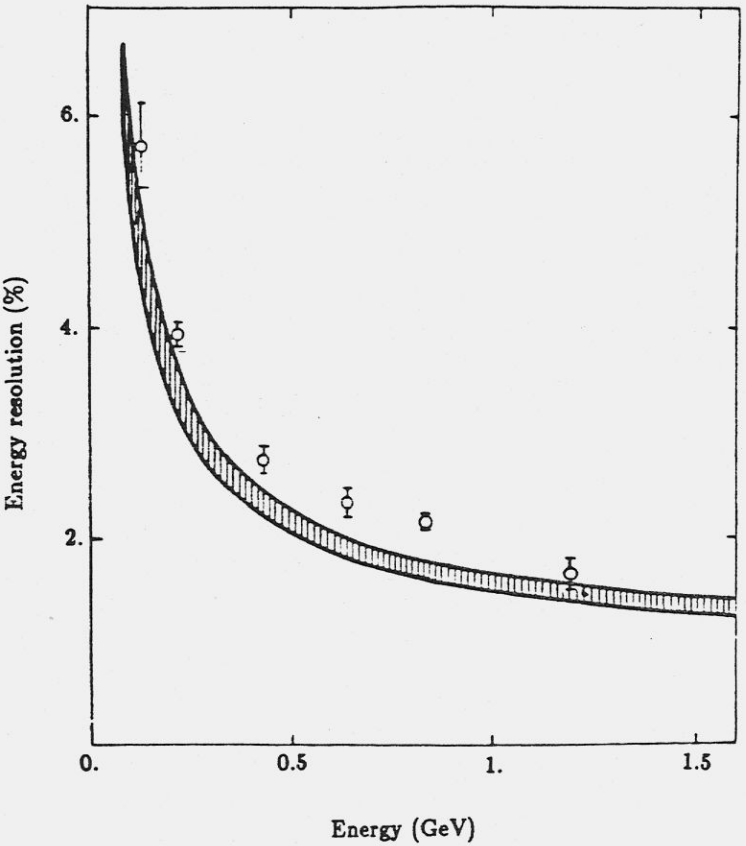

Fig. 10.17 Prototype-400 : energy resolution versus energy.

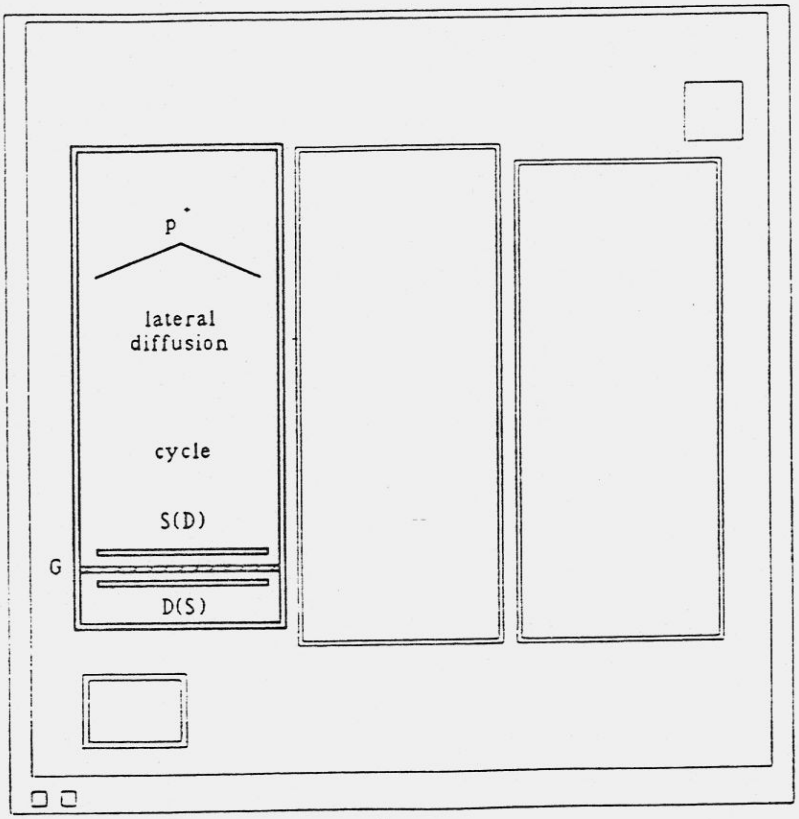

Fig. 10.20 - NJFET 1800D - device configuration.

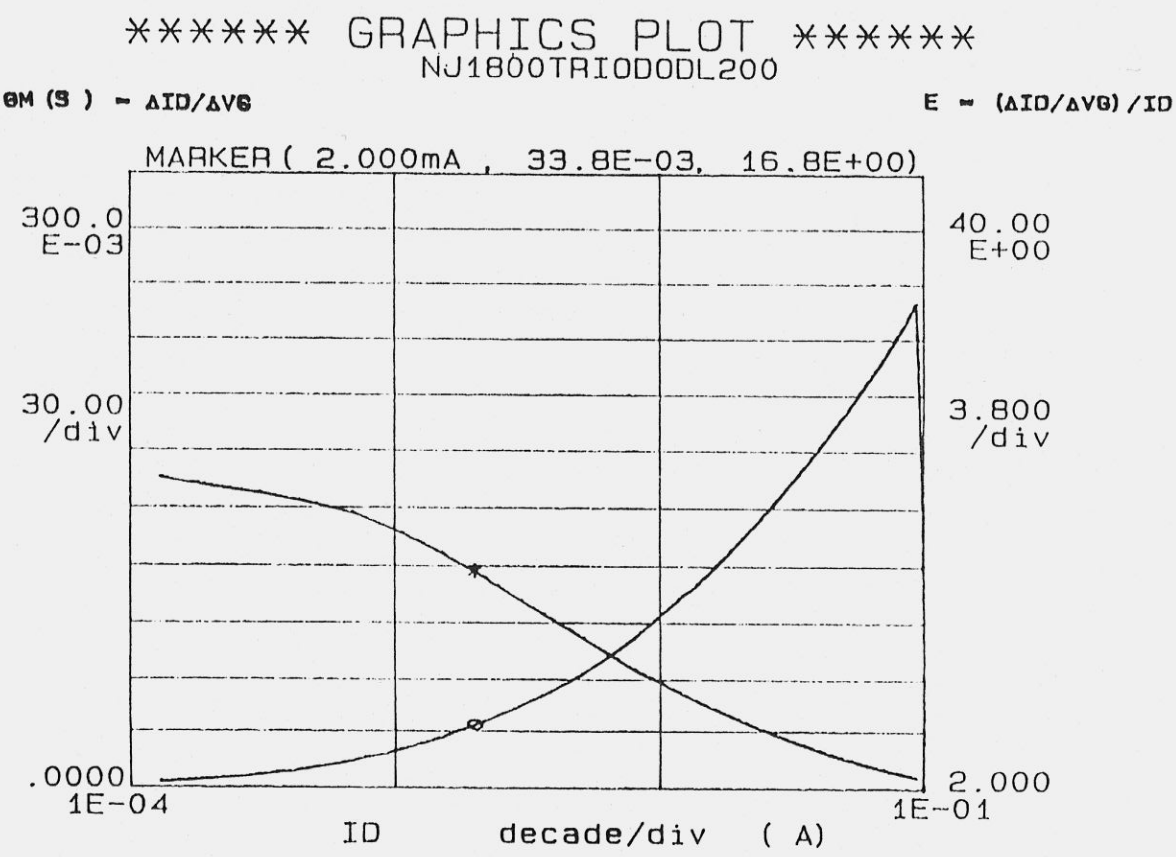

Fig. 10.19 -NJ1800D - Transconductance, g_m and g_m/I_D ratio as functions of the drain current I_D.

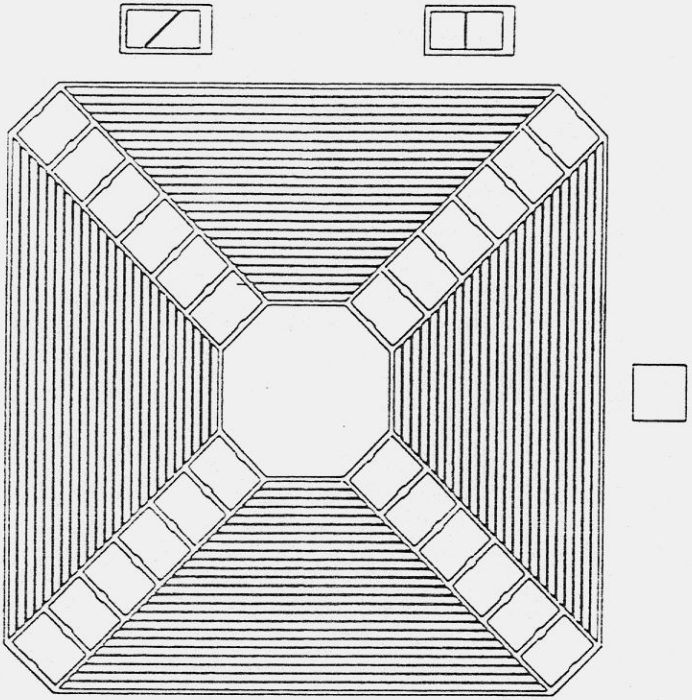

Fig.10.18 - Topside gate configuration of tetrode NJ1800C

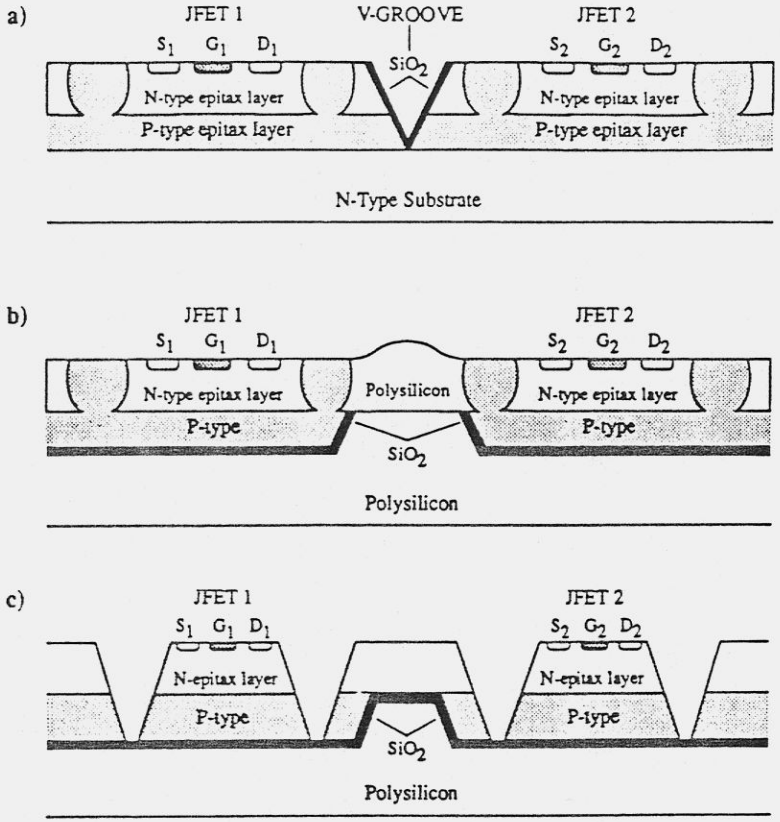

Fig. 10.21 Technologies being tested for the implementation of the monolithic preamplifier.
a) Double-epitaxial layer, V-groove isolation.
b) Dielectric isolation, individual tubs.
c) Dielectrically isolated mesas.

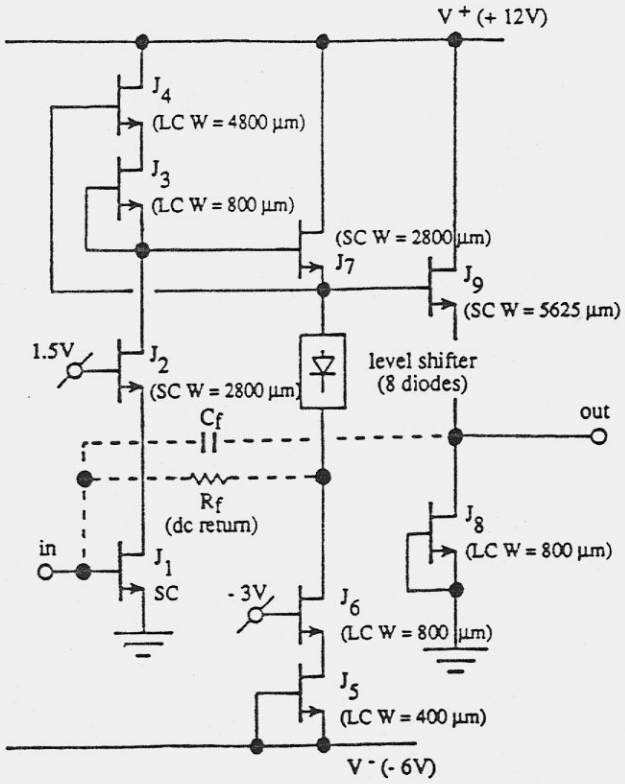

Fig. 10.22 Charge-sensitive preamplifier employing only N-channel JFETs and a diode level shifter.

11. Muon identifier

The main goal of the muon identifier is a reliable isolation of muons produced together with a considerable number of hadrons in $e^+ e^-$ annihilation.

A highly efficient identification of events with one and two muons is required to study semileptonic decays of B, D, and F-mesons, to determine the ψ-meson yield and to analise $\tau\tau$-events.

The muon identifier for the detector KEDR has a thickness of the hadron absorber of 6-7 nuclear lengths.

After each layer of absorber there is a layer of streamer tubes. The system comprises 8 octants covering 0.67 4π sr ($48^0 < \theta < 132^0$) and two endcaps, so that the total solid angle of muon identification system is 0.99 4π sr ($8^0 < \theta < 172^0$).

The total amount of the substance-absorber is determined by the desiderable coefficient of suppression of the hadron background for hard muons. The pions and kaons are capable of imitating muons either due to the probability to pass through the matter without nuclear interaction, or to the decay into a muon and a neutrino. The latter is possible if the angle between the direction of the muon and hadron motions is so small that the precision of coordinate measurements does not allow a kink in the track to be identified and the measured momentum does not contradict the range of a muon path.

Pions create a higher background for muon identification than kaons do because in the decay of Υ-mesons the number of charged kaons is 5 times smaller than that of pions. A marked kink in the track during the kaons decay is more probable than in the case of pion. Moreover, the kaon passed without interaction has a noticeable shorter ionization range of the pass in comparison with the muon with the same momentum (32-34 cm of iron). In view of this, if iron is divided into layers whose thickness is less than 25 cm (with possible angles of incidence taken into account), then the kaon is not capable to imitate the muon on account of the interaction-free path.

The probability of muon imitation due to the pion decay is determined by the length of flight in a matter of low density, i.e. by the radius of the identification system (60 cm in KEDR) as well as by the accuracy of tracking to find the kink.

For the pions, the probability of an interaction-free passage through matter decreases with increasing the total thickness of the absorber. The chosen thickness enables to make this probability lower than the muon imitation probability due to pion decay.

The whole of the absorber will be passed only by muons whose energy is higher than the threshold one (E=1.7 - 2.1 GeV), on account of ionization losses. For the hadron background suppression, in case of identification of muon whose energy is lower than the threshold, intermediate sensitive layers are necessary . These offer the possibility to evaluate the energy of the particle and to distinguish them with respect to the range.

The first sensitive layer allows the information of neutral hadrons (K_L and neutrons) to be gained.

In the chosen variant, the iron of the octants is divided into 4 layers of 23, 23, 23 and

20 cm thickness. A sensitive layer consisting of streamer tubes is placed after each absorber. The endcaps have only the outer sensitive layer.
Streamer tubes are assembled in modules. The total number of modules is 120 in the barrel and 24 in the endcaps. The total number of tubes is 3136 in the barrel and 768 in the endcaps.
The stainless steel tubes of 40 mm diameter with 0.3 mm wall thickness are 4.5 m long in the inner barrel layers and from 3 to 5 m long in the outer barrel and end-caps layers. The anode wire made of gilded Mo is 0.1 mm in diameter. At the ends, such a tube is closed by plastic plugs along the axis of which brass pins are placed to fix the anode wire.
Blowing is performed through special holes in the plugs. The work has been made on a choice of the diameter of the anode wireand the material for the cathode and the gas mixture [1]. Using the gas Ar-CO -n-pentane (2:1:1) under normal pressure, the following characteristics of the streamer signal have been obtained: a rise time about 5 ns, a total width of 80 ns, mean pulse height 1 mA, pulse height spectrum FWHM 80 %.
The spatial resolution in the direction transversal to the tubes is determined by their size and location in the layers and less than 1 cm.
The high signal amplitude in the streamer regime and its small spread make possible to arrange the registration of the longitudinal coordinate by measuring the difference in the time of arrival of the signal at opposite ends of the tube [1,2]. The coordinate is proportional to the measured time difference. The proportionality coefficient is the rate of a pulse propagation through a tube, V, divided by two. In the case of a coaxial wave guide with the gas, this value is practically a half velocity of light in vacuum. Thus, the conversion coefficient "time-coordinate" is 6.7 ps/mm. This method allows a better ultimate resolution to be achieved in comparison with that where longitudinal coordinate is found with charge division technique, one can use only one "analogue-digit" converter for every channel instead of two and anode wire of low resistance, i.e. thick and reliable, thereby ensuring a large plateau of efficiency and simplicity in the design of streamer tubes. The two methods are compared in detail in Refs. [2,3].
One electronics channel can be applied for the definition of the longitudinal coordinate in several tubes connected to a chain. This approach allows one to considerably decrease the number of electronics channels and may be useful applied in the muon identification system where the flux of particles is fairly small.
The electronics channel incorporates two discriminators, a time stretcher and direct counting TDC (Fig. 11.1). A chain of tubes is a line along which the signal propagates. The discriminators are located directly at the ends of a chain and connected to the time stretcher by a twisted pair cable. The time stretcher are also connected to the TDC by twisted pair cable of 20 m long. The calibration signals of a generator may be applied to the ends of the chain and to the places of tube connections. Thus, one can perform a continuous monitoring of the status of electronics.
The duration of the output signals of time stretcher is the time between "START" and "STOP" signals. The coefficient of expansion of a stretcher is determined by the required resolution, the TDC time binning and the dynamic range. Use was made

of a stretcher with an expansion factor 40 since a 12-bit duration measurer with the binning of 2 ns was employed as a TDC. In this case, the bin of the electron track with the stretcher was 50 ps; this corresponds to 7.4 mm along the streamer tube.
The electronics resolution is 18 ps. The delay time of the discriminator depends on the pulse amplitude with the slope of about 6 ps/mV. In the 20^0 -60^0 range, the total temperature drift of the electron track does not exceed 15 ps/ C.
The sensitive layers of the muon system will consist of streamer tubes, connected in chains by four. The total number of electronic channels is 960.
Results of the measurements with 4 m long modules of endcaps are presented below. All measurements were performed for Ar:n-pentane (3:1) gas mixture. Fig. 11.2 shows the dependences upon high voltage (HV) of main characteristics of the streamer tubes modules. The HV operational region is equal to 600 V and is restricted by increasing crosstalk and rates in upper region and by deterioration of resolution in the lower HV region. The efficiency of a module at the plateau is 99.5 %.
The longitudinal coordinate resolution was measured with a set of 6 endcap modules registrating cosmic rays particles. The averaged on all channels resolution was found to be 33 mm. The averaged on all channels resolution for 2 middle tubes of a chain (a chain consists of 4 tubes) was 23 mm (HV 4000 V). The relative resolution taking into account the total length of a chain 16.5 m is equal to 0.2 % and 0.15 % correspondingly.
The long-term operation stability of streamer tubes is being studied. At a radiation damage there appears a rough covering on the surface of the anode wire. In this place in the tube the noise counts increase. The speed of covering formation depends on the anode-wire material and on the initial state of its surface. In the mixture Ar-CO_2-n-pentane (1:2:1) the tubes with gilded Mo wire conserve the service ability after $5 \cdot 10^9$ operations per centimeter of the wire length. This allows to forsee that with the background in the accelerator hall, giving a rate up to 10 Hz/cm , the units of streamer tubes will be serviceable over 10 years. One endcap module being in continuous operation for already two years reveals no changes in characteristics.

References

1. V.M. Aulchenko et al., Preprint INP 85-122, Novosibirsk 1985.
2. S. F. Biagi et al., Delphy internal report 84-9, 1984
3. S. F. Biagi et al., Nucl. Inst. and Meth. A252 (1986) 586
4. V. M. Aulchenko et al., Nucl. Instr. and Meth. A265 (1988) 137

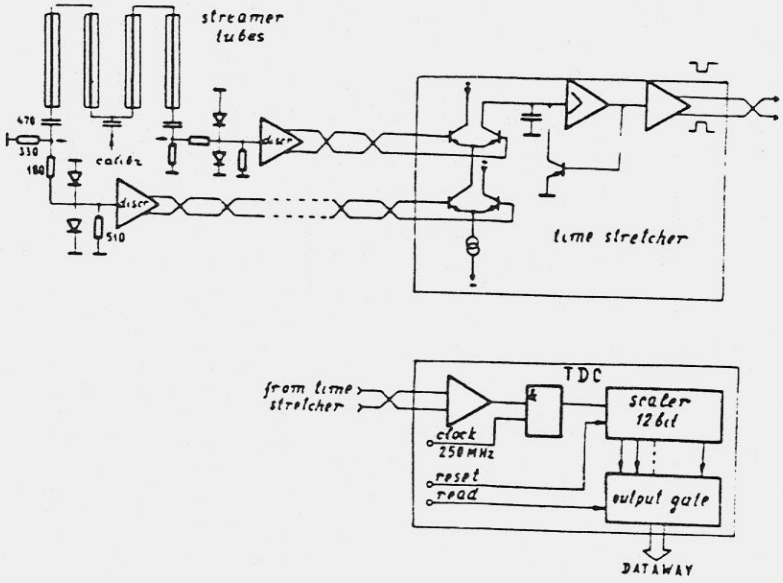
streamer tubes
470
330
180
calibr
510
time stretcher
from time stretcher
TDC
clock 250MHz
reset
read
scaler 12bit
output gate
DATAWAY

Fig. 11.1

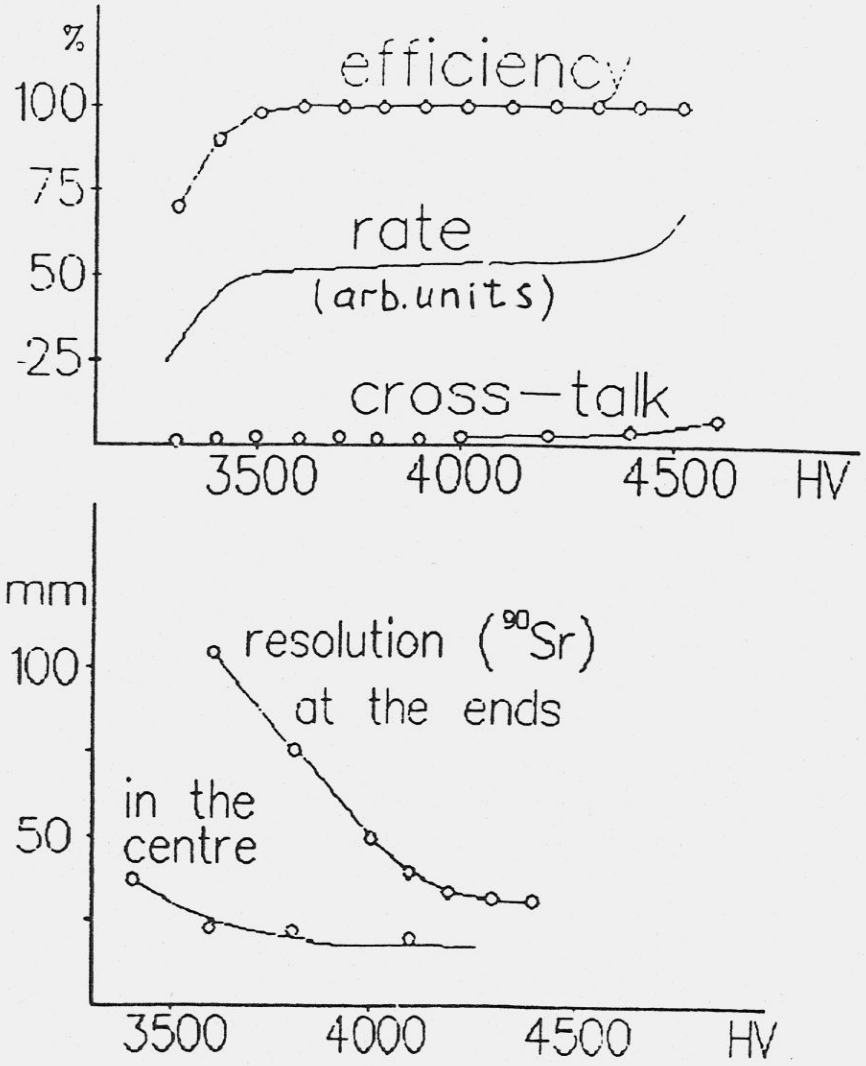

Fig. 11.2 Dependence of efficiency, cross-talk between adjacent channels and resolution on HV value. Gas Ar:n-pentane (3:1)

12. Magnet yoke

The yoke is composed of barrel section of octagonal shape and endcaps. At the same time, it serves as a hadron absorber. The total weight is closed to 800 tons.

The thickness of the endcaps is determined by the flux magnitude , while the thickness of the barrel section is dictated by the requirement of an effective absorption of hadrons.

The barrel section of the yoke is fixed in the collision region of the storage ring VEPP-4M; note that every octant comprises 4 plates (230 + 230 + 230 + 200) mm thick, with spacers located at the corners of the plates. The spacers ensure 100 mm slites between the plates in the octants in which the muon chambers are placed.

The yoke octants are assembled on the mantle rings. In these rings and inner plates of the octants there are adjustable stops to positioning and fixation of the coil.

The endcaps may extend outside, thereby making the inner elements of the detector accessible. In them there are the holes for the light guides of scintillation counters and the slots for cables.

The barrel was produced in 1989-1990. Production of endcaps was delayed and will be completed in 1991.

13. Superconducting solenoid coils

13.1 Main superconducting solenoid coil

The main superconducting (SC) coil is a one-layer solenoid 3268 mm^2 in diameter and 2940 mm long with a 5 mm winding step and a conductor cross-section of 3.8 × 3.5 mm. It is inserted in a cylindrical helium cryostat.

The conductor comprizes two connected strands STP-8-0.85 with dimensions 3.8*1.7 mm^2 made of 8 twisted SC Nb-Ti wires soldered with POS-61. The diameter of the wires is 0.85 mm, the coefficient of filling is equal to 0.4 and the critical current is 500 A (in 5 T field) for each wire.

The SC coil is wound around and welded to the inner surface of a ring helium vessel and is cooled indirectly through a 10 mm stainless steel wall of the vessel. This construction has some advantages :

1 - The ring helium vessel is simultaneously a force bandage for the coil.
2 - High electrical tensions cannot appear, because the coil is shunted with helium vessel walls (resistance of 6 $\mu\Omega$).
3 - Small radiation length of the coil.
4 - The quench of the SC coil to the normal state is not dangerous, since stored magnetic field energy would dissipate uniformly in the coil and in the helium vessel walls, heating them to the temperature not higher then 90 K.

The SC transformer supplies the coil with current of 8 kA, that allows in the stationary regime switch on the coil into the frozen magnetic flux mode. The helium consumption in this mode is approximately 6 l/hour.

The number of turns of the coil is 588, the inductance is equal to 1.2 H. The operational field 2 T is produced with a coil current of 8 kA. That is 50 % of critical current for the used SC. The stored field energy is 42 MJ.

The yoke returns the magnetic flux and provides the required uniformity of the field. The coil must be centred between the yoke poles in order to compensate attraction forces. The coil position can be adjusted from the outside of the cryostat by means of axial arms of supporting system, equiped with strain gauges for force measurements. Since the resistance of helium vessel is only $6 \cdot 10^{-6}$ Ohm for 4.5 K, the time required for current input is equal to 100 hours (helium heat load 200 W). The total helium consumption during the current input period is approximately 16 m^3. While the current is being fed into the coil, a temperature gradient of 0.2 K in the 10 mm wall separating the coil from helium appears. This gradient is tolerable and cannot lead to quench to the normal state.

Simulating experiments were carried out with soldered coils, like the one planned to be used. A coil with the following parameters was wound on a stainless steel frame and tested : 130 mm diameter, 220 mm long with a resistance of 2 $\mu\Omega$, 70 turns of SC wire, inductance $3 \cdot 10^{-4}$ H. No aging processes and degradations were observed during tests when the velocity of current input changes from 10 A/s to 500 A/s.Quench occured for current value of 5.6 kA, although a critical current for this coil was equal to 5.2 kA.

13. Superconducting solenoid coils

13.1 Main superconducting solenoid coil

The main superconducting (SC) coil is a one-layer solenoid 3268 mm^2 in diameter and 2940 mm long with a 5 mm winding step and a conductor cross-section of 3.8 × 3.5 mm. It is inserted in a cylindrical helium cryostat.

The conductor comprizes two connected strands STP-8-0.85 with dimensions 3.8*1.7 mm^2 made of 8 twisted SC Nb-Ti wires soldered with POS-61. The diameter of the wires is 0.85 mm, the coefficient of filling is equal to 0.4 and the critical current is 500 A (in 5 T field) for each wire.

The SC coil is wound around and welded to the inner surface of a ring helium vessel and is cooled indirectly through a 10 mm stainless steel wall of the vessel. This construction has some advantages :

1 - The ring helium vessel is simultaneously a force bandage for the coil.
2 - High electrical tensions cannot appear, because the coil is shunted with helium vessel walls (resistance of 6 $\mu\Omega$).
3 - Small radiation length of the coil.
4 - The quench of the SC coil to the normal state is not dangerous, since stored magnetic field energy would dissipate uniformly in the coil and in the helium vessel walls, heating them to the temperature not higher then 90 K.

The SC transformer supplies the coil with current of 8 kA, that allows in the stationary regime switch on the coil into the frozen magnetic flux mode. The helium consumption in this mode is approximately 6 l/hour.

The number of turns of the coil is 588, the inductance is equal to 1.2 H. The operational field 2 T is produced with a coil current of 8 kA. That is 50 % of critical current for the used SC. The stored field energy is 42 MJ.

The yoke returns the magnetic flux and provides the required uniformity of the field. The coil must be centred between the yoke poles in order to compensate attraction forces. The coil position can be adjusted from the outside of the cryostat by means of axial arms of supporting system, equiped with strain gauges for force measurements. Since the resistance of helium vessel is only $6 \cdot 10^{-6}$ Ohm for 4.5 K, the time required for current input is equal to 100 hours (helium heat load 200 W). The total helium consumption during the current input period is approximately 16 m^3. While the current is being fed into the coil, a temperature gradient of 0.2 K in the 10 mm wall separating the coil from helium appears. This gradient is tolerable and cannot lead to quench to the normal state.

Simulating experiments were carried out with soldered coils, like the one planned to be used. A coil with the following parameters was wound on a stainless steel frame and tested : 130 mm diameter, 220 mm long with a resistance of 2 $\mu\Omega$, 70 turns of SC wire, inductance $3 \cdot 10^{-4}$ H. No aging processes and degradations were observed during tests when the velocity of current input changes from 10 A/s to 500 A/s.Quench occured for current value of 5.6 kA, although a critical current for this coil was equal to 5.2 kA.

13.2 Compensating superconducting solenoid coils

Two compensating coils are situated at the end-caps of the main coil and serve for the compensation to zero of the magnetic field integral on the beam trajectory. The coils 450 mm long are made of SC conductors with diameters of 1.2 and 0.85 mm. The operational field is equal to 6.5 T, the current is 385 A and the stored energy is 140 kJ. Current is supplied through special inlets. The inner helium surface of the cryostats of the compensating coils is connected with storage ring vacuum volume and serves simultaneously as a cryogenic pump.

The cryogenic maintenance system allows :

1. Refrigeration from normal temperature to 80 K with liquid nitrogen.
2. Refrigiration from 80 K to 4.5 K with liquid helium.
3. Cryostating at the level of 4.5 K.

Time schedule

1990 - manufacturing of the main coil with cryostat ;
manufacturing of the compensating coils with cryostats
1991 - tests of cryostats and coils
1992 - getting into the stationary operation of the magnetic system

14. Electronics

A data acquisition system (DAS) for the detector KEDR, referred to as "KLYUKVA"[1], was designed to meet the requirements for detectors used in colliding beams experiments . Its main features are :

- the large number of precise measuring channels;
- capability of designing an efficient multy-level trigger;
- short deadtimes of A/D conversion and data recording;
- parallel precomputer processing;
- derandomizing and compressing of the data before recording;
- convenient in use; low cost and possibility of production in our experimental workshop.

The main organization principles of DAS "KLYUKVA" are :

- measurement of time intervals with a 2 ns step by direct counting. Transmitting a clock frequency from one center to every digitizing channel. Digitizing of analog information mostly by converting to time intervals.
- almost all registrating electronics is placed in special crates with fast dataway, including trigger communications and clock frequency distribution. Standard crates (CAMAC, in future VME) are used for communication with computer. They contain central parts of the main DAS devices - triggers, readout, synchronising.
- fast special processors with built-in processing algorythms are used as the controllers for the special crates.

Measuring channels consist of front-end electronics (preamplifiers, discriminators, expanders, ets.) which is placed near the detector, communication lines and ADC devices. These devices as well as the modules for digital processing, for selecting and recording "good" events, power supplies, testing systems ets. are installed in the control room.

Registrating electronics is placed in the special crates. Each special crate contains 20 units - 16 data modules (DM) and 4 service modules (Fig. 14.1). Service modules have fixed positions, determined by the dataway. The DM positions are the same for all types of units. Service modules are - readout processor (RP), transmitter of service signals (TTS), interfaces of primary and secondary triggers (IPT, IST) [2]. DMs accept and digitize analog information, prepare and transfere data to IPT and IST for trigger decision [3,4,5]. The upper limit for digitizing is 80 μs, after this time RP takes data from DM via the 100 ns dataway.

RP reads, processes and selects data from DMs of his crate and prepares information to the computer. The RP operating program is stored in his command RAM. The command RAM also stores pedestals of the channels placed in that crate.

RP can :

- receive data from DM in arbitrary sequence;
- record data having a special mark;
- compare with pedestals and buffer according to the result of the comparison;
- substract pedestals and buffer only positive difference;

- zero suppression and so on.

For storing the processed data, RP has 2 data RAMs, which with DM registers provide 3-step derandomizing.

The architecture of DAS is shown in Fig. 14.2. Besides readout electronics, CAMAC crates contain the central parts of primary (PT) and secondary (ST) triggers , triggers of higher levels and central control device (CD). CD synchronizes all special crates and transmits clock frequency for time measurements (250 MHz with detecting a half period). The clock frequency is phased by PT strobe (Fig. 14.3). It is convenient if one wants some channels to work in a "common start" mode. With high luminosity in high rate environment this mode can reduce losses. Of course, in this case one must use a delay line without deadtime (cable).

Time digitizing channels are working in selfstarting mode (common stop). AD channels are controlled by coupled time channels (for example, measuring time and dE/dx in drift chamber channel). If there's no coupled time channel, ADC is working in a "common start" mode.

The operation begins with a PT strobe, which is generated from data received from DM, scintillators and other devices (Fig. 14.4). Then the PT system is closed and all DMs start digitization of data. After the PT strobe the information needed for ST decision is transfered from DM to IST. The ST deadtime is about 10 μs. If the ST decision is negative, the DMs are cleared and PT is opened. Upon a positive solution digitizing continues. When the time for AD convertion is finished (80 μs), information transferes from DMs to the empty data RAM of RP (100 μs). Then DMs are cleared and PT is opened. All this time CD is trying to record data from filled data RAMs into the computer. So the deadtime of the system is about 200 μs.

Some words about events selection. The strategy of the trigger designing is to keep the same amount of loss - 10 %, while making selection conditions more hard from step to step. The selection capability of each following step is higher than at a previous one, because it receives more detailed information and has more time for making decision. The high limits for intensity of PT strobes (10.000 ev/s) and positive solutions of ST (500 ev/s) are shown in the picture and are determined by two times: deadtime of ST (10 μs) and deadtime of the whole system (200 μs).

Architecture of the PT is traditional - mostly coincidence devices. The main requirement is high efficiency for "good" events. One DM can give up to 4 bits of "PT" data. The aim of the ST is a further reduction of background by operating with more hard selection conditions. The amount of information from one DM to IST is up to 64 bits. This provides good opportunities for fast making of the detailed event image.

Each level of trigger system consists of a central part in CAMAC crate and its interfaces in special crates. Interfaces are hardwired devices. They are forming the part of the decision. Central parts of the PT and ST are controlled and retuned from the dataway. They form the event image and compare it with masks stored in memory.

Fig. 14.5 shows the rates and losses of the system. Here another level of precomputer selection is shown - a special processor (SP). SP receives data from the chosen ROP via their front panel connectors, while the data RAM is filling. SP data are followed with command codes. SP operates only with specially marked commands from command

RAM. While SP is operating, the computer waits. Upon a negative solution the conformable data RAMs are cleared. If the response time of SP is shorter then 80 μs (AD conversion of the next event), there's no additional loss. Using of SP can be very efficient. SP receives maximally detailed, selected and processed information. Every part of the event has its own fixed place in SP memory. SP can analyse only a part of the event. Hence SP is the on-line processor, one needs not to write all information about the event in its memory. So the memory needs not to be deep, but very fast. For example, SP can be used as a total energy trigger.

Even without SP DAS provides precomputer handling rate up to 500 ev/s with 10 - 15 % loss. If we use CAMAC controllers with DMA and the speed of 2 μs/word, with the everage event length 1000 words, the computer can only serve as a dispatcher for other computers. With the help of SP the event rate is reduced and we can increase the event length and the time for computer processing.

In Fig. 14.5 the limits for rate capability of DAS are shown. The parameters of DAS provide an opportunity for an efficient use of high level trigger (company of computers). We still don't make a final choice for on-line processing.

The main factors that provide reliability of electronics and convenience in use are :

- digitizing of information and preparing data for PT and ST is made in one unit - DM;
- data for PT and ST are transmitted from DM via dataway;
- input cables connectors are the part of dataway and are immobile while replacing the DM (Fig. 14.6);
- power supply and ventilation are from one center.

Digital part of electronics is made on 500 series (ICL) integral circuits. Power dissipation in one crate can reach 1.2 KW. The racks for special crates are used as airtubes and contain 6 crates (Fig. 14.7).

The necessary amount of the described electronics is now under production. At the same time electronics is handled by physicists, who used it during the constructing and testing the components of the detector. For these purposes we installed several DASs. Each of them consists of one or two special crates and the total number of service units. Four types of DMs (T,T2A,TAM, A32) are designed and manufactured now in the needed amount.

The amount of electronics for the main registrating systems of the detector existing so far and our future plans are shown in Table 14.1.

One can see that DAS like "KLYUKVA" can be built with the help of FUSTBAS standard, which has comparable characteristics of dataway, areas of PC boards and power dissipation. But now and in close future it is very hard for us to get enough FUSTBUS crates, besides they are very expensive.

On the contrary "KLYUKVA" can be produced in our experimental workshop, it is easy in technology and has no redundant accessories, typical to any standard. We also add some opportunities that made DAS more suitable for our experiments with colliding beams.

World practice shows that such a way of constructing DAS is becoming usual.

References

1. V. M. Aulchenko, S. E. Baru and G. A. Savinov, " Electronics of new detectors of INP for colliding beam experiments ", Proc. of the Inter. Symp. on coordinate detectors for High Energy Physics. Dubna, 1988, pag. 371
2. S. E. Baru et al.,The service modules of DAS " KLYUKVA ". Preprint INP 88 - 26 Novosibirsk, 1988
3. V. M. Aulchenko et al., The data modules deltaT, TP, T2A of DAS " KLYUKVA ". Preprint INP 88 - 22 Novosibirsk,1988
4. V. M. Aulchenko et al., The data module TAM of DAS " KLYUKVA ". Preprint INP 88 - 30 Novosibirsk, 1989
5. S. E. Baru and G. A. Savinov, The data module TAM of DAS " KLYUKVA ". Preprint INP 89 - 122 Novosibirsk,1989

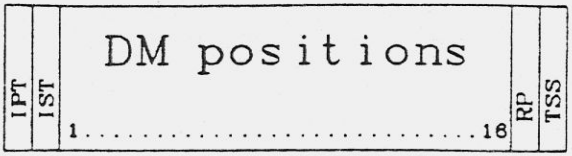

Fig. 14.1 The special crate.

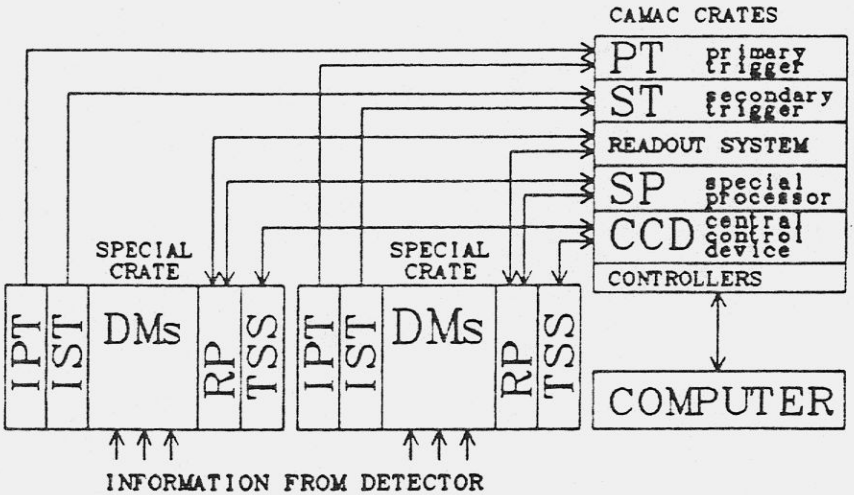

Fig.14.2 Architecture of DAS.

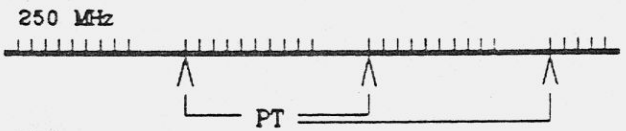

Fig.14.3 The clock frequency.

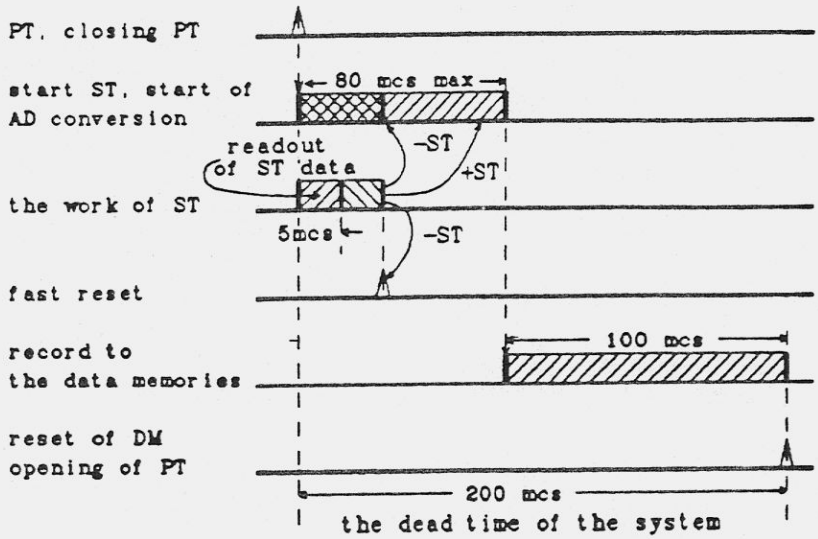

Fig.14.4 Time diagram of event processing.

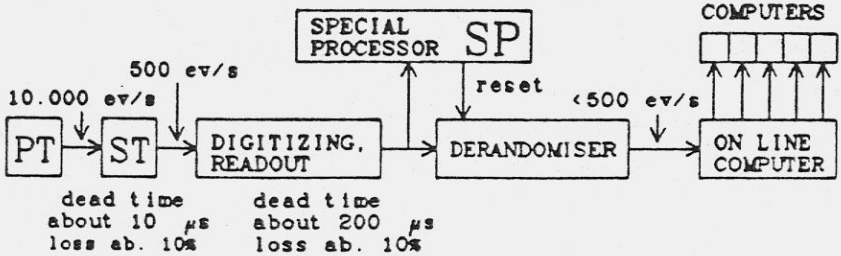

Fig.14.5 The trigger system. Rate capability and losses.

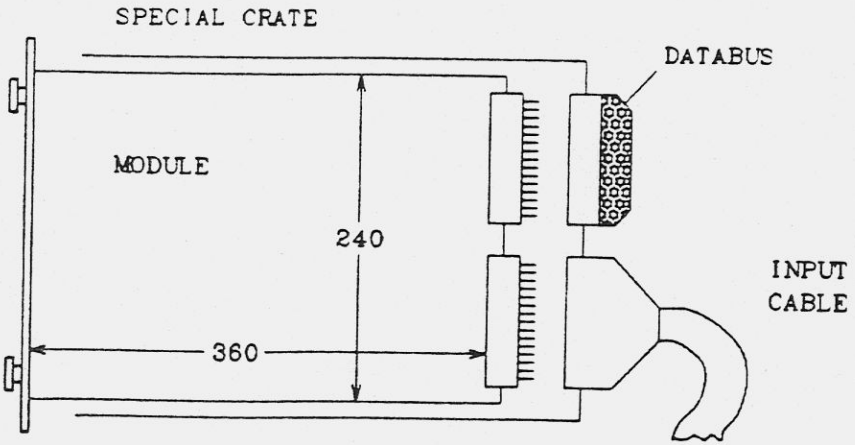

Fig.14.6 Construction of a special crate.

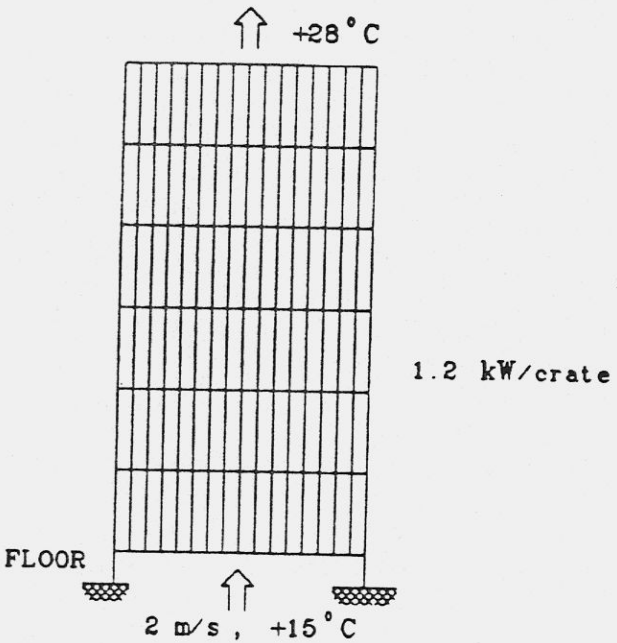

Fig.14.7 The cooling of rack.

Table 14.1

System	Total amount	May '90 Designed	May '90 Developed	Final date
Microvertex Detector	2048 Channels	10%		
Vertex Detector	320 Channels: Preampl. - 40 units Discr. - 20 units DM(T) - 20	100%	10%	1991 2^{o} quarter
Drift Chamber	1500 Channels: Preampl. - 250 units DM(TAM) - 435	100%	30%	1991 2^{o} quarter
Scintillators	128 Channels: Discr. - 32 units Q/T - 16 units T/A/D - 16 units DM(T) - 16	100%	30%	1991 4^{o} quarter
Calorimeter (LKr)	10000 Channels: Preampl. and Discr. - 10000 DM(A32) - 312	100%	5%	1992 1^{o} quarter
Calorimeter (CsI)	1200 Channels: Preampl. - 1200 Shapers - 80 units DM(A32) - 40	close to the end	10%	1991 1^{o} quarter
Muon system	1000 Channels: Discr. and Expander - 1000 DM(T) - 60	100%	80%	3 Lays 4^{o} quarter '90 4^{o} lay and edge 4^{o} quarter '91
Electron Tagging System	1440 Channels: Preampl. and Discr. -120 units Shapers - 30 units DM(T) - 90	100%	30%	1991 1^{o} quarter
Special Crates and Racks	80 Special Crates 13 Racks	100%	10%	1990 4^{o} quarter
Service Modules	80 ROP 80 CCD etc.	100%	90%	1990 3^{o} quarter
Trigger System	3 CAMAC Crates	Architecture and opportunities		
Power Supply	-5V,-2V 14 Racks	100%		1991 1^{o} quarter
H.V. Power Supply		80%		1992 1^{o} quarter

15. Schedule

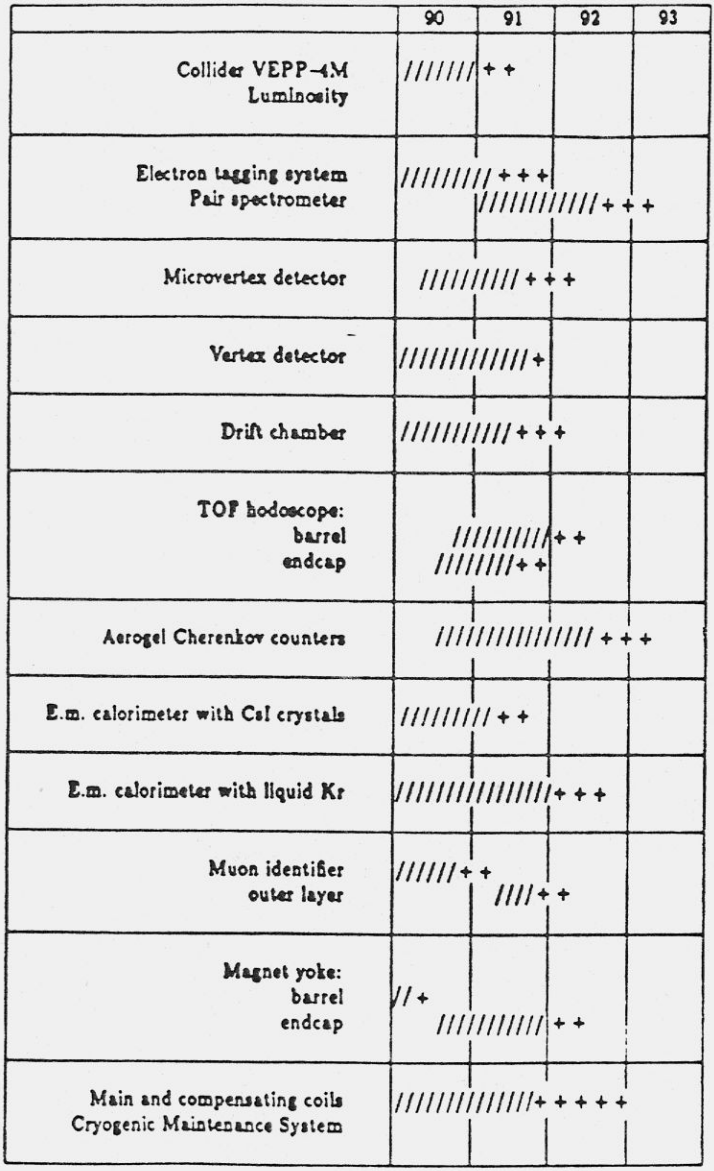
90
91
92
93
Collider VEPP-4M
Luminosity
Electron tagging system
Pair spectrometer
Microvertex detector
Vertex detector
Drift chamber
TOF hodoscope:
barrel
endcap
Aerogel Cherenkov counters
E.m. calorimeter with CsI crystals
E.m. calorimeter with liquid Kr
Muon identifier
outer layer
Magnet yoke:
barrel
endcap
Main and compensating coils
Cryogenic Maintenance System
Legend:
- construction
- assembling in the detector